POLITECNICO
MILANO 1863

SCUOLA DI INGEGNERIA INDUSTRIALE
E DELL'INFORMAZIONE

State of the art and analysis of open-end winding motor drives

Tesi di Laurea Magistrale in
Electrical Engineering - Ingegneria Elettrica

Author: **Michele Falsiroli**

Student ID: 977226
Advisor: Prof. Maria Stefania Carmeli
Academic Year: 2022-23

Abstract

In this research, the operation of open-end winding motors is analysed, with a focus on synchronous permanent magnet motors (OW-PMSM).
This type of motor, which differs from conventional ones due to the absence of the star-delta connection in the stator winding terminals, enables two independent VSI inverters to be connected to its ends, which is known as dual-inverter configuration.
It will be analysed the different possible configurations that can be implemented mainly in traction applications, such as in trains or electric vehicles, with their benefits and drawbacks, before moving on to the modelling of the motor and control system adopted.
The latter considers the use of two separate voltage sources, connected to the DC-link of the two VSIs. A hybrid modulation, combining a six-step and a PWM, will be implemented by means of a lookup table to control the two inverters, with the aim of minimising switching losses in the system. It will also be compared with a more conventional modulation strategy called 180° decoupled SVPWM.
In order to verify the effectiveness of the analysed solutions for OW motor control, some simulations were carried out by implementing the entire system on MatLab and Simulink, and using telemetry data recorded during the use of an electric vehicle during a lap on the Varano circuit.
In the end, the open-end winding motor, driven by the lookup table-based modulation, was compared with a conventional permanent-magnet synchronous machine, to analyse the benefits obtained from the dual-inverter configuration.

Keywords: OW-PMSM, dual-inverter, electric vehicles.

Abstract in lingua italiana

In questo studio viene analizzato il funzionamento dei motori ad avvolgimento statorico aperto (open-end winding), concentrandosi soprattutto su quelli sincroni a magneti permanenti (OW-PMSM).
Questa tipologia di motori, che si differenzia da quelle convenzionali per l'assenza della connessione a stella-triangolo nei terminali dell'avvolgimento statorico, permette di connettere ai suoi capi due inverter VSI indipendenti, che prende il nome di dual-inverter.
Verranno analizzate le varie configurazioni, per questa tipologia di motori, che possono essere implementate principalmente nell'applicazioni di trazione, come in treni o veicoli elettrici, con i relativi benefici e punti deboli, per poi passare alla modellizzazione del motore e del sistema di controllo adottato.
Quest'ultimo prende in considerazione l'utilizzo di due sorgenti di tensione separate, connesse al DC-link dei due VSI. Una modulazione ibrida, che combina un six-step a un PWM, verrà implementata tramite una lookup table per il controllo dei due inverter, con l'obbiettivo di andare a minimizzare le perdite di commutazione nel sistema. Essa verrà messa a confronto anche con una strategia di modulazione più convenzionale denominata 180° decoupled SVPWM.
Per verificare la validità delle soluzioni analizzate per il controllo del motore OW, sono state svolte alcune simulazioni tramite l'implementazione dell'intero sistema su MatLab e Simulink, andando ad utilizzare dei dati di telemetria registarti nell'uso di un veicolo elettrico durante un giro eseguito sul circuito di Varano.
Infine, è stato messo a confronto il motore open-end winding, gestito dalla modulazione basata sulla lookup table, con una convenzionale macchina sincrona a magneti permanenti, per analizzare i benefici ottenuti dalla configurazione dual-inverter.

Parole chiave: OW-PMSM, dual-inverter, veicoli elettrici.

Contents

1 Introduction

Over the years, electric motors have been increasingly integrated into every area of industry, seeing their use increase, especially nowadays, in the automotive sector as well. Indeed, with the ecological transition that has been taking place in recent years, the transition from internal combustion engines (ICE) to the more modern electric motors is becoming increasingly evident, the latter being subject to continuous technological research to improve their performance and efficiency, while also trying to reduce implementation costs.

Electric motors are seen as the main solution to replace internal combustion engines in the automotive sector, as they have a much higher efficiency (even above 90%) than thermal engines, which is around 20 to 30%. This factor makes modern electric motors more efficient, as they are also subject to far fewer combustion and mechanical losses.
The biggest difference between the two types of motors, however, concerns their mechanical characteristics. In fact, electric motors are able to provide torque even at zero rpm, which can correspond to the maximum value, whereas ICEs require a minimum operating speed, i.e. a minimum speed at which it is able to overcome friction and losses, thus entering into operation. The electric motor is also able to reach a higher speed, i.e. higher rpm values, and it does not need a gearbox. However, this results in a generally lower top speed than thermal engines. The most significant advantages of electric motors remain the absence of noise, vibration and pollution, the need for less maintenance, and a longer service life as component wear is low. On the other hand, however, internal combustion engines allow a longer vehicle range and have a lower overall cost.

The most commonly used electric motors in this sector are those powered by alternating current, which are divided into two main classes: synchronous and asynchronous, the latter are commonly referred to as induction motors.

Over the years, with an increasing development of new technologies and the improvement of existing ones, Synchronous motors have seen an increasing application in various sectors, especially those with permanent magnets. The main difference between the two macrotypes of AC-powered motors is that induction motors are less complex than synchronous

one, even in terms of construction, and less expensive. This is because permanent magnet motors are also much more expensive due to the rarity and price of the materials from which they are made. Asynchronous motors are also easier to implement and repair, however, synchronous motors have a higher power density for the same size, being able to deliver more power and achieve higher efficiency and precision values. Furthermore, synchronous motors are able to work with both lagging and leading power factors, while induction motors only work with lagging PF values. This is why synchronous motors are also used in power stations because they are able to improve the power factor or used as voltage regulators in transmission lines. This type of motor maintains a constant speed even when the load varies, unlike asynchronous motors, there is no slip and the velocity depends on the mains frequency and the number of pole pairs, always reaching synchronous speed. Indeed, this type of motor is used in applications that require a very precise and constant speed.

On the other hand, induction motors, represented in the Figure 1.1, are widespread in many industrial and domestic fields because, as mentioned above, they are low in cost and, unlike all other electrical machines, they have no permanent magnets, no brushes, no commutation rings and no position sensors, so they are much simpler to make and less bulky. They are used in various industrial sectors such as food, chemicals, metallurgy, in mining-type plants, in lifting equipment (such as lifts, hoists), in conveyor belts, and of course have also found many uses in electrical vehicles [1].

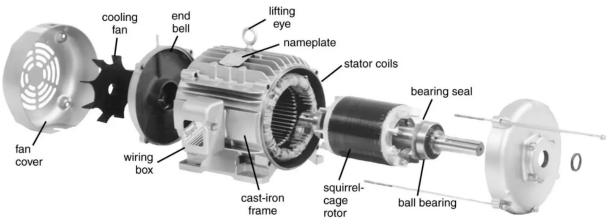

Figure 1.1: Induction motor components.

The synchronous motors mainly used are those with permanent magnets that can be glued to the outer surface of the rotor (SMPM - surface mounted permanent magnet) or inserted inside the rotor (IPM - internal permanent magnet), as shown in Figure 1.2. The first topology can be considered as an isotropic machine, as the d-axis inductance can be considered equal to the q-axis one (Ld $\approx$ Lq), as the inductance values can be considered independent of the rotor position. In addition, SMPM motors are easier to realise and a slightly smaller axial length, but the IPM motors have a higher overload capacity and have the ability to generate more torque, making them more cost-effective, especially in cases where there is a high rotor anisotropy [2].

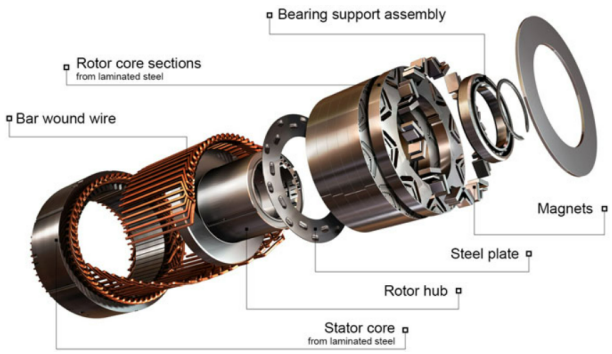

Figure 1.2: Internal PM synchronous motor components.

Going into the details of the application of these two types of motors in electric vehicles, to increase the operating range and autonomy of modern electric cars, it was decided to use two different DC power sources, the so-called range extending electric vehicles (REEVs). In this new type of car, there is the presence of the DC/DC converter which is essential to maintain a constant voltage across the DC bus and to manage the power flow.. This converter, however, greatly increases the complexity of the system and also the cost, with higher power consumption. To overcome this problem, one possible solution would be the introduction of Open-end Winding (OW) motors[3]. This particular type of motor is obtained by simply opening the neutral point of a conventional three-phase y-connected motor, thus obtaining two independent three-phase inputs in which each end of the stator winding can be fed by an independent inverter leg.

The main part of this study, set out in the following chapters, will be the development of a control to exploit the strengths of open-winding motors, while at the same time reducing the disadvantages of the configuration under investigation as much as possible. For this purpose, several papers have been analysed which propose various control methods for OW motors, according to the application in which they will be used. [4-7] deal with control techniques for open-winding induction motors, while [8-21] focus on those using permanent magnets, which is the type on which the current study will concentrate most.

2 | State of the art

As mentioned above, different scientific articles are analysed in which the use of open-end winding motors is implemented in various applications, and compared with conventional systems. These papers were investigated to find the best solutions, in terms of control efficiency and optimisation, for the two main types of motors, induction motors and permanent magnet ones. In addition, the various configurations of the DC-link on the system and the different applications in which open-end winding motors can be implemented were analysed.

2.1. Open-end winding induction motor

Such as, in [4] the control system of an open-winding induction motor fed by a dual-inverter connected to two isolated DC sources is presented. Two capacitors are also implemented on the dc-link to filter out voltage fluctuations and to provide the required reactive power. In this paper, the operating principle of voltage vector distribution is analysed. This technique assumes the definition of the stator voltage vector $\bar{u}_s$ as the difference between the output voltage vectors of the two inverters ($\bar{u}_s = \bar{u}_{s1} - \bar{u}_{s2}$). The admissible region of the voltage vector distribution, in which the common end of the vectors $\bar{u}_{s1}$ and $\bar{u}_{s2}$ must lie (denoted with point J), is given by the superposition of the two hexagons, whose centres are the starting point of the voltage vectors of the inverters (O1 and O2), and radius defined by the SVPWM modulation, equal to $\sqrt{\frac{2}{3}} * V_dc$. The stator current, on the other hand, is obtained by measuring the stator phase currents using current sensors. The system under consideration is represented by the Figure 2.1.

Two algorithms for calculating the rotor flux ψ_r, motor loss minimisation (MLM) and maximum power sharing capability (MPSC), are proposed to maximise system efficiency and power sharing capability. Moreover, a selection strategy based on the operating conditions is defined.
As the name suggests, the MLM aims to minimise the total electrical losses of the machine at each permissible operating point in steady state condition. These losses are obtained from the sum of the losses in the iron and in the copper. To find the minimum points of

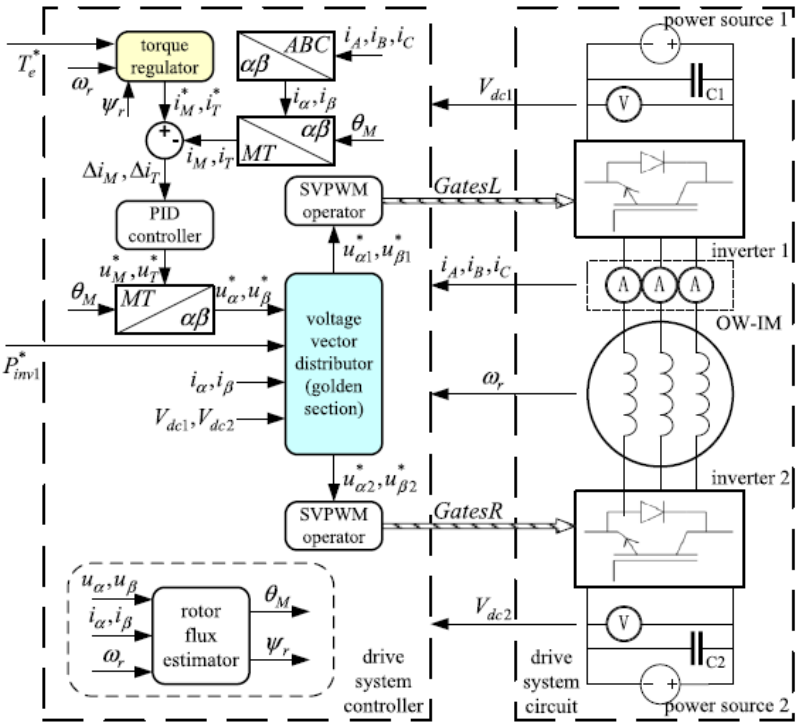

Figure 2.1: Overall system configuration with open-winding induction motor [4].

interest, the partial derivative of the total loss to the flux must be set equal to zero. In this way, the ψ_r values that minimise the losses at each admissible operating point can be obtained and entered into a lookup table.

The MPSC algorithm, on the other hand, has the task of finding the minimum value of the vector amplitude $\bar{u}_s$ to maximise the power sharing capability. To do this, the partial derivative by the square of the $\bar{u}_s$ magnitude, over the rotor flux must be calculated and set equal to zero. The solutions of this equation are called minimum voltage vector amplitude (MVVA). Nevertheless, the found values of the stator voltage and current vector must comply with the limits of the dc source voltage and current capacity of the inverters. If the minimum voltage value exceeds the constraints, the operating point cannot be reached and therefore the MVVA method cannot be used. In this case, the solution with the minimum value of $\bar{u}_s$ which solves the maximum current vector amplitude (MCVA) equation, and the respective value ofψ_r, will be sought.

A strategy for the selection of the method to be adopted is also presented, according to the operating conditions. In order to optimally select the method to be used, it must first be examined which one guarantees the desired dynamic performance and, if an efficiency capable of realising the required power exchange is achieved.

Tests show that the MLM can achieve higher values of flux amplitude, and therefore output torque, at the same operating point. All three proposed methods reach a high efficiency in the heavy-load high-speed zone. However, the MLM algorithm has a much higher efficiency than the MPSC in the low-speed light-load zone. Instead, with the use of MVVA and MCVA, it is possible to have a high-power sharing capability and keep it constant over a larger operating area. For these reasons, and according to the selection principles listed above, the MLM will be selected if it is suitable for the current operating point and if it will be able to meet the required power sharing. Otherwise, the MPSC algorithm will be selected, and more precisely, if the actual point is within the operating range, the MVVA will be selected, otherwise the MCVA will be implemented.
Once the reference value of the rotor flux has been derived using the proposed algorithms, the stator current can be calculated and, using a PI controller, the desired voltage $\bar{u}_s^*$ will be obtained. It will be divided between the two inverters to meet the power sharing through the voltage vector distribution strategy.

The one proposed in the paper optimises the two inverter voltage vectors in the feasible zone, so that the generated power of inverter one matches the desired value as closely as possible. The golden section search method is used because it has a stable computational burden and a number of iterations that can be flexibly modified. This strategy synthesises $\bar{u}_{s1}$ and $\bar{u}_{s2}$ by the desired power sharing value and the motor power. If both vectors fall within the permissible range, they will be used as the solution of the linear voltage vector distribution. In other cases, the GS method will be applied, and an appropriate probe angle will be sought, i.e. a spatial angle of the two parallel lines passing through the centre of the two hexagons, which define the orientations of the two voltage vectors. From the intersection of these two lines with the edges of the voltage modulation ranges four different points can be found. The one with the smallest deviation from the desired power sharing will represent the solution of the current probe angle. The number of iterations is set in the simulations.
The control of the system is completed by the implementation of a speed controller to derive the torque value of the reference motor, which together with the desired output power for the inverter1, represent the system inputs. Furthermore, from the torque, the stator current is calculated and through another PI, $\bar{u}_s^*$ is obtained. It is then divided into the two inverter voltage vectors by the voltage vector distribution, which will be the inputs to the space vector PWM that give the switching signals.

To verify the effectiveness of the presented solution, tests were carried out. It can be seen that the ripple in the phase voltages is almost zero as there are sinusoidal behaviour. Both the output power of the inverter1 and the motor speed effectively follow their respective

references. Furthermore, the losses obtained with the proposed strategy are lower than those obtained with a conventional flux inverse control. The main problem highlighted by the simulations is that, when the flux calculation algorithm is switched, there are large variations in the rotor flux that cause a deterioration in system performance and a possible loss of control accuracy.

Paper [5] presents a new and simple scalar control strategy for an open-end winding induction motor, capable of extending the speed range. This motor is powered by a dual-inverter configuration connected on one side to a DC source, and on the other side to a capacitor. The first inverter will work at unity power factor supplying only active power, while the second inverter will have the task of generating the reactive power required by the system and keeping the voltage on the capacitor ends constant. For these reasons, the voltage vector of inverter1 will have to be in phase with the motor current, while the voltage of inverter2 will be in quadrature.

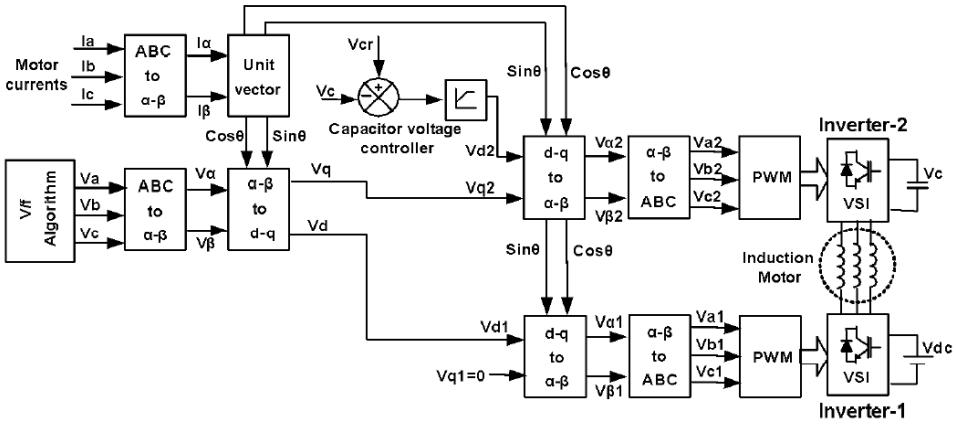

Figure 2.2: Proposed control scheme for the open-winding induction motor [5].

The proposed control scheme aims to increase the voltage on the motor and to counteract high back-emf values above base speed, to keep the voltage on the capacitor constant and to allow independent control of the two inverters. An open-loop V/Hz control is implemented in the system, operating in a dq synchronous reference system, in which the d-axis is aligned with the stator current vector. The V/Hz allows the calculation of phase reference voltages corresponding to a specific desired speed. They are converted into the $\alpha\beta$ components, and then into the dq components, using the Park's transform, which represent the active and reactive components of the motor voltage respectively. The components of the reference $\alpha\beta$ currents are used to obtain the unit vectors that are designed to ensure alignment between the d-axis and the motor current phasor. $V_d = V_{d1}$ is used to obtain the three-phase reference voltage for inverter1 in which V_{q1} is set equal to zero, since this inverter has the task of generating only active power. Instead, to keep the

voltage across the capacitor constant, another controller is implemented which computes the difference between the reference value and the current voltage value. Based on this error, the controller generates the inverter's d-axis voltage reference2. V_{q2} will instead coincide with the value of the reference voltage V_q. These voltages are transformed into the three-phase components and sent to the sinusoidal PWM to generate the inverter2 gate signals, exactly as for inverter1.

From the simulations performed, it can be verified that the two inverters actually operate under the conditions listed above, and that the voltage on the capacitor is maintained at a constant value. Furthermore, as the speed increases, an increase in the modulation index is observed, which corresponds to an increased voltage delivered to the motor by the inverter2. Thanks to this method, it is possible to extend the motor's speed range even without the use of field weakening, thus avoiding a decrease in torque and efficiency.

The article [6] proposes a high-efficiency control method for an open-end winding motor fed by a dual-inverter configuration, connect to two different dc sources. The proposed control operates in the low-speed zone and aims to improve the output voltage waveform. A bi-directional chopper, in addition to improving the efficiency of the motor, is used on the second side to regulate the V_{dc2} voltage together with the inverter, as can be seen in the Figure 2.3:

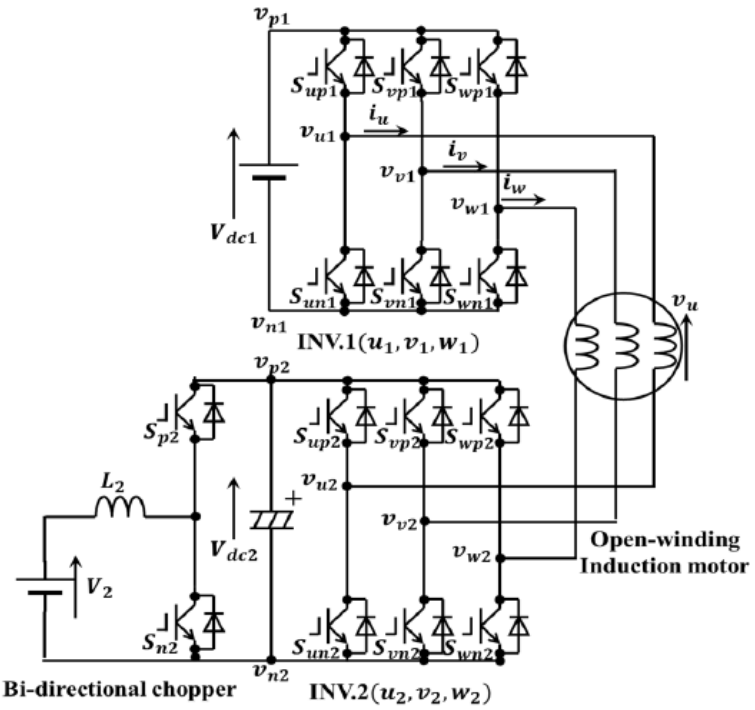

Figure 2.3: Configuration of the open-end winding induction motor drive with dual-inverter and bi-directional chopper [6].

To realise the control method, SVPWM modulation was applied to both inverters. The PWM waveform generated by the dual inverter has a reduced peak value ($V_{dc1} - V_{dc2}$) than conventional methods, decreasing losses at low speeds and improving voltage distortion. Pulse peak value of the winding voltages is reduced by outputting synchronised pulses in the two inverters. Only the switching states obtained by selecting the same vectors for both inverters (00',11',22',33',44',55',66' and 77') are used to realise this strategy. Therefore, the combination of the space vectors of the two inverters results in the feasible region, represented in Figure 2.4.

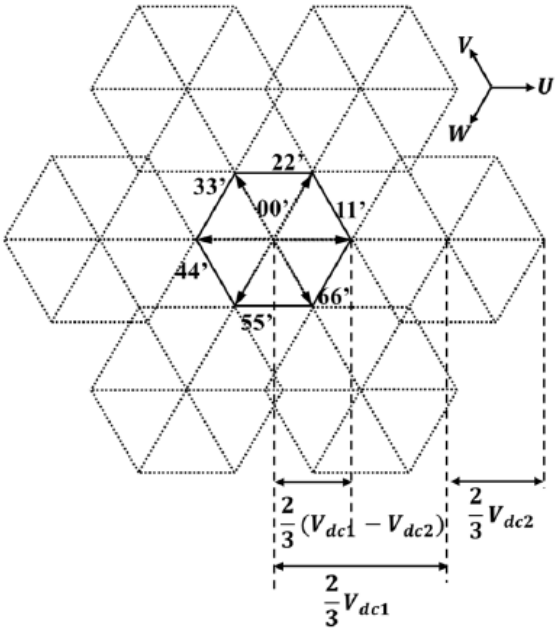

Figure 2.4: Voltage output vector for the analysed method [6].

A commutation pattern is also proposed in the paper to avoid the dead-time problem due to switching in the two inverters. It detects the direction of the phase currents and is divided into 3 steps, from which the switching table for the dual-inverter is derived. From the simulations carried out, the effectiveness of the proposed solution is verified. It can be seen from the graphs that the peak voltage is greatly reduced from 240V to 40V. The harmonic component of the output voltage is decreased from 1.03 to 0.74 and the THD of the phase voltage goes from 320% to 140%. Finally, there is also a reduction in motor losses compared to conventional control methods.

In [7], a model predictive flux control (MPC) for a dual-inverter drive an open-end winding induction motor powered by a single DC source is presented. This type of control is based on the use of torque and stator flux as cost function control variables. The proposed MPC aims to both eliminate the disadvantages of weighting factors and minimise torque ripple. In the control algorithm, Forward Euler's method is used, where T_S is the sampling period and k is the sampling state. Once the model has been discretized, the stator flux can be estimated and through this both the stator current and the electromagnetic torque can be predicted, after also measuring the machine voltage and current.
The cost function g (2.1), on the other hand, is divided into two parts, which are used to estimate the torque and flux errors respectively, and the voltage vector with the lowest cost function will correspond to the switching state.

$$g = [T_e^{ref} - T_e(k+1)] + \lambda[\psi_s^{ref} - \psi_s(k+1)]. \tag{2.1}$$

As mentioned earlier, the main problem is the regulation of the weighting factor λ as it could lead to anomalies in the motor's main variables, which greatly reduce performance. For this reason, the proposed MPC aims to eliminate the need of the weighting factor. For this purpose, the reference torque is defined as the product of the rotor flux and the reference stator flux. Besides, the amplitude of the rotor flux is set to a desired value in the Equation (2.2)

$$|\psi_s^{ref}| = \psi^*. \tag{2.2}$$

which is tracked by means of the cost function in (2.3):

$$g_1 = [\psi_s^{ref} - \psi_s(k+1)]. \tag{2.3}$$

Thus, torque is no longer a control variable in the cost function. Using g_1, the reference stator voltage can also be obtained, based on which the voltage vector closest to its value will be chosen, identifying the sector in which it is located. The simplified MPC is compared with an FOC to verify the validity of the proposed solution. From the simulations performed, it can be seen that there is a lower THD value with the MPC control than with the FOC control, with a cleaner phase current pattern and lower ripple. Furthermore, the electromagnetic torque effectively follows the desired reference value without deviations.

2.2. Open-end winding PM synchronous motor

2.2.1. System configuration with single DC voltage source

A novel direct torque control (DTC) strategy, for driving an OW-PMSM motor based on the suppression of zero-sequence current by an additional hysteresis control, is presented in [8]. This particular current is present in the system as the motor is powered by a common DC source, as seen in Fig. 2.5.

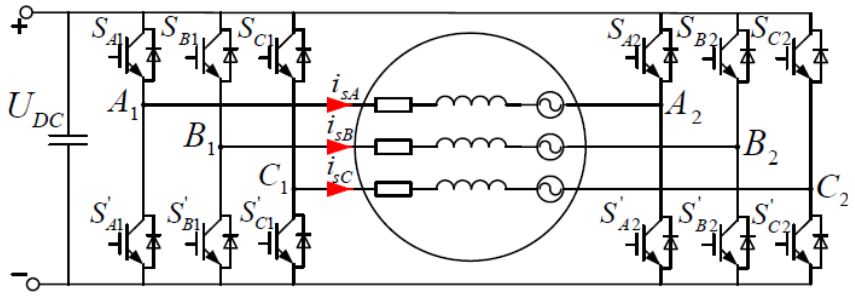

Figure 2.5: Control block of the proposed strategy [8].

Although this solution has several benefits in terms of cost, weight, and volume, it has the disadvantage of introducing a zero-sequence current path. This current can only be suppressed if zero-sequence voltage vectors (ZSV) are selected, thus avoiding an increase in system losses and a limitation of the maximum output power. To do this, if the zero-sequence current is less than 0 in the current sector, it must be increased in the next sector by selecting voltage vectors with positive ZSV. Otherwise, with a zero-sequence current greater than 0, voltage vectors with negative ZSVs must be selected.
Furthermore, the output voltages are selected to maintain the linear modulation range as wide as possible. In order to do this, additional voltage vectors need to be synthesised, resulting in a voltage vector diagram divided into 12 sectors. Compared to a conventional DTC, the one proposed in the paper therefore has a more complex optimal switching table and the system has an additional hysteresis control for the zero-sequence current, in addition to the torque and flux ones.

Comparing the two types, it can be seen from the simulations performed that the proposed control significantly reduces the phase current THD and retains all the advantages of the classic DTC, i.e. fast dynamic response, and structural simplicity.

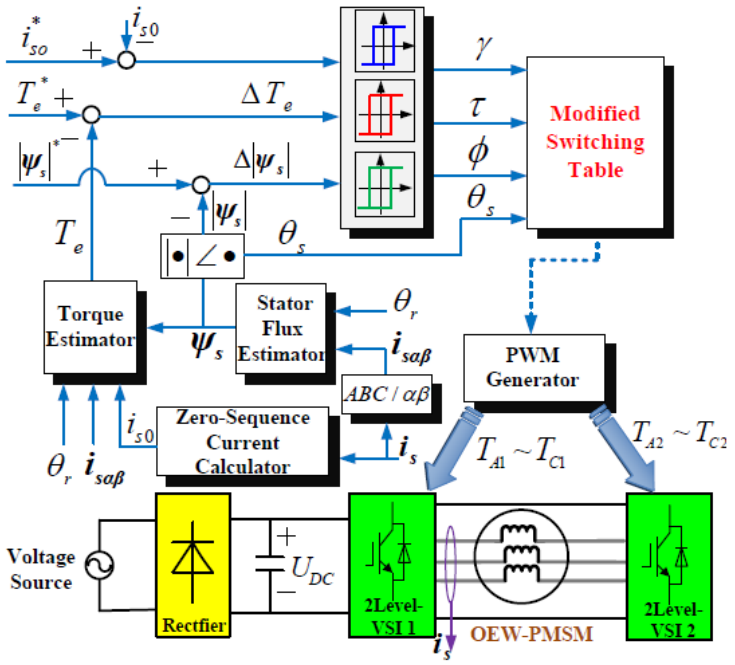

Figure 2.6: Control diagram of the novel DTC [8].

Three different control strategies applied to an open-end winding PMSM connected to a single dc link are proposed in [9]: Zero Space-Vector Modulation (Z-SVM), Conventional Modulation with an Additional Voltage Limitation (VL-PWM), Zero-Sequence Harmonic Component (ZSHD). For each method, a different control scheme will be implemented, from which the reference voltages V_d^*, V_q^*, and V_o^* will be obtained, which are used to calculate a suitable modulation, as can be seen in Figure 2.7.

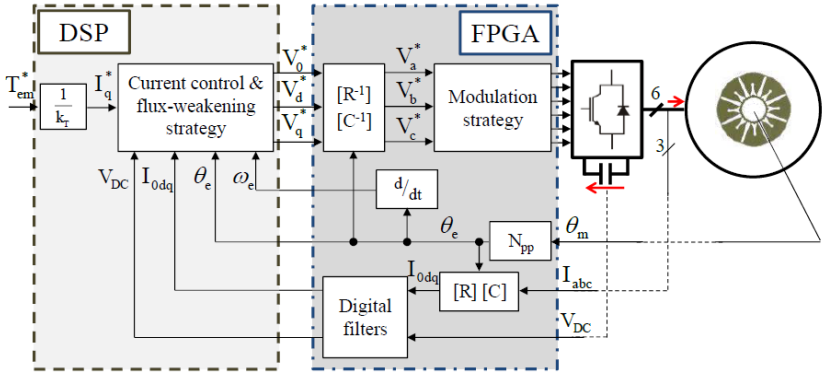

Figure 2.7: General control scheme [9].

The first method in Figure 2.8 is based on selecting voltage vectors with an instantaneous zero-sequence component equal to 0, which makes the zero-sequence current dependent only on the machine parameters. Six of these vectors form a hexagon which sets the limit equal to $\sqrt{3/2}pu$ in the $\alpha\beta$ plane. The control system associated with this method

involves the saturation of the q-axis reference current, which is also derived from the d-axis current, obtained from the flux-weakening controller. By simulating this control, it can be seen that even though the high-frequency zero-sequence current has been reduced to zero, there is still the third-harmonic component responsible for various losses in the system.

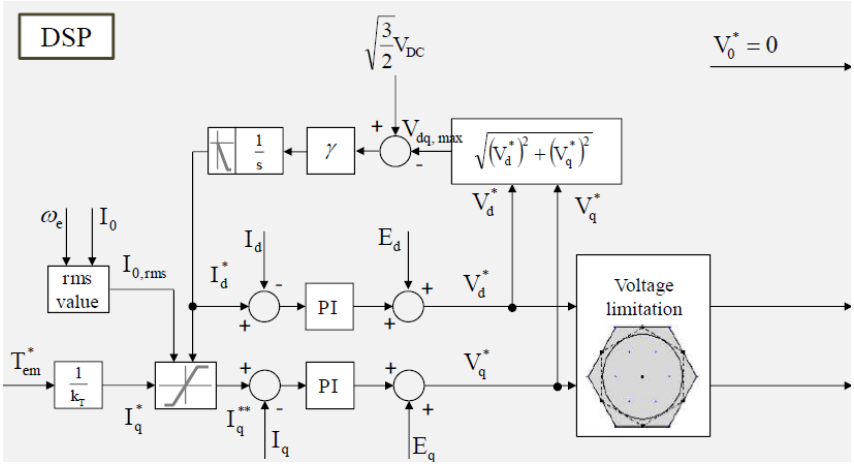

Figure 2.8: Control block for the Zero-Space Vector Modulation (Z-SVM) [9].

In the second method in Figure 2.9, the effects of a zero-sequence voltage reference different from zero are analysed and this will affect the maximum voltage limits, which will vary from the previous case. In addition, the zero-sequence current will also be present as it will be handled by a PI controller and emf compensation. With this strategy we have high-frequency zero-sequence current, but the joule losses caused by the third harmonic are negligible.

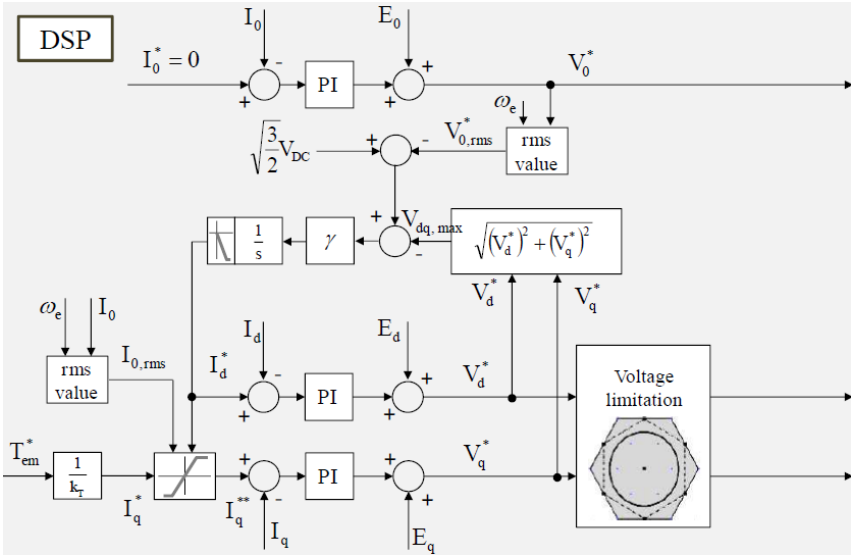

Figure 2.9: Control block for the Voltage-Limited PWM (VL-PWM) [9].

The last control proposed aims to determine the value of k_1 (amplitude of the fundamental harmonic) that maintains the phase voltage (in Equation (2.4)) at equal to 1, for given values of k_3 and $\phi_{1,3}$ (the amplitude of the third harmonic and the phase shift between the two harmonics, respectively):

$$V_a = k_1 \sin(\omega t) + k_3 \sin(\omega t + \phi_{1,3}). \tag{2.4}$$

This method is implemented in the control by means of a lookup table that receives as input k_3 and $\phi_{1,3}$ and outputs the value of k_1, which is multiplied by the value of the DC link voltage to find the maximum fundamental voltage dq.

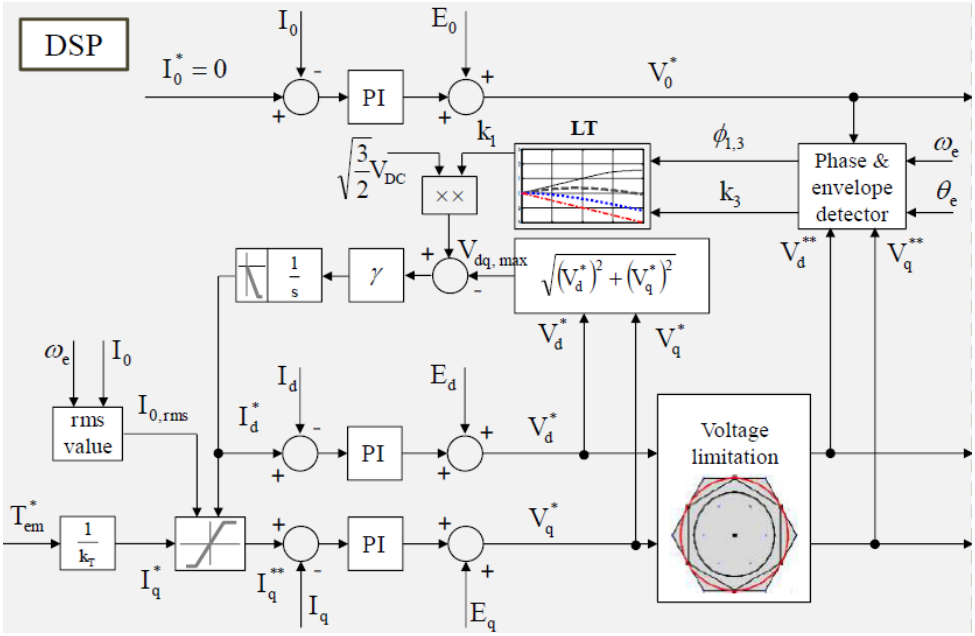

Figure 2.10: Control block for the Zero-Sequence Harmonic Detection (ZSHD) [9].

At last, the three different methods were compared by means of some suitable simulations. It is analysed in the paper that the ZSHD control has greater efficiency in the flux-weakening region and better performance in terms of maximum torque than the other two methods. The proposed ZSHD strategy is better than the Z-SVM for two main factors: the zero-sequence voltage leads to an increase in the fundamental component, and a lower zero-sequence current allows lower Joule losses and a torque without reduction. The latter point, however, is highly dependent on the electrical parameters, which greatly affect the performance of the machine. Furthermore, the third strategy also allows better utilization of the DC link by avoiding inverter saturation.

Paper [10] presents a dual-space vector control capable of suppressing zero-sequence current in a system consisting of an open-end winding PMSM motor fed by a dual inverter configuration with a common DC source. This technique aims to suppress the zero-sequence voltage via a switching combination capable of not creating this type of voltage and thus to synthesise the reference voltage. The combination found is implemented in the hexagon of the six-sector voltage space vector distribution, and in each of these a specific SVPWM modulation is defined. However, the zero-sequence voltage is also generated by the dead time of the inverter, which are only related to the current conducting modes, not the sectors.

The control strategy described in the paper implements to the conventional control scheme a closed-loop zero-sequence current controller, in which the reference is set to 0 and the error is regulated by a PI that produces a reference zero-sequence voltage.

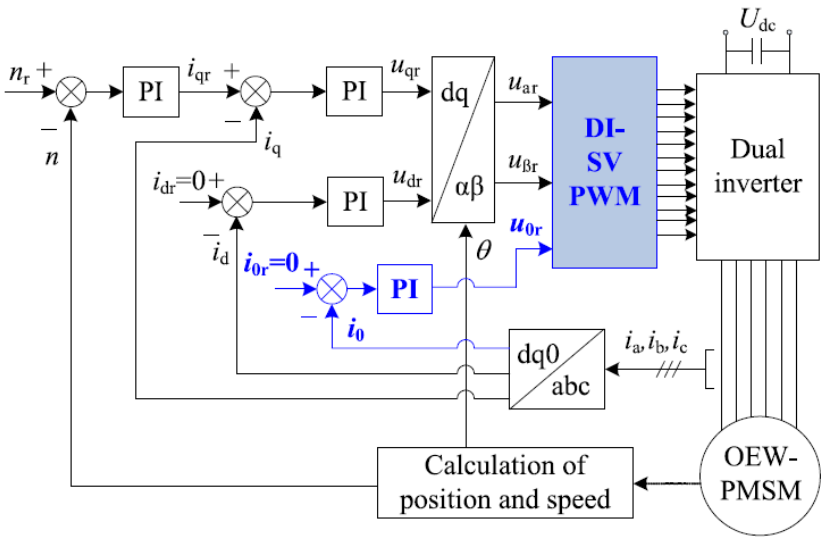

Figure 2.11: Control scheme for the proposed strategy [10].

The latter represents the third input for the novel DI-SVPWM together with the two voltages of the reference system $\alpha\beta$. It is responsible for suppressing the zero-sequence current via a closed loop by regulating and controlling the zero-sequence voltage. In the DI-SVPWM algorithm, each sector is subdivided into six further subsectors and two main steps are included. The first identifies which sector the reference vector is positioned in and decomposes it into two segments (e.g. OU=OX+XU), while the second identifies which subsectors the XU segment is positioned in and implements the SVPWM in that subsector. Using this technique, the paper demonstrates that zero-sequence current and voltage are effectively suppressed, reducing distortion on phase currents and voltages.

2.2.2. System configuration with independent DC voltage sources

[11] focuses on the control of a three-phase open-end winding SMPMSM at high speeds and therefore in the flux-weakening region. The proposed configuration is a dual-inverter power supply with two isolated dc-links. These are composed of an engine generator supplying the inverter1 and a battery connected to the inverter2, as depicted in Figure 2.12.

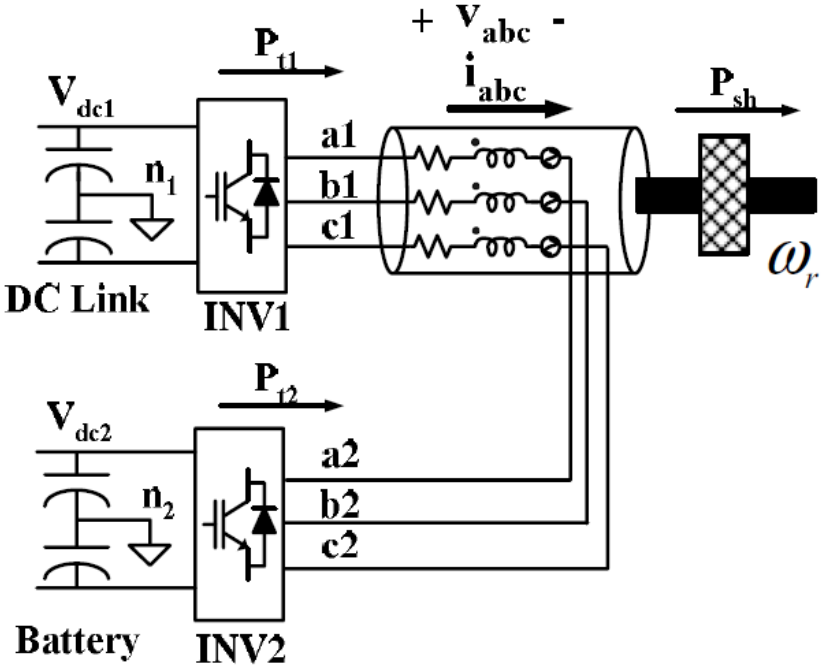

Figure 2.12: Open-end winding PMSM with two isolated inverters [11].

In this way, the power flow between the two sources can be controlled independently, thus also having direct control over the torque, which is proportional to the stator current of the q-axis. The proposed flux-weakening control is based on the voltage quadrature method. Indeed, if the power of inverter2 is zero, the voltage vector applied to the machine of side2 must be perpendicular to the current vector. The power of inverter2 is controlled by the current controller. It calculates the voltage vectors that must be applied to the machine after having received as input the reference voltage obtained from the current command of axis-q. As a result, the amplitude of the voltage vector supplied by inverter1 becomes minimal, while inverter2 supplies all the reactive power that the motor requires.

As the speed increases, the axis-d current must be modified to reduce the flux amplitude so as not to exceed the voltage limits imposed by the dc-link. This results in flux-weakening control which, as mentioned above, has the task of calculating the two inverter voltages through the current controller.

If the voltage of inverter2 reaches the maximum admissible value, its amplitude will

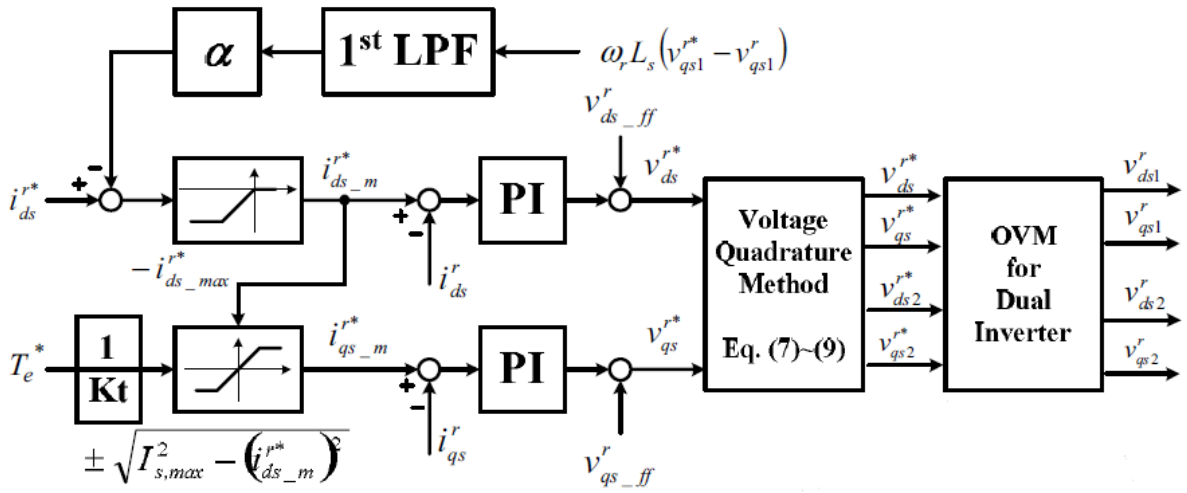

Figure 2.13: Block diagram for the flux-weakening control [11].

remain fixed, while the angle will be modified appropriately to vary the output power of the inverter. Next, the voltage supplied by inverter1 is calculated. Based on the difference between the reference voltage vector and the one obtained, the axis-d current will be modified. Using this method, all the power flow to the motor will be supplied by inverter1, since that of inverter2 is maintained at zero for the whole operating period.

The results obtained by applying the proposed method show a 15% increase in torque compared to the control of a conventional Y-connected motor. The maximum applicable voltage for current control is also increased by 15%. Finally, it can be seen that the power output of the inverter2 is effective at zero all the time and that there is an improvement in the capability curve.

A hybrid PWM based on flux-weakening control strategy for an OW-PMSM is presented in [12]. The motor is fed by two voltage source inverters, the first one powered by a dc voltage source called main inverter (MI) and the other one connected to a floating capacitor, called compensation inverter (CI).

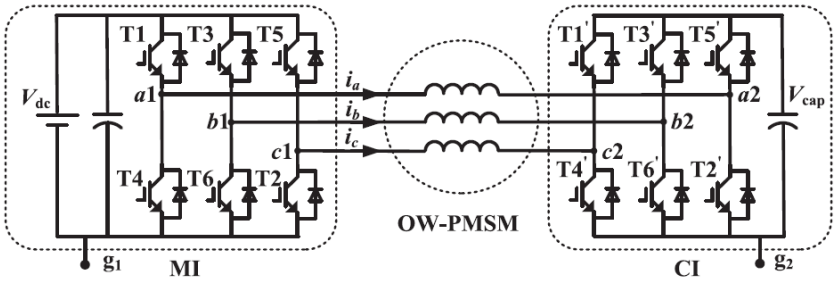

Figure 2.14: Open-end winding PMSM driven by a hybrid-inverter (MI and CI) [12].

The CI can boost the DC link voltage and increase the speed range if an appropriate control is implemented. For MI a double-vector based PWM is applied while for CI a conventional SVPWM is used. Furthermore, flux-weakening control based on this hybrid PWM strategy is implemented with PI controller to achieve demagnetizing current to lower the back emf and to improve the utilisation of the dc link. In the proposed strategy, the MI provides all the power required by the motor, both active and reactive, and the CI has the only task to compensate the reactive power. This therefore requires an accurate synthesizing of the voltage vectors generated by the two inverters.

The double-vector PWM uses only an active vector and a zero vector in a switching period to synthesise the voltage vector (VMI) that can provide the required active voltage. This method reduces switching losses by approximately one third compared to a conventional SVPWM. In addition to the active voltage MI also provides the reactive voltage, which must be accurately compensated by the CI, in order to avoid dangerous stator current harmonics that could damage the machine. To properly synthesise the voltage generated (VCI) by the compensation inverter, the SVPWM method is used. If VMI coincides with the voltage vector required by the motor, then VCI will be set to zero.
Moreover, a field-weakening control based on the PWM hybrid strategy is also implemented in the system, which uses the duration of the active MI vector as feedback. The complete control system also includes a speed control loop and two current controllers. Instead, the reference currents of the two axes are calculated using an MTPA algorithm. The PI for field-weakening control provides a negative d-axis current to counter the saturation or supplies a zero output if the flux-weakening region is not reached. Combined with the PI, that controls the q-axis current so as to remain within the saturation limits, they generate the voltage references that will then be transformed into the active and reactive control voltage. Finally, these will be appropriately processed to derive the inputs of the two modulations explained above, obtaining the switch signals to be sent to the MI and IC. The overall machine control is shown in Figure 2.15.

In the simulations performed, the proposed method is compared to the conventional case of SVPWM modulation for both inverters. It can be seen that switching losses are effectively reduced by one third with the hybrid PWM and the flux-weakening control. In addition, 9.09% higher output power was achieved due to the increased utilisation of the dc link in the FW region. Experimental studies on a test bench were also carried out, which confirmed the validity of proposed control strategy since it improves the efficiency and performance of the system while maintaining a THD value similar to conventional control.

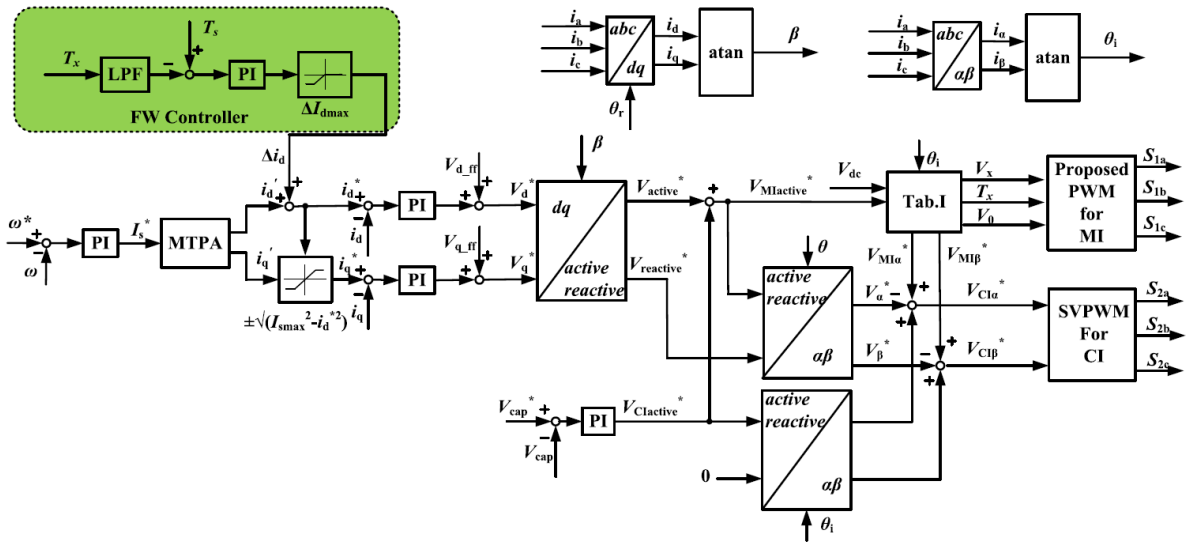

Figure 2.15: Complete block diagram for the hybrid-inverter [12].

A speed control for an open-end winding PMSM fed by a dual inverter is presented in [13]. In this case the second inverter is fed by a floating capacitor able to extend the speed range of the motor, reducing the current ripple. For proper system operation, the torque must be limited by the maximum current value due to the thermal constraints of the machine. In the region beyond the base speed, the available voltage must also be limited by the DC-link voltage of the inverters, which depends on the modulation strategy.
This paper deals mainly with the control of the floating capacitor. Through the q-axis output voltage of the floating bridge, it is possible to control the reactive power supplied by the inverter2. It is used to null the reactive power of the other inverter, maximising the active power flow. It is also shown that with the system adopted, it is possible to increase the maximum speed value achievable by the motor. Indeed, it can be calculated that the maximum speed is extended by a value equal to the ratio of the voltages at the DC-links of inverter2 and inverter1, compared to the single inverter configuration.
A field-oriented control (FOC) is proposed for the control of the system, in Figure 2.16, and can be divided into two main sections: the first one concerns the control of the first inverter connected to the battery (green box), while the second one focuses on controlling the DC voltage of the floating capacitor and compensating the reactive power absorbed by the motor (purple box).
Two PI regulators are used for the inverter1, which control the two current components and output the voltage values, which will be compensated with the back-emf to obtain the reference voltage values. Also included in this part is the flux-weakening control, in which another PI defines the d-axis current reference, after comparing the inverter voltage with the maximum allowed value.

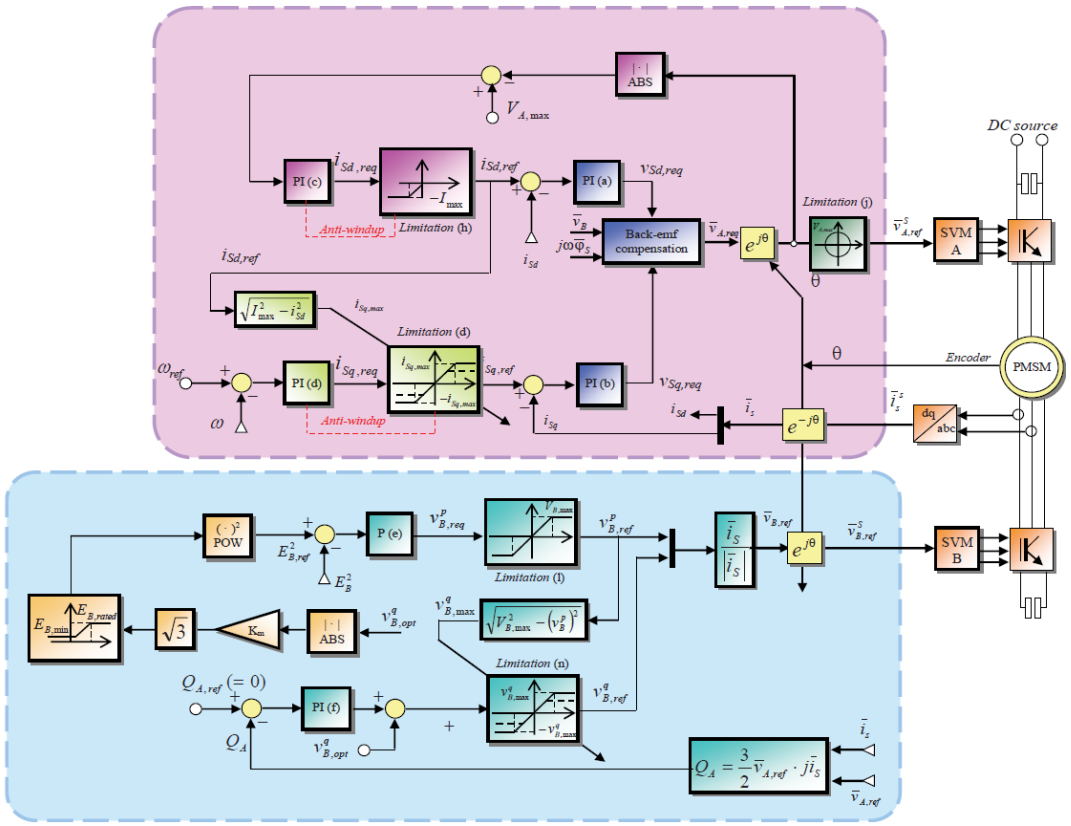

Figure 2.16: Complete control block diagram for the OW-PMSM system [13].

The current value obtained will also be used in the saturation to compute the q-axis component. Instead, two other PI regulators were used to control the DC-link. One has the task of maintaining the voltage at the reference value, while the other has the task of improving the dynamic performance and ensures that the inverter1 works at a unity power factor, setting the reactive power generated by the inverter itself to zero for the entire period. From these two different sections of the control, the voltage reference values of the two inverters are derived, which are sent to the modulation, consisting of space vector modulation in both cases.

The results of the laboratory experiments show an increase in both the maximum speed of the machine and the constant power speed range, compared to the single inverter configuration. Furthermore, the increased current quality and reduced switching losses confirm the validity and effectiveness of the proposed strategy.

One of the main problems of the dual-inverter configuration is the high switching losses due to the presence of 12 power semiconductors. In [14], advanced discontinuous pulse-width modulation (DWPM) is proposed to reduce these losses by more than 30% in high-power applications, leading to better system efficiency compared to space vector

PWM modulation, as there are smaller power factor variations. Figure 2.17. shows the operating diagram of the proposed control which, contrary to a conventional DWPM, generates the offset voltage based on the phase angle of the current θ_i and the rotorθ_r, instead of using the reference phase voltage, as shown in the Table 2.1:

Reference angle (θ_i^*)	Offset voltage inverter1	Offset voltage inverter2
$-\pi/6 < \theta_i^* \leq \pi/6$	$-v_{as1} + 0.5V_{DC1}$	$-v_{as2} + 0.5V_{DC2}$
$\pi/6 < \theta_i^* \leq \pi/2$	$-v_{cs1} + 0.5V_{DC1}$	$-v_{cs2} + 0.5V_{DC2}$
$\pi/2 < \theta_i^* \leq 5\pi/6$	$v_{bs1} + 0.5V_{DC1}$	$-v_{bs2} + 0.5V_{DC2}$
$5\pi/6 < \theta_i^* \leq -5\pi/6$	$-v_{as1} + 0.5V_{DC1}$	$-v_{as2} + 0.5V_{DC2}$
$5\pi/6 < \theta_i^* \leq -\pi/2$	$-v_{cs1} + 0.5V_{DC1}$	$-v_{cs2} + 0.5V_{DC2}$
$\pi/2 < \theta_i^* \leq -\pi/6$	$-v_{bs1} + 0.5V_{DC1}$	$-v_{bs2} + 0.5V_{DC2}$

Table 2.1: Offset voltages for the two inverters.

Where θ_i^* is the reference angle:

$$\theta_i^* = \theta_i + \theta_r = tan^{-1}\left(\frac{I_d}{I_q}\right) + \theta_r. \tag{2.5}$$

The offset voltages of the two inverters will then balance the phase voltages (v_{as}, v_{bs}, v_{cs}), calculated in Equations (2.6), (2.7), to obtain the reference voltages (with x=a,b,c):

$$v_{xn1} = v_{xs1} + v_{offset1}, \tag{2.6}$$

$$v_{xn2} = v_{xs2} + v_{offset2}. \tag{2.7}$$

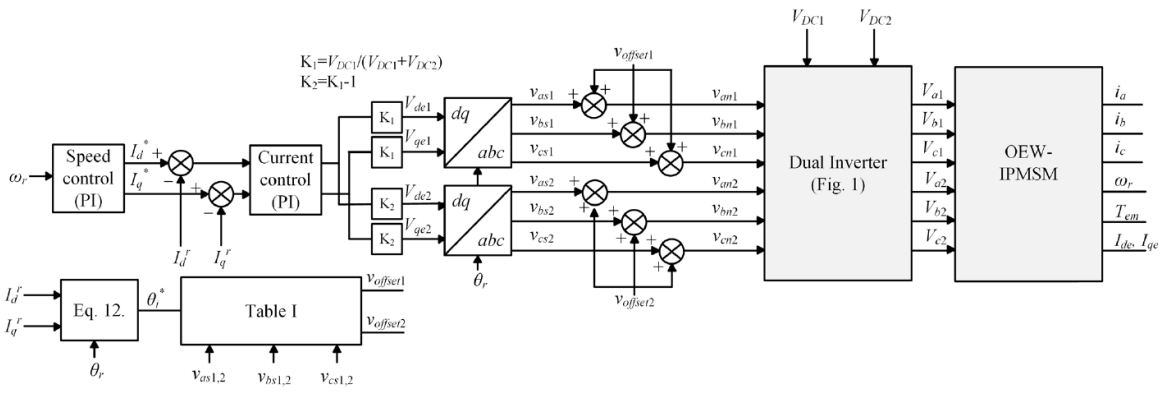

Figure 2.17: Block diagram of the analysed DPWM [14].

Thus, when the phase current changes, the DWPM changes the reference voltage, which is applied at the maximum current point.

To verify the real advantages of the proposed solution, it was compared in simulations with the conventional DWPM and SVPWM. From the results obtained, it can be seen that under all simulated conditions, the analysed method has the lowest switching losses, a higher system efficiency and also a greater reduction in THD.

2.2.3. Control systems for EV traction applications

In [15] each inverter is connected to a different independent source, more precisely an energy conversion device (power battery) supplies the primary inverter, and an energy storage element (floating capacitor) is connected to the secondary inverter, represented in Figure 2.18. The capacitor's task is to work as a power buffer, i.e. to compensate for the lack of power required by the load and to absorb instantaneous power fluctuation outputted by the primary source. This paper also defines a precise method for obtaining the desired power exchange between the two sources, based on first order inertial element. The calculator is based on the difference between the input power of the motor P_{mot} and the optimal output power of the inverter1 for which the maximum battery efficiency $P_{inv1opt}$ is set as a constant. The output of this controller corresponds to the desired power output of the first inverter, P^*_{inv1}, as illustrated in Figure 2.18.

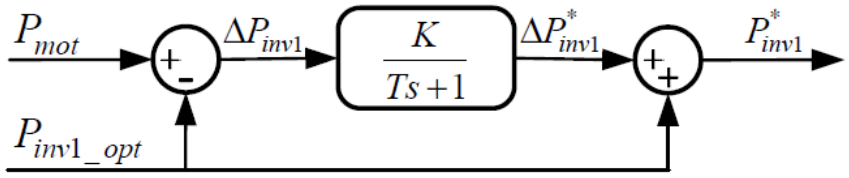

Figure 2.18: Calculation diagram of desired power for the inverter1 [15].

By varying the parameters K and T, the power sharing characteristic can be modified, changing the amplitude and speed/sensitivity of the response of ΔP^*_{inv1} respectively. In addition, a selection strategy is introduced between the three modulation methods: low switching frequency (LF), accurate power flow (AF), linear partitioning (LP).

The first proposed method is based on forcing the inverter1 to supply only basic voltage vectors or null vectors to minimize the system's switching losses as much as possible. The candidate vector $\vec{u}^*_{s1}$ is chosen from those that match the output power of inverter1 as closely as possible. The voltage of inverter2 $\vec{u}^*_{s2}$ calculated as the difference between $\vec{u}^*_{s1} - \vec{u}^*_{s2}$ must be contained within the modulation range of inverter2. If yes, $\vec{u}^*_{s1}$ is valid, otherwise, the next candidate vector must be passed on.

Instead, the second method generates the desired voltage of inverter1 in phase with the stator current vector and the amplitude is determined from the desired output power of the same inverter. After that, it is checked whether the current found is within the limit of the modulation range of inverter1 and only if positive is it assigned. In other cases, the voltage must be brought back within the limits, and only after a suitable value has been found can the voltage of the second inverter also be calculated.
Finally, the third method is only used when the first two fail and is based on assigning the values of $\vec{u}^*_{s1}$ and $\vec{u}^*_{s2}$ by linearly partition of $\vec{u}^*_s$ maximizing the possibility of the two vectors lying in the feasible region of the two inverters.

Each of the three different methods provides evaluation indexes that correspond to a flag F set to 1 if the corresponding method is available or 0 otherwise, and the difference D_{Pinv1} between the power of inverter1 calculated using $\vec{u}^*_{s1}$ found and the desired power $P*_{inv1}$. The last index that is evaluated is how much the method succeeds in reducing the total switching losses in the system.

The method selection strategy is mainly based on these three indices, from most to least important in the order in which they have been listed. The diagram in Figure 2.19 effectively summarizes what has already been said.

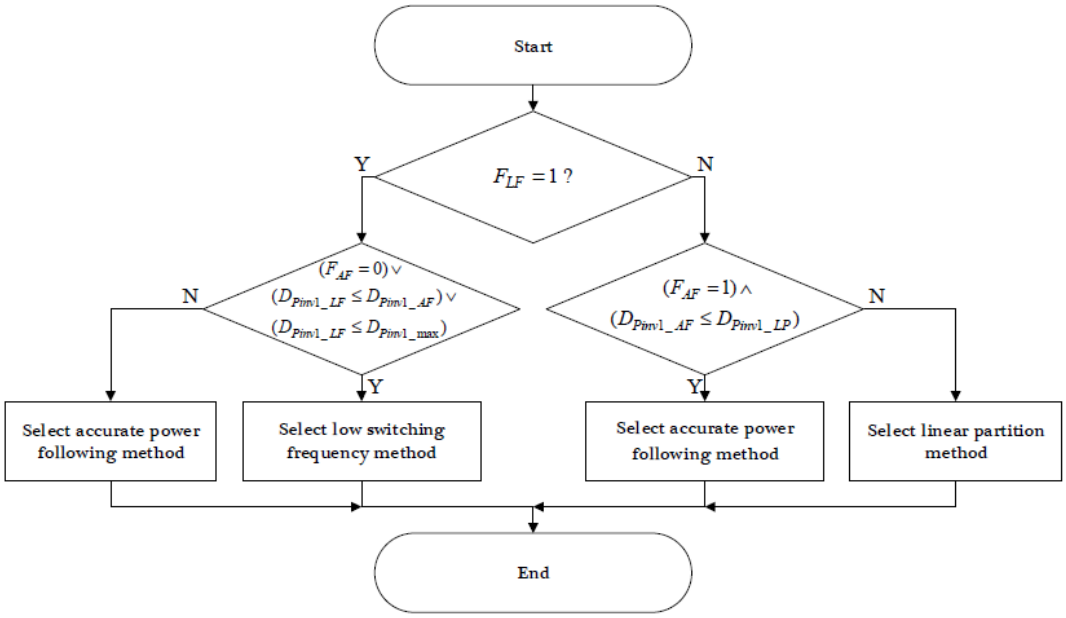

Figure 2.19: Voltage vector distribution method selection strategy diagram [15].

The proposed control system is similar to that of Figure 2.1, to which the block for calculating the desired power P^*_{inv1} is added:

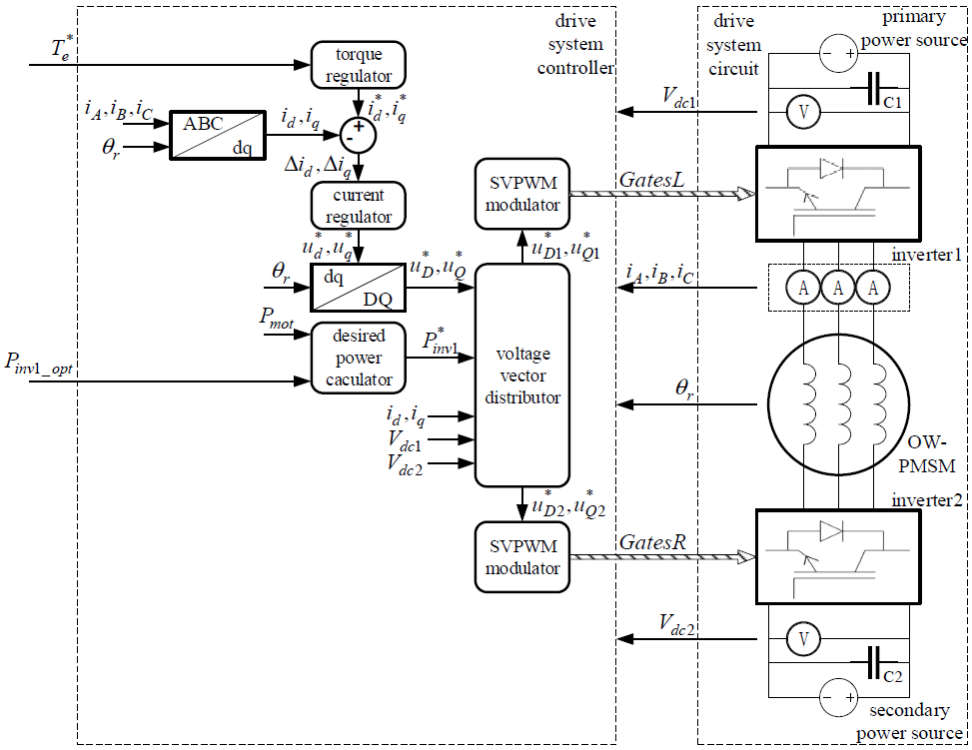

Figure 2.20: Overall configuration scheme of the proposed solution [15].

The ideal stator current $\vec{i}^*_s$ is instead calculated in the torque regulator, using the maximum torque per ampere method (MTPA) in the constant torque region and through the constant back emf method in the flux-weakening region. The stator current is then fed into a PI controller to obtain the reference voltages. They are handled by the voltage vector distributor and, only after having found the most accurate and convenient method, the two voltage vectors $\vec{u}^*_{s1}$ and $\vec{u}^*_{s2}$ are sent to the corresponding SVPWM modulators, that will generate the gate controls of the inverters.

The simulations carried out verify the validity of the proposed strategy. Both torque and motor speed quickly and smoothly track the desired values. Thanks to the power sharing calculation strategy and the voltage vector distribution method, it is possible to reduce the switching frequency and therefore also the losses, to increase the efficiency of the primary source energy and to recharge the second dc source when there is an excess of power generated by the inverter1.

A conventional PMSM motor drive is compared with a dual inverter drive in [16]. It also demonstrates the usefulness of the boost converter modules to increase the DC link value at high speeds, resulting in greater efficiency. In this way, the speed range will also

increase, resulting in higher torque and lower conduction losses. The control algorithm is divided into determining the control torque and current, calculating the stator voltage required to obtain these torque and current values using the MTPA method, dividing this voltage into the two references for the two inverters, and generating the battery current control to adjust the DC link voltage. The system in Figure 2.21 is used to perform these operations.

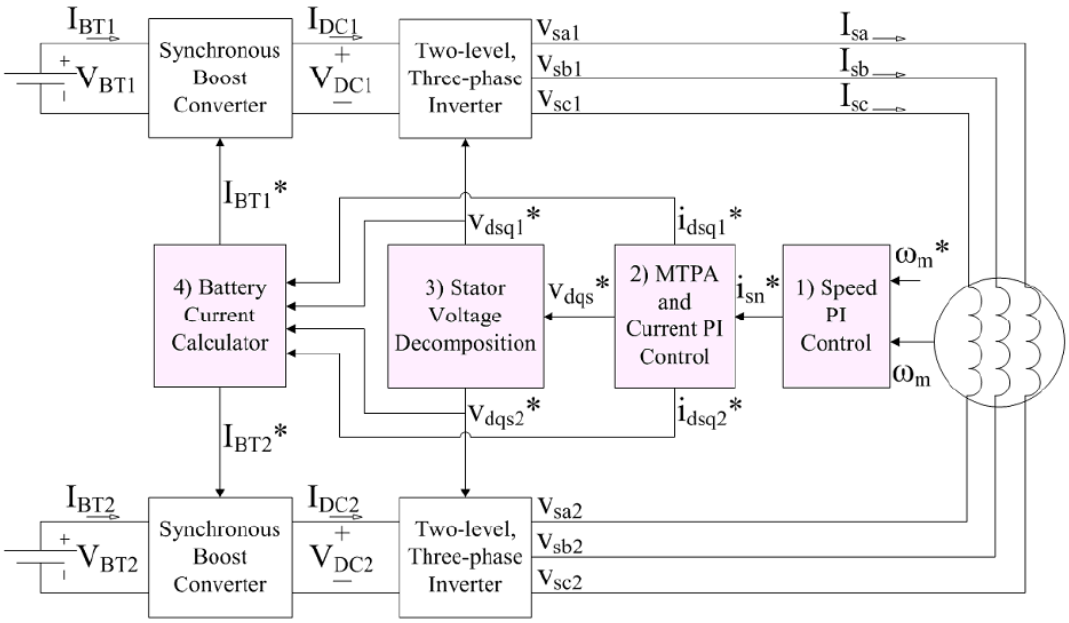

Figure 2.21: Open-end winding PMSM fed by dual-inverter with boost converters [16].

In the constant torque operating area, i.e. below base speed, only MTPA acts without the need of a boost converter. Above this speed there is the flux-weakening region, also known as the constant torque region. By using a boost converter, the DC link voltage is increased, which allows the stator current to remain on the trajectory of the MTPA, also beyond the base speed, where the maximum possible torque becomes proportional to the speed itself. Comparing this method with flux-weakening control, it can be seen that by increasing the voltage at the DC link through the boost converter, more torque can be achieved at higher speeds with a more efficient use of current, reducing the conduction losses.

In [17], an open-end IPM motor is powered by two three-phase inverters connected to two separate electrically isolated sources. Inverter1 is connected to a fuel cell or generator and inverter2 to an energy storage element such as a battery. The total power flow of the load is given by the sum of the powers of the two inverters:

$$P_L = P_{c1} + P_{c2}, \tag{2.8}$$

$$P_{c1} = \frac{3}{2}(v_{q1}i_q + v_{d1}i_d), \tag{2.9}$$

$$P_{c2} = \frac{3}{2}(v_{q2}i_q + v_{d2}i_d). \tag{2.10}$$

Three different methods are proposed to simultaneously control both the motor output power and the power flow between the two DC voltage sources. The first is based on controlling the power supplied from the battery to the load in order to maximise the power flow in the inverter2 by making it work at unity power factor. The primary source, on the other hand, will behave as a slack bus producing the necessary power to overcome the power of the second inverter, lost power, and load. With these constraints, the reference voltages for the space vector modulation of the two inverters can be derived. The second method proposed is based on supplying all the power required by the motor from the inverter1 while the secondary one supplies only the reactive power consumed by the load. To do this, the voltage of inverter2 is in quadrature with the motor current and is therefore called the voltage quadrature method. The last control presented is the optimum inverter utilization in which the voltages of the two inverters are co-linear and proportional to the desired power. The commanded voltages for the two inverters are calculated using the power equations written above, and used in the control diagram in Figure 2.22.

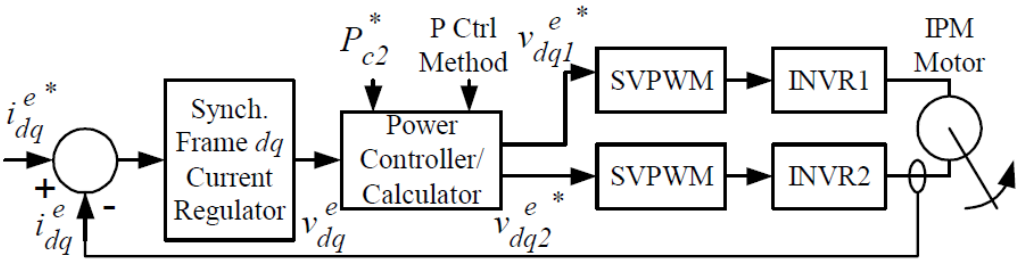

Figure 2.22: Control block of the proposed strategy [17].

A closed-loop current controller was used for the control system, which delivers the values on the desired dq-axis voltages. These correspond to the input of the open-loop power regulator whose task is to provide the commands for the two inverters via two separate

SVPWM modulators. The simulations show that the current is well regulated with all three proposed methods. In particular: with the unity power factor, the motor works at a stable point despite the voltage being subject to step changes, with the quadrature control, it can be seen that the inverter2 is actually generating a voltage in quadrature with the current, and with the inverter optimal utilisation control, it can be seen that the powers of the two sources can be controlled independently.

An application of the OW generator in a hybrid vehicle, connected in series with an ICE and driven by a dual inverter, is examined in [18]. The configuration adopted also includes two additional motors connected both to the wheels (R and L), and to two separate dc links each powered by a battery, represented in Fig. 2.23.

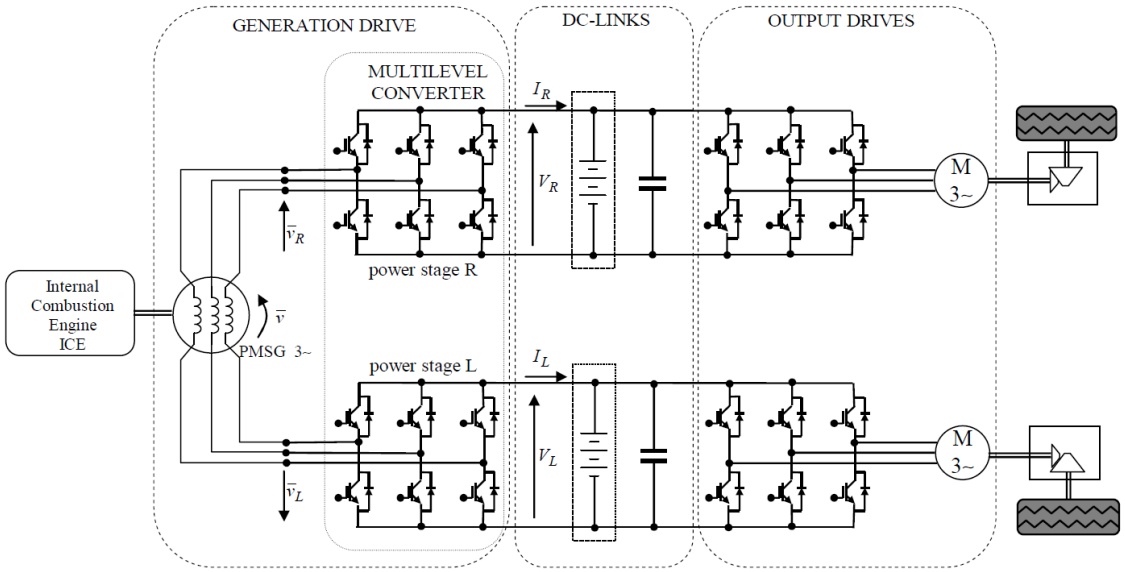

Figure 2.23: Overall configuration of the system investigated [18].

The control structure of the system is divided into high-level and low-level control. The former in Figure 2.24 has the task of calculating the reference powers to be supplied by the generator. It consists of an outer loop that must control the value of the voltages at the two dc-links, and then there are the PI regulators that generate the reference currents that should flow output from the multilevel converter, which is connected to the generator system. They are then used to calculate the electrical reference powers P_R^* and P_L^*, the sum of which corresponds to the power that must be generated P_g^*. Two lookup tables with torque and speed mappings are employed to find the optimum operating point for a given Pg. These values are sent to the ECU (speed) and PMSG (torque).

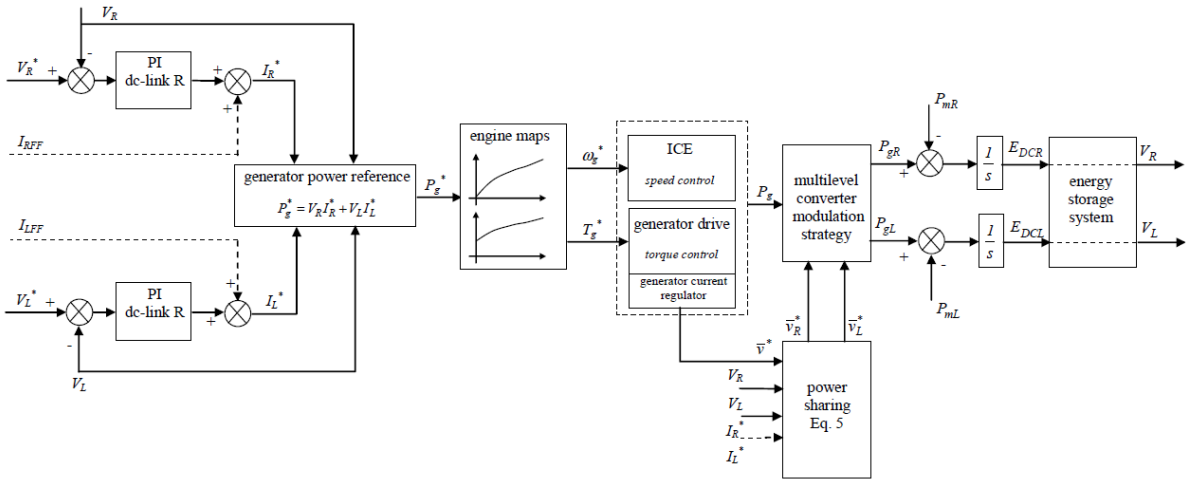

Figure 2.24: High-level control algorithm for the hybrid vehicle [18].

Instead, low control is based on the modulation strategy of the converter, which must be able to efficiently handle the power demand from both sides. In this multilevel converter, the voltage $\bar{v}_R$ and $\bar{v}_L$ applied to the generator are derived from 18 output active voltage vectors and one null. These are then used to calculate the electrical reference powers P_R^* and P_L^*, the sum of which corresponds to the power to be generated P_g^*. Two lookup tables are used, containing the torque and speed maps, required to find the optimum operating point for a given Pg. These values are sent to the ECU (speed) and PMSG (torque).
Instead, low control is based on the modulation strategy of the converter, which must be able to efficiently handle the power demand from both sides. In this multilevel converter, the voltage $\bar{v}_R$ and $\bar{v}_L$ are derived from 18 output active voltage vectors and one null and applied to the generator. To do this, the voltage vector $\bar{v}^*$ is synthesised from the three phase voltage vectors, the two components R and L, assumed to be in phase and in the same sector, are derived. An appropriate duty-cycle is calculated, and a loss-minimising switching sequence is defined. Furthermore, the dual-inverter must separate the total generated power appropriately and according to the demands of the two output drives.
From the simulations carried out in the paper, it can be seen that with the type of control adopted fast dynamic responses are obtained, the voltage value of the DC links remains similar to the nominal value, and the modulation strategy functions correctly, showing the capability of the proposed system.

Another technique for controlling open-end winding PMSM motors called PTC (predictive torque control) is described in [19]. As well as giving accurate results and being less complex, this type of control is able to reduce torque and flux ripples. The conventional PTC is based on 4 main steps: measurements, estimations, predictions, and optimisation.

The stator voltage and current are measured, while the stator flux is estimated as it is not measurable, and predicted together with the torque and current, by means of appropriate formulas in the following k steps. Using these values, the cost function G_n is defined and optimised. Since it is generated by combining the torque and flux equations and has very different quantities, the weighting factor comes into play, which must be set appropriately to avoid high torque ripples that could affect motor efficiency. Finally, the voltage vector that minimises this formula is selected and transmitted to the gates of the dual-inverter. In the proposed strategy (Figure 2.25), two cost functions are used to avoid the use of the weighting factor in the Equations (2.11) and (2.12):

$$G(T) = [T^*_{em} - T_{em}(k+2)n], \tag{2.11}$$

$$G(\lambda) = [\lambda^*_s - \lambda_s(k+2)n]. \tag{2.12}$$

In the first, the voltage vectors that minimise voltage ripples are obtained, while in the second cost function, the vectors that minimises flux ripples are found. The optimal voltage vectors generating lower flux and torque ripples are applied to the cost function G (2.13), finding the gate signals of the two inverters:

$$G = min\{G(T)\} + min\{G(\lambda)\}. \tag{2.13}$$

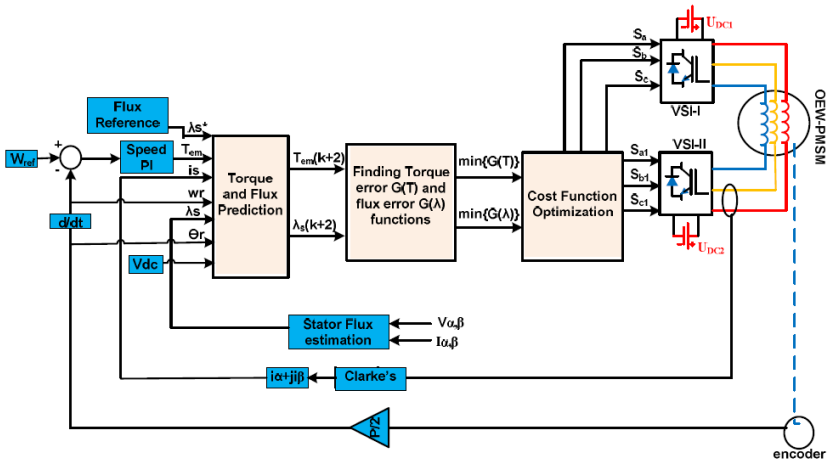

Figure 2.25: Block scheme of the proposed predictive torque control [19].

From the simulations performed, it can be seen that the proposed PTC achieves a 42% reduction in torque ripples and improves the speed of the system's dynamic response compared to the conventional strategy. It is also simpler to implement and does not contain the weighting factor selection algorithm, which is a heavy and critical process.

In [20], a dual inverter driven OW-PMSM system powered by a battery and a flying capacitor on the two different sides is analysed. A hybrid modulation method consisting of a six-step for inverter1 and a PWM for inverter2 was chosen to obtain the maximum power output.
The drive system must be able to regulate the torque/speed of the machine and the flying dc-link voltage. For the former, it is necessary to adjust the active and reactive power consumed by the machine, while for the latter, it is required to keep the inverter2 power flow value at zero. To do this, the output voltage vector of the inverter must be kept in quadrature with respect to the current vector. Furthermore, to maximise the active power output, the reactive power of inverter1 must also be kept at zero. Therefore, all the reactive power of the motor will be supplied by the flying inverter.

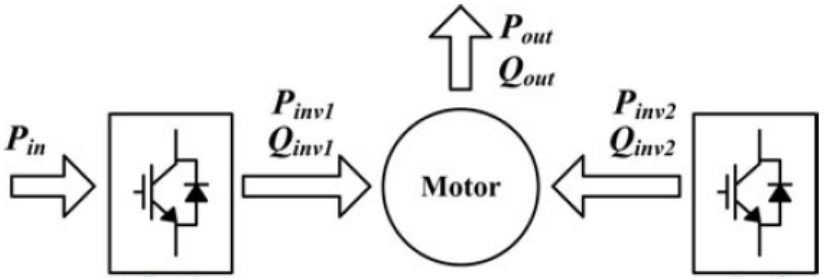

Figure 2.26: Power flow scheme in the proposed system [20].

In this paper, the six-step is proposed as the modulation method for inverter1. It reduces switching losses and generates the maximum output voltage, which is 10% higher than conventional modulation techniques such as SVPWM, but at the same time it generates odd harmonics that cause torque ripple and affects efficiency. The hybrid modulation adopted solves this problem as the flying inverter has the task of compensating for the high order harmonics generated by the input side inverter, allowing for a pure sinusoidal voltage and current on the load.
Moreover, the six-step modulation of the dual inverter allows higher output power and torque values than other topologies in the high-speed region. In the low-speed region, on the other hand, it is impossible to use six-step modulation for inverter1 because the back-emf and active voltage required are not high enough. For this reason, the paper proposes a phase modulation and a transition around the base speed to six-step modulation. In the high-speed region, field weakening control through the voltage feedback method must also be implemented. It receives the reference output voltage and regulates its value via the d-axis current. This is also controlled, below the rated speed, through the use of an MTPA algorithm and kept at zero. In contrast to conventional control systems, a flying dc-link voltage controller is also used in this case, which consists of a PI controller that

supplies the required power to the dc-link that is subsequently converted to the active voltage reference of the inverter2. Two current controllers are also used to generate the d-axis and q-axis voltage references from which the active voltage reference is calculated. This is added to that obtained from the DC voltage controller, to obtain the active voltage reference of the input side inverter, as depicted in Figure 2.27. Only now the phase modulation can be applied to obtain the reactive voltage, and finally the reference voltage is processed by the six-step modulation.
The simulations performed verified the validity of the proposed control and the modulation method. More specifically, it can be seen that the waveforms are pure sine waves, the operating area of the dual-inverter is larger than the single inverter configuration, and the output power and efficiency of the system has been increased with the six-step.

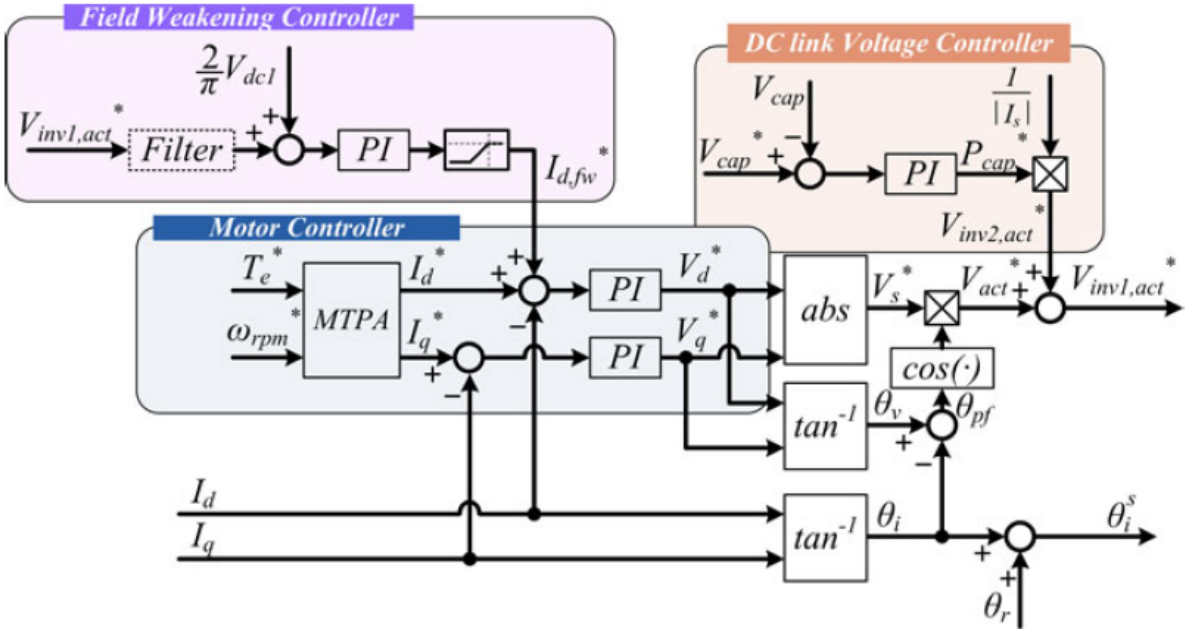

Figure 2.27: Motor, field weakening, and dc-link voltage controller [20].

The paper [21] presents a hybrid modulation for controlling an open-end winding PMSM motor fed by a dual-inverter. The proposed configuration uses two isolated dc sources to prevent zero-sequence current circulation, decreasing Joule losses.
For control at speeds lower than base speed, an MTPA algorithm is used to provide the minimum values of the d-axis and q-axis components of the stator current, in order to obtain the desired torque. At higher speeds this technique cannot be used. Therefore, flux-weakening feedback control is employed to increase the operating range. The vector control system also includes two closed-loop controls, one for current and one for speed. More precisely, from the velocity error is obtained the armature current control via a PI regulator, which is processed by the MTPA block.

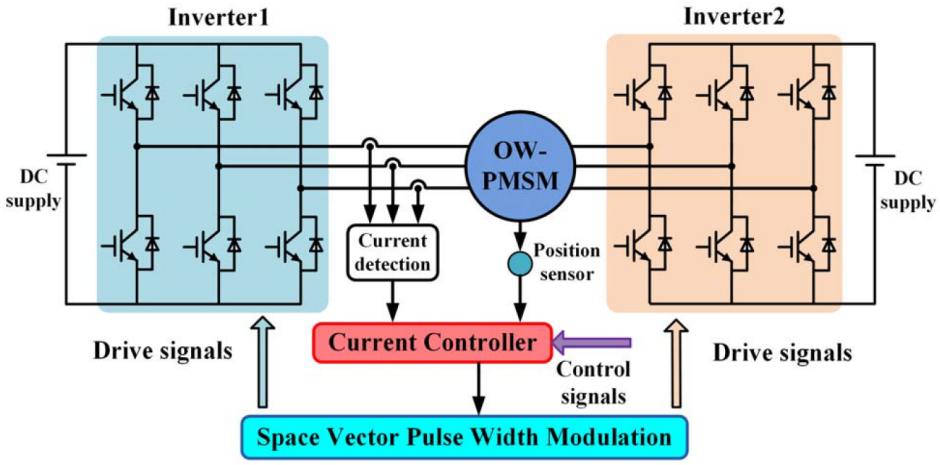

Figure 2.28: Open-end winding motor driven by a dual-inverter with isolated dc links [21].

Instead, the flux-weakening control receives the output voltage values from the two PI regulators. It handles them in such a way as to respect the voltage limits by adjusting the d-axis current. This current value is then used to delimit the saturation and to calculate the q-axis current. The overall control scheme implemented for the open-end winding motor is shown in Figure 2.29.

With respect to the generation of the switching states of the two inverters, the paper presents a hybrid modulation technique based on a lookup table combining six-step and PWM modulation. Therefore, the first inverter will work in six-step status based on the lookup table, while the second works as a compensating inverter. Six-step modulation is used to reduce switching losses and, at the same time, to maximise the output voltage.

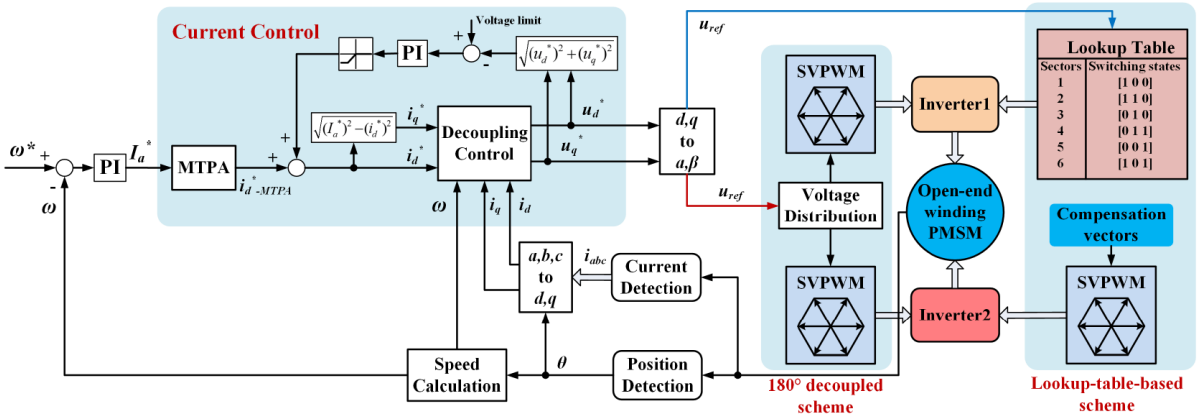

Figure 2.29: Overall diagram of the control scheme with comparison between the lookup table and 180° decoupled method [21].

Based on the position of the reference voltage vector, the sector in which it is located is

identified. Each sector corresponds to a vector of switching states which will control the inverter1, and the same sector also identifies the compensation vectors for inverter2. This vector defines the components of the reference vector for the second inverter, which will be sent to the space vector pulse width modulation.

The final simulations show that for speeds lower than base speed, there is an improvement in current THD and a lower torque ripple than in the 180° decoupled scheme. In the flux-weakening region, on the other hand, switching losses are effectively reduced, while torque and speed quickly track the reference value. Furthermore, the lookup table scheme allows efficient modulation of the spatial vector with reduced computational work.

Another example of an open-end winding engine applied to an electric vehicle is the one presented in the paper [22]. Examines the case of an electric vehicle driven by a dual-inverter system with a five-phase open-end winding motor.

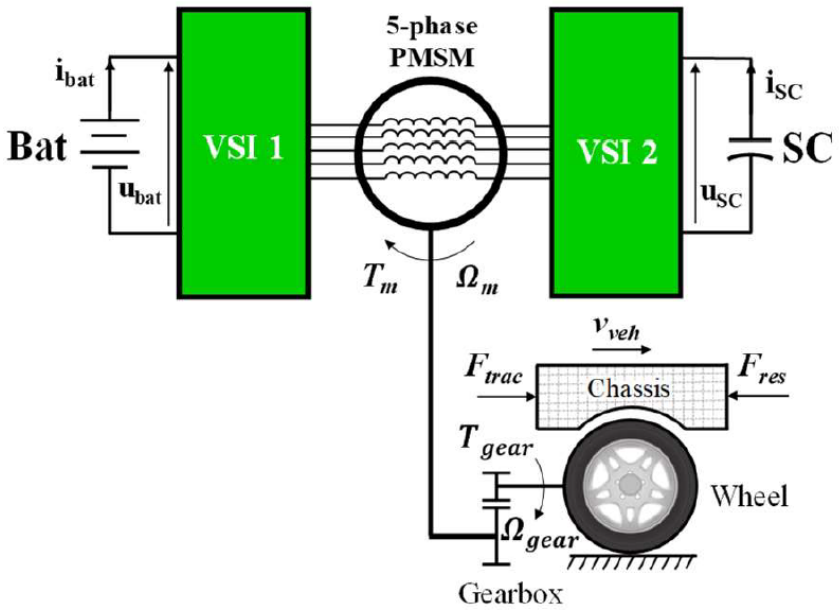

Figure 2.30: EV system with 5-phase OW-PMSM fed by HESS [22].

The two five-level VSI inverters are fed by a hybrid energy storage system (HESS), that is composed of a Li-ion battery and supercapacitors (SC). Instead, as visible in Figure 2.30, the vehicle is schematised by the wheel and chassis, connected to the machine via a gearbox, which is used to reduce the speed of the machine and to increase its torque. The entire system is analysed using the energetic macroscopic representation (EMR) formulation, which describes the energetic system through the interaction of the various subsystems into which it is divided (Figure 2.31), for control purposes.

Furthermore, the five-phase motor is equivalent to three fictitious machines in a rotating

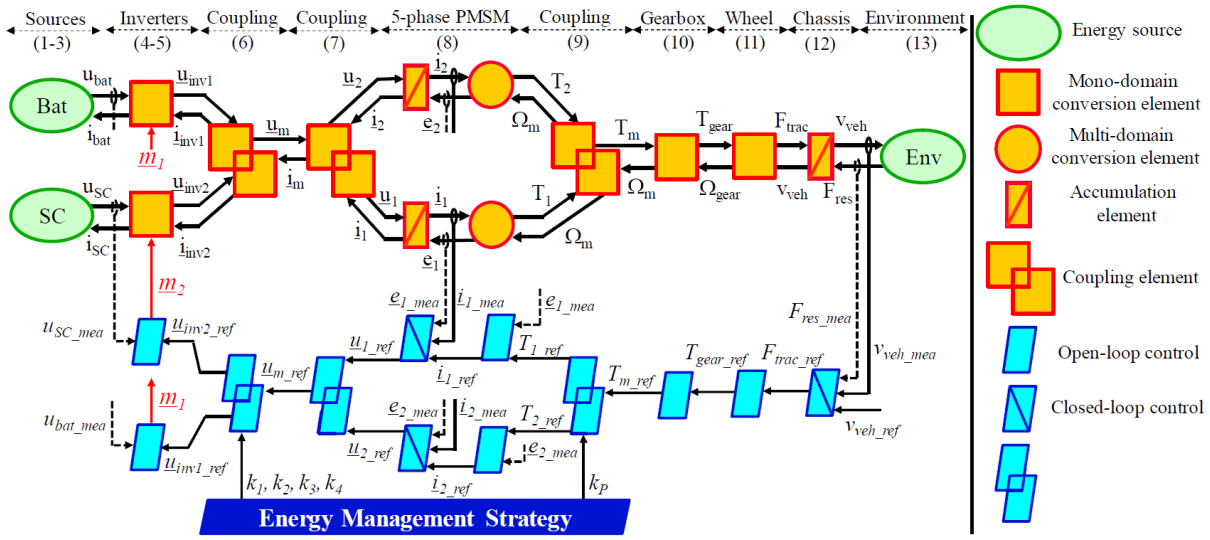

Figure 2.31: EMR diagram and IBC control [22].

reference system, only two of which are responsible for torque generation. Using the EMR, the motor is schematised by the assembly of a storage element and a multi-domain conversion element. They respectively represent the machine windings and the electro-mechanical conversion of variables (from currents and back EMFs to torque and rotational speed). An inversion-based control (IBC) is also implemented, which is divided into global and local levels for the control of the electric vehicle. The local levels contain closed-loop controls to track the desired speed profile. The global levels, on the other hand, are used to distribute and manage the system's energy flow. Indeed, in the Figure 2.31, it can be seen that an energy management system (EMS) has been implemented for this purpose to regulate the energy flows between the two sources and the fictious machines in order to meet the required power P_{ref} of the EV in accordance with the speed profile. This strategy uses the power factor k_p to control the powers between the two machines, described in Equation (2.14)

$$k_p = \frac{P_1}{P_1 + P_2} = \frac{P_1}{P_{ref}}. \tag{2.14}$$

After having defined the powers of the system, the reference voltages for the two inverters can be calculated. Inverter2 will have a power factor equal to 1 in all charge and discharge operations of the supercapacitor, so the unity power factor method will be used. Then, using the output voltages from the inverters, the voltages at the ends of the two fictitious machines can be defined.

To verify the efficiency of the proposed solutions, through appropriate simulations, the system presented was compared with a wye-connected machine fed by a single invert,

without the SCs. As expected, the proposed solution allows a lower peak value of battery current than the conventional system. This results in less wear and a longer battery life. With the presence of the SC, it is also possible to reduce the battery size, since the power required by the system is reduced and matches the power of the battery. The latter is also able to recover all regenerative energy, recharging up to its nominal voltage value. Finally, the adopted EMS is able to control four energy flows, two for each fictitious machine, in the drive system allowing more efficient power management than conventional systems.

In the next paper, an interesting solution is proposed for increasing the supply voltage of an open-end winding motor using two different batteries with only one charging socket [23]. This configuration was chosen because it provides the advantages of a dual-inverter configuration, while avoiding the generation of the triple harmonic current. This harmonic is generated with a common dc-link configuration, and it increases core saturation and copper losses. Only one charger will be used for the first voltage source, while the second will be recharged through Inverter1.
Therefore, Battery1 will be used as the main source and Battery2 will operate as an auxiliary source, with intermittent utilisation. This system reduces the high cost and weight of the system, which would have been with two chargers.

Three different control schemes are established in the paper, depending on the motor speed: standstill, below base speed and in the flux-weakening region (above base speed). The model of the machine was developed in the synchronous reference frame and the d-axis and q-axis equivalent circuits of the motor are shown in Figure 2.32.

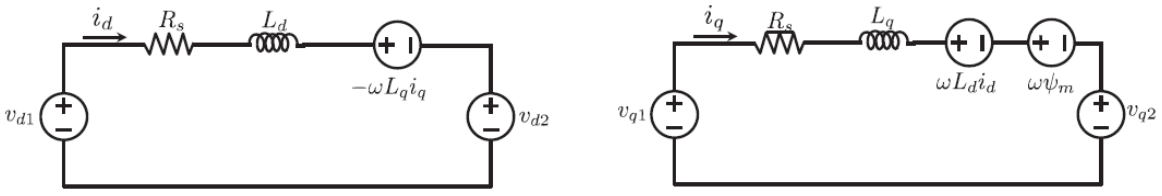

(a) d-axis. (b) q-axis.

Figure 2.32: Equivalent circuits in the synchronous reference frame [23].

Instead, the power delivered by the motor (2.15) consists of the sum of the power absorbed by the two inverters in the system:

$$P_{mot} = P_{inv1} + P_{inv2} = \frac{3}{2}[(v_{d1} - v_{d2})i_d + (v_{q1} - v_{q2})i_q] = \frac{3}{2}(v_{dm}i_d + v_{qm}i_d). \qquad (2.15)$$

As mentioned above, charging methods have been established for three different cases,

with respective control schemes and algorithms:

- At standstill ($\omega_e = 0$), the q-axis current is held at zero while the d-axis current is used for charging without the risk of core demagnetisation. From the power relationship between inverter2 and the battery, the current $i_d = \frac{2}{\sqrt{3}} I_{bat2}$ is derived, by considering the inverter's maximum current equal to $\frac{1}{\sqrt{3}} v_{bat2}$. In this particular case, therefore, battery2 is subject to a fast charge, through a current $i_d^* = \frac{2}{\sqrt{3}} I_{bat2}^c$, which corresponds to the current limit for the battery. The voltage of inverter2 will instead be $v_d = \frac{V_{bat2}}{\sqrt{3}}$ and $v_q = 0$. The control used is shown in Figure 2.33;

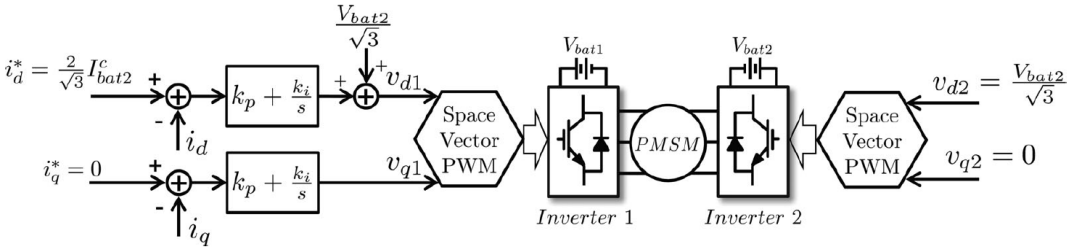

Figure 2.33: Block diagram scheme in the standstill charging situation [23].

- Below base speed, the main task of the control (in Figure 2.34) is to supply to the motor the desired torque setting the stator current components. Then, if there is a residual voltage, it will charge the battery2. In this way, the stator voltage is also established while the voltages of the two inverters are decided in order to maximise the charging power. This is achieved when the current and voltage vectors of Inverter1 are in parallel, therefore, when the PF of the inverter is unity, always remaining within the limits of the maximum available inverter voltages;

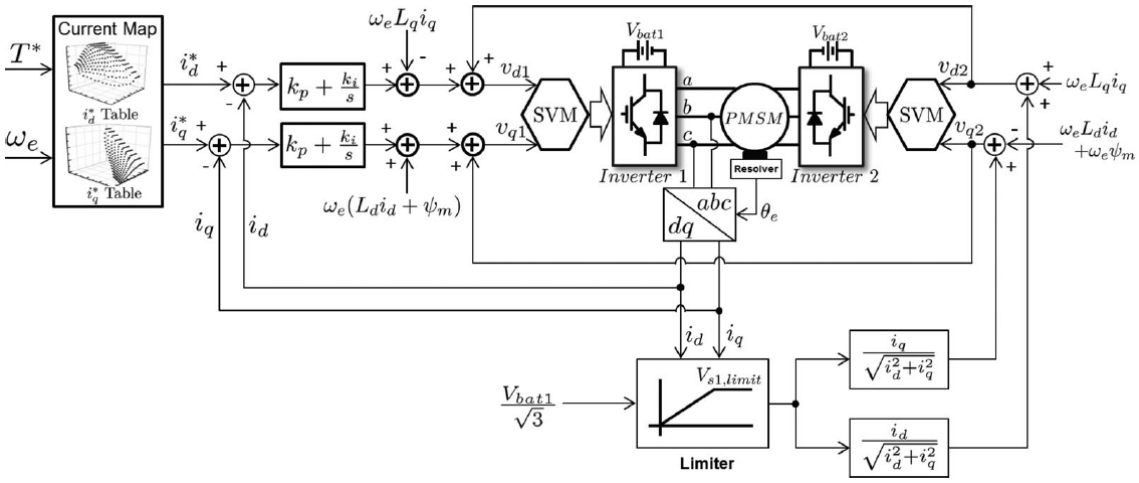

Figure 2.34: Block diagram scheme in the low-speed area [23].

- For values of ω_e above the base speed, the currents at the operating point B are found on the constant torque curve (i_{dB}, i_{qB}) of tangential intersection with that of the voltage limit, considering a margin for it. This point varies, of course, depending on the state of the motor. From the components of the current, the vector of the motor voltage is obtained in the Equation(2.16), which is used to calculate the voltage of the inverter2 that will recharge the battery2.

$$v_{s2} = v_{s1} - v_{sm} = \Big(\frac{V_{bat1}}{\sqrt{3}}\frac{i_{dB}}{I_{sB}} + \omega_e L_q i_{qB}, \frac{V_{bat1}}{\sqrt{3}}\frac{i_{qB}}{I_{sB}} - \omega_e L_d i_{dB} - \omega_e \psi_m\Big). \tag{2.16}$$

Where $I_{sB} = \sqrt{i_{dB}^2 + i_{qB}^2}$, and the voltage of inverter1 is obtained from the unity power factor:

$$v_{s1} = \frac{V_{bat1}}{\sqrt{3} I_{sB}}(i_{dB}, i_{qB}). \tag{2.17}$$

If the operating point is in a zone of really high speed, the Battery2 cannot be recharged.

2.2.4. Other types of applications

Paper [24] analyses the use of an open-end winding permanent magnet synchronous generator in a wind energy conversion system (WECS). The proposed system, in Figure 2.35 consists of the open-end wind generator connected on both three-phase ends to a full-bridge diode rectifier, to provide a unidirectional power flow from the OW-PMSG to the power grid. A boost converter is also used, to increase the voltage before it is sent to the dc-link, and a medium-voltage NPC inverter to connect the system to the grid.

The main problem in this configuration in Fig. 13 is the torque ripple, and to solve it, it is necessary the introduction of a zero-sequence back-emf observer (ZCBO), to have a continuous estimate of the zero-sequence back-emf and zero-sequence current (ZSC). Indeed, with the quantities estimated by the ZCBO, the two sensor less adaptive control methods proposed in the paper can be implemented.

The first is a sliding mode control (SMC) with predictive current control. Here, a sliding mode speed controller is used in the speed loop, and a deadbeat-based predictive current controller is utilized for current regulation. A reliable adaptive sliding mode function is required to convert the estimated parameters into an adaptive slide mode surface. The

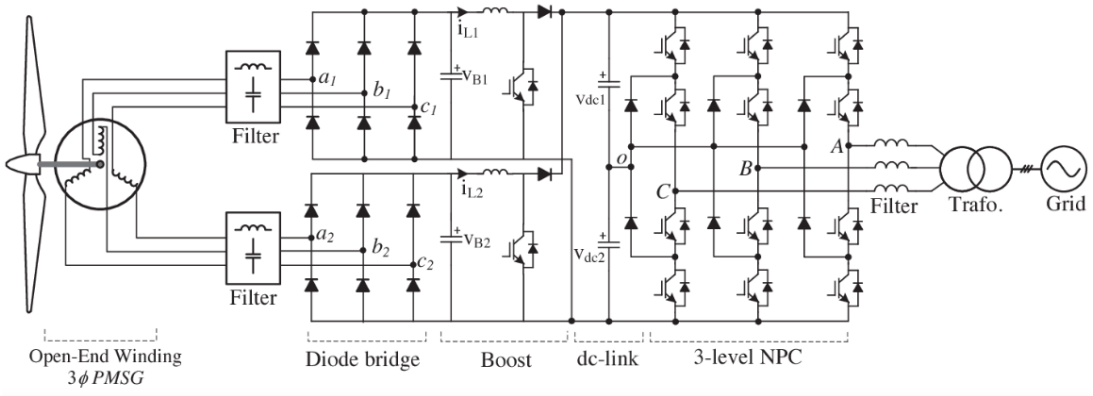

Figure 2.35: Wind power generation system with open-end winding PMSG [24].

second proposed method is a model reference adaptive control (MRAC) with deadbeat predictive control. In this type of control, an MPC (model predictive control) is used instead of a fixed-gain PI controller to estimate rotor position and speed. The MPC used is a deadbeat predictive control with feed forward linearisation since it has an excellent transient response and a constant switching frequency.

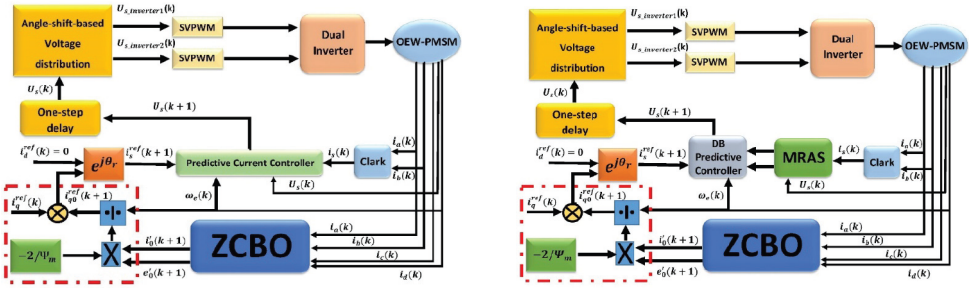

(a) Predictive current control. (b) MRAS.

Figure 2.36: Predictive current control with ZCBO and MRAS [24].

From the simulations carried out to compare the two different methods, it can be seen that the second proposed strategy is able to generate greater stability and efficiency. The first method also requires a higher wind speed to produce the same active power.

A different application of the OW motor is analysed in [25], where this type of motor is used in a grid-connected distributed system.
In the proposed configuration, shown in Figure 2.37, only one inverter is used, connected to the three terminals of the open-end winding surface mounted PM motor, which will be used as a generator, while the other three terminals are connected to the power grid. A engine is also implemented to generate the power P_{eng}.

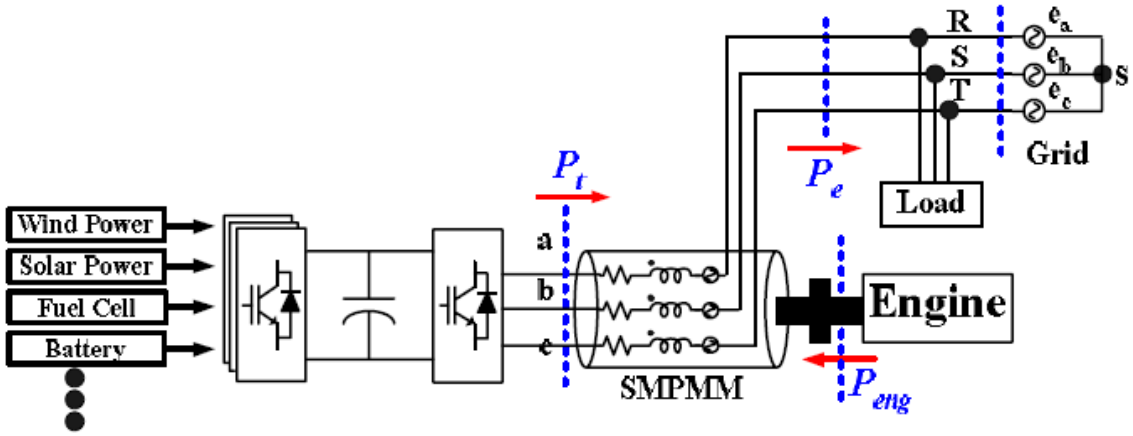

Figure 2.37: Scheme of the overall system, with the engine, the SMPMM and the grid [25].

The proposed configuration avoids the use of the two converters found in conventional engine generation solutions, which increase the overall cost and reduce the efficiency of the system. Furthermore, the system described in the paper allows the power flows of both sides to be managed independently.
To do this, the following voltage Equations(2.18) in the dq reference frame were obtained:

$$\begin{bmatrix} V_{ds}^r \\ V_{qs}^r \end{bmatrix} = \begin{bmatrix} r_s + \rho L_s & -\omega_s + \rho L_s \\ \omega_s + \rho L_s & r_s + \rho L_s \end{bmatrix} \begin{bmatrix} i_{ds}^r \\ i_{qs}^r \end{bmatrix} + \begin{bmatrix} 0 \\ \omega_r + \phi_f \end{bmatrix} + E \begin{bmatrix} -\sin(\theta_e - \theta_r) \\ \cos(\theta_e - \theta_r) \end{bmatrix}. \quad (2.18)$$

Where, θ_e and E are respectively the synchronisation angle and the peak value of the grid voltage, while θ_r represents the rotor angle.
The speed of the OW motor is synchronised with the frequency of the grid, and the difference between the grid and rotor angle is kept constant.
In the operating region where the motor speed starts from zero until the synchronising speed, there is an increase in the dc-link voltage to a value given by the sum of the grid voltage and the generator back efm. To ensure that, it does not exceed this value, the d-axis current is used to limit the dc-link voltage.
When the synchronising speed is reached, the voltage, power and torque equations become independent of time, as the angle difference is kept constant. The q-axis current is used to control the slip angle θ_{sl} through the rotor angle, while the d-axis current is used to regulate the dc link voltage and thus the power in the system P_t. The control schemes for the two different conditions are depicted in Figure 2.38.

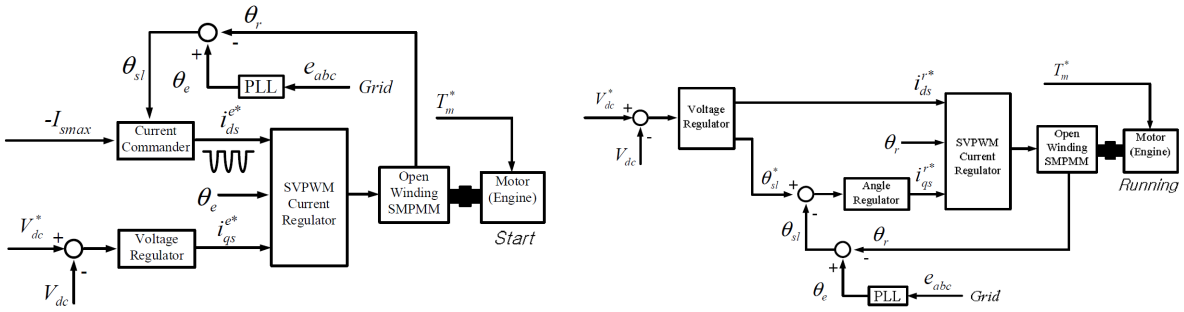

(a) Before synchronization. (b) After synchronization.

Figure 2.38: Block diagram scheme of the proposed system [25].

In order to demonstrate the validity of the proposed system and the control used, simulations were carried out in which an IPM is used as a generator, directly coupled to the open-end winding motor, with torque control.

The experimental results show that controlling the d-axis and q-axis currents provides effective control of power flows in both directions between engine, grid, and dc-link. Finally, compared to conventional systems, as initially emphasised, greater efficiency and lower costs are achieved, and optimal management of the power generated by the different energy sources is achieved.

3 | Open-end winding motor

3.1. Different Types

As already mentioned in the *Introduction part*, open-end windings are a particular type of motor obtained by opening the three-phase stator ends, which are usually connected in a triangle or star configuration in conventional motors, thus obtaining a total of six terminals.

Therefore, a motor with an open winding can be driven with a double inverter configuration. As the name suggests, it allows to implement two inverters, which can be connected to one or two different DC sources in the system, such as an energy conversion device and an energy storage system, i.e. a battery and a floating capacitor. In [3], the main typologies of dual-inverter configurations are presented:

- Dual inverter with common DC link (Fig. 3.1a): here there is only one DC voltage source, which can be either a battery or a boosted voltage through a DC/DC converter. The achievable line voltage is equal to the value of the V_{dc} source, which is higher than the single inverter configuration;
- Dual inverter with isolated DC link (Fig. 3.1b): with this type of configuration there is not a common mode current path, and the common-mode voltage can be used to improve the differential voltage at the ends of the motor. In this case, a maximum phase voltage can be obtained of $(V_{dc1} + V_{dc2})/\sqrt{3}$;
- Dual inverter with common mode connected DC links (Fig. 3.1c): with this configuration for supplying the open-end winding motor, the common mode current can flow through the path consisting of the connection of the OO' points. When this current is kept zero, the maximum available voltage is $(V_{dc1} + V_{dc2})/2$.

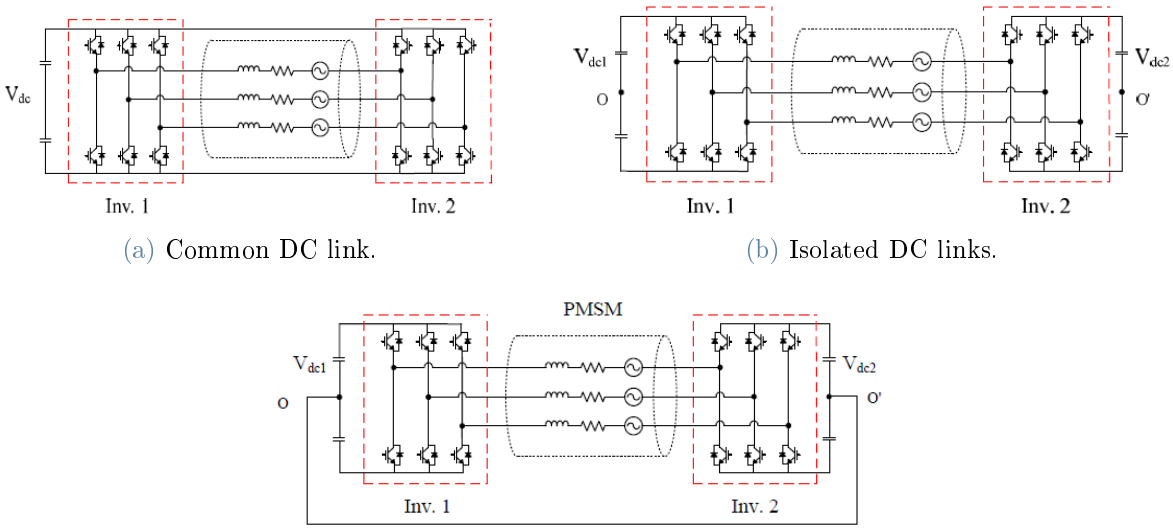

(a) Common DC link.

(b) Isolated DC links.

(c) Common mode connected DC links.

Figure 3.1: Analysed dual-inverter configurations [3].

The main differences between the configurations presented are that, with the two isolated DC sources there is no zero-sequence current, which reduces total Joule losses and current ripple. Moreover, with two independent sources, the power exchange between the two inverters can be managed, optimizing the power flow. But, on the other hand, the solution with a common DC-link reduces the overall cost, complexity and volume of the system.

3.2. Benefit and Drawbacks

Open-end winding permanent-magnet motors, in addition to retaining high power density and high efficiency of PM machines, also avoid the use of DC/DC converters, which are required in conventional systems to keep the DC-link voltage constant and which greatly increase the complexity, cost and total power consumption of the system.
Compared to conventional Y-connected motors, they have a larger speed range and greater power density because they can achieve a higher phase voltage with the same DC bus voltage. But to reach high performance, it is necessary to design a suitable control in flux-weakening region. These motors have greater flexibility and accuracy in the control and, as the currents of each phase can be controlled separately, they also have a strong fault tolerance. Due to this good controllability, output power can be increased with respect to star-connected motors.

Furthermore, as two inverters are used, the problem of switching losses increases, as they will be higher than when only one inverter is used in the control of a conventional systems. However, by using the dual-inverter configuration, two different types of electrical sources can be implemented, such as a battery and a supercapacitor, or an energy storage system and an energy conversion device, and it is possible to control the energy distribution between these two sources without involving a DC/DC converter. In electric vehicles, their combined operation allows the useful life of the components can be extended, for example by using the battery for constant speed operations, and the supercapacitor during acceleration and deceleration. Through the use of an open-end winding motor, it is also possible to obtain a multilevel output voltage that improves total harmonic distortion (THD).

On the other hand, it is more complicated to implement system control than the single inverter configuration since power management between the two sources must also be introduced since, for an automotive applications, and it is also necessary to balance the state of charge and the efficiency of the two batteries to maximise the range of the vehicle.

The main disadvantages of open-end winding motors are the higher probability of a single point of failure, the complexity of overall control, greater costs associated with the presence of more components to realise the system, and most of all, the increase in the inverter losses due to the higher switching frequency.

3.3. Modelling

The modelling of open-end winding motors is carried out in the same way as that of three-phase y-connected motors. Therefore, the three-phase equivalent model of the motor will be the series circuit consisting of a resistor, an inductor and the back-emf, as in Figure 3.2 (series modelling).

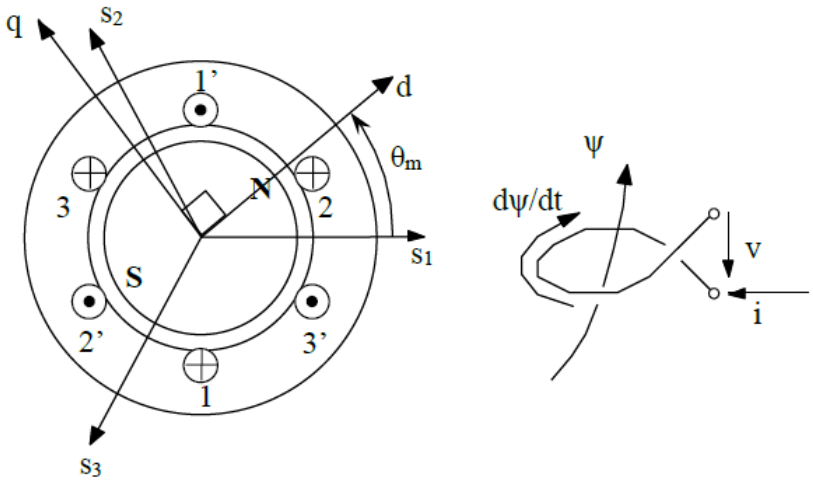

Figure 3.2: Schematic diagram of the AC motor with permanent magnet.

Indeed, there is only one difference with respect to the latter case: the voltage applied to the ends of the machine. For open-end winding motors, this voltage is given by the difference of the vector voltages generated separately by the two inverters, as the open stator windings are connected to the legs of the two inverters. Therefore, as a base case, the system configuration shown in Figure 3.3.

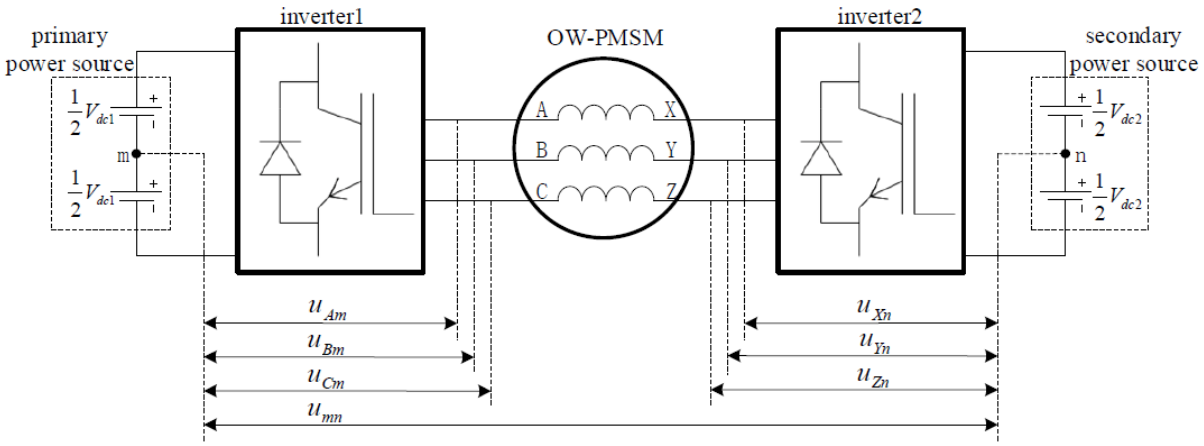

Figure 3.3: System diagram with mid-point voltage [15].

By dividing the dc sources into two equal parts based on their total voltage, a midpoint is defined for each inverter (represented in Fig. 3.3 by points m and n). In this way, the voltages between each inverter output leg and the midpoint, called inverter phase voltages, are used. The space vectors generated by the two inverters, described by the Equation (3.1), can be obtained:

$$\begin{cases} \vec{u}_{s1} = \sqrt{\frac{2}{3}}(u_{Am}e^{j0} + u_{Bm}e^{j\frac{2\pi}{3}} + u_{Cm}e^{j\frac{4\pi}{3}}), \\ \vec{u}_{s2} = \sqrt{\frac{2}{3}}(u_{Xn}e^{j0} + u_{Yn}e^{j\frac{2\pi}{3}} + u_{Zn}e^{j\frac{4\pi}{3}}). \end{cases} \tag{3.1}$$

With these two voltage vectors, it is possible to calculate $\vec{u}_s$ and, taking into account that the two voltage sources dc are electrically isolated, the voltage connecting the two midpoints ($\sqrt{\frac{2}{3}}u_{mn}(e^{j0} + e^{j\frac{2\pi}{3}} + e^{j\frac{4\pi}{3}} = 0)$ can be eliminated (3.2):

$$\vec{u}_s = \vec{u}_{s1} - \vec{u}_{s2} = \sqrt{\frac{2}{3}}(u_{AX}e^{j0} + u_{BY}e^{j\frac{2\pi}{3}} + u_{CZ}e^{j\frac{4\pi}{3}}). \tag{3.2}$$

For the machine model, that of a classical brushless AC motor is implemented (as mentioned above). More precisely, considering a concatenated flux of the permanent magnets of the sinusoidal form of the type $\psi_{pm}(\theta_m) = \hat{\psi}_{pm}cos(\theta_m)$. Considering a stationary reference system, where the α-axis coincides with the magnetic axis of the first motor winding, and applying the formula for spatial phasors, (3.3) and (3.4) are derived.

$$\bar{v}_s^{\alpha\beta} = R_s\bar{i}_s^{\alpha\beta} + p\bar{\psi}_s^{\alpha\beta}, \tag{3.3}$$

$$\bar{\psi}_s^{\alpha\beta} = L_s\bar{i}_s^{\alpha\beta} + \psi_{pm}e^{j\theta_m}, \tag{3.4}$$

$$\psi_{pm} = \sqrt{\frac{3}{2}}\hat{\psi}_{pm}. \tag{3.5}$$

In which v_s, i_s, R_s, L_s and ψ_s are the voltage, current, resistance, inductance and flux of the stator, respectively, while ψ_{pm} represents the flux of the permanent magnets and the symbol p denotes the derivative $\frac{d}{dt}$.

Then, by changing to a rotational reference system in which the north pole of the permanent magnets is fixed to the d-axis, the electrical equations (3.6), (3.7), (3.8), (3.9) for the motor model under consideration are obtained.

$$v_{sd} = R_s i_{sd} + L_d p i_{sd} - \dot{\theta}_m L_q i_{sq}, \tag{3.6}$$

$$v_{sq} = R_s i_{sq} + L_q p i_{sq} - \dot{\theta}_m L_d i_{sd} + \dot{\theta}_m \psi_{pm}, \tag{3.7}$$

$$\psi_{sd} = L_d i_{sd} + \psi_{pm}, \tag{3.8}$$

$$\psi_{sq} = L_d i_{sq}. \tag{3.9}$$

Where the symbol $\dot{\theta}_m$ represents the derivative of the mechanical angle between the d-axis of the reference system and the magnetic axis s_1, which therefore corresponds to the mechanical speed through the number of pole pairs: $\dot{\theta}_m = n_p \Omega_m$.
The mechanical equations of the machine are instead described by the formulas (3.10) and (3.11).

$$\frac{d}{dt}\dot{\theta}_m = \frac{n_p}{J}(T_e - T_r), \tag{3.10}$$

$$T_e = n_p \bar{i}_s \underline{\psi}_s = n_p[(L_d - L_q) i_{sd} i_{sq} + \psi_{pm} i_{sq}]. \tag{3.11}$$

Where T_r is the load's resistant torque and T_e is the electromagnetic torque generated by the machine.

4 | System configuration

The main purpose is to use a control and a system configuration that can take advantage of the use of an open-end winding PMSM, compared to a conventional three-phase permanent magnet motor. To do this, it is necessary to minimise the disadvantages of this type of motor, such as reducing switching losses, which are already a major problem in electric propulsion systems. Indeed, due to the presence of a second inverter, there will be a further increase of these losses, which must therefore be reduced as much as possible.

As seen in the *State of the Art*, in [21] this particular problem has been dealt with in that the switching states of the first inverter are controlled via a lookup table based scheme, decreasing the switching frequency and thus also the corresponding losses. This configuration will also be compared, in order to verify its improvement, with a more traditional system used to control an open-winding motor, the 180° decoupled modulation. Furthermore, this control strategy has been implemented in the system to maximise the output electrical power of the open-winding motor, while reducing current harmonics and thus losses. The system in Figure 4.1 will be employed. Two isolated DC voltage sources are used in order to avoid zero-sequence current flow. This also results in lower current harmonics and fewer losses due to the Joule effect, than in the case with common DC-link.

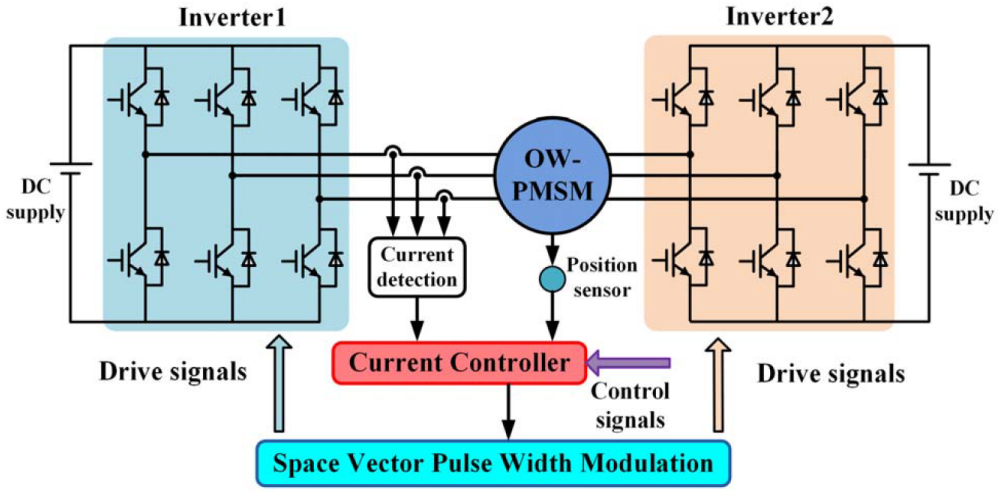

Figure 4.1: Diagram of the motor drive configuration applied.

The analysed solution uses two-level voltage source inverters (VSI) to control the open-end winding motor, in the dual-inverter configuration.
More precisely, each inverter can achieve eight different switching states, which can be divided into six different sectors on the $\alpha\beta$ reference frame, as in Figure 4.2. They correspond to the division into the six sectors listed in Table 4.1.

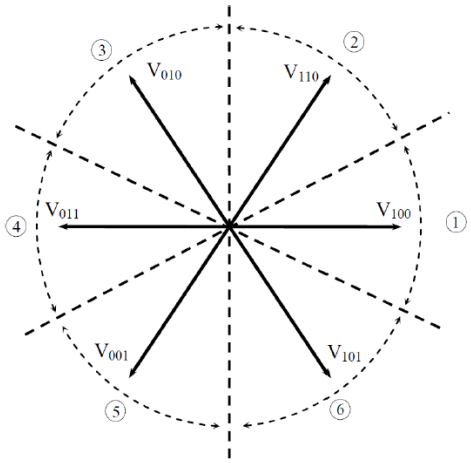

Figure 4.2: Voltage space vectors for the two-level VSI.

Each switching state of the individual inverter represents a voltage space vector. Six that represent active voltage configurations and the others represent the two zero voltage configurations. Therefore, there will be a total of sixty-four different combinations of voltage space vectors for the dual-inverter configuration.

Instead, the two different control configurations proposed of the two inverters are shown in Figure 4.3.

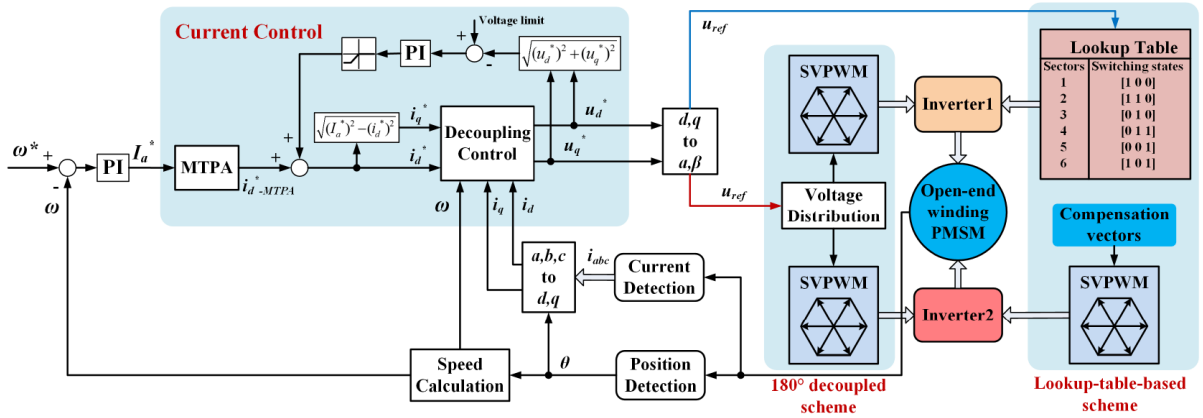

Figure 4.3: Overall control scheme diagram of the implemented solution.

In the region below base speed ω_b, the control system analysed employs the MTPA (maximum torque per ampere) method. It establishes the minimum values of the dq components of the armature current that can generate the required torque.
However, this solution is no longer suitable for higher speed values than ω_b, as the back-EMF is not compensable by the dc sources any more. In this case, a flux-weakening control based on two closed loops, one for speed and the other for current, is applied. The reference voltage (u_{ref}) generated by the system represents the input of the lookup-table which simultaneously combines six-step modulation with PWM, as shown in Table 4.1.

Sector	Reference Voltage's Angle	Switching States
I	-30°$\leq \theta <$30°	[1 0 0]
II	30°$\leq \theta <$90°	[1 1 0]
III	90°$\leq \theta <$150°	[0 1 0]
IV	150°$\leq \theta <$180° -180°$\leq \theta <$-150°	[0 1 1]
V	-150°$\leq \theta <$-90°	[0 0 1]
VI	-90°$\leq \theta <$-30°	[1 0 1]

Table 4.1: Inverter1 switch status according to reference voltage angle.

It is divided into six sectors in the $\alpha\beta$ reference plane and, according to the value of the voltage vector angle $\theta_{u_{ref}}$, it handles the states of the first inverter's switches.
Depending on the sector in which the vector $\bar{u}_{ref}$ is located, the reference for the Space Vector PWM are set via Table 4.2. In this way, the $\alpha\beta$ components of the reference voltage vector for the modulation of the compensation inverter are obtained, which will have the task to balance the power flow in the system.

Sector	Compensation Vectors
I	$u^*_{\alpha 2} = u^*_\alpha - \frac{2}{3}V_{dc1}$; $u^*_{\beta 2} = u^*_\beta$
II	$u^*_{\alpha 2} = u^*_\alpha - \frac{1}{3}V_{dc1}$; $u^*_{\beta 2} = u^*_\beta - \frac{\sqrt{3}}{3}V_{dc1}$
III	$u^*_{\alpha 2} = u^*_\alpha + \frac{1}{3}V_{dc1}$; $u^*_{\beta 2} = u^*_\beta - \frac{\sqrt{3}}{3}V_{dc1}$
IV	$u^*_{\alpha 2} = u^*_\alpha + \frac{2}{3}V_{dc1}$; $u^*_{\beta 2} = u^*_\beta$
V	$u^*_{\alpha 2} = u^*_\alpha + \frac{1}{3}V_{dc1}$; $u^*_{\beta 2} = u^*_\beta + \frac{\sqrt{3}}{3}V_{dc1}$
VI	$u^*_{\alpha 2} = u^*_\alpha - \frac{1}{3}V_{dc1}$; $u^*_{\beta 2} = u^*_\beta + \frac{\sqrt{3}}{3}V_{dc1}$

Table 4.2: Components of the compensation voltage vector of inverter2.

Where u^*_α, u^*_β are the components of the total reference voltage of the control system, while $u^*_{\alpha 2}$, $u^*_{\beta 2}$ are those of the reference voltage vector of inverter2.

An example of the voltage space vectors obtained from the modulation of the two analysed VSIs is represented in Figure 4.4.
The open-end winding motor stator voltage space vector u_s is generated by the difference between u_{s1}, obtained from the lookup table, and the compensation voltage u_{s2}, as seen in equation (3.2).

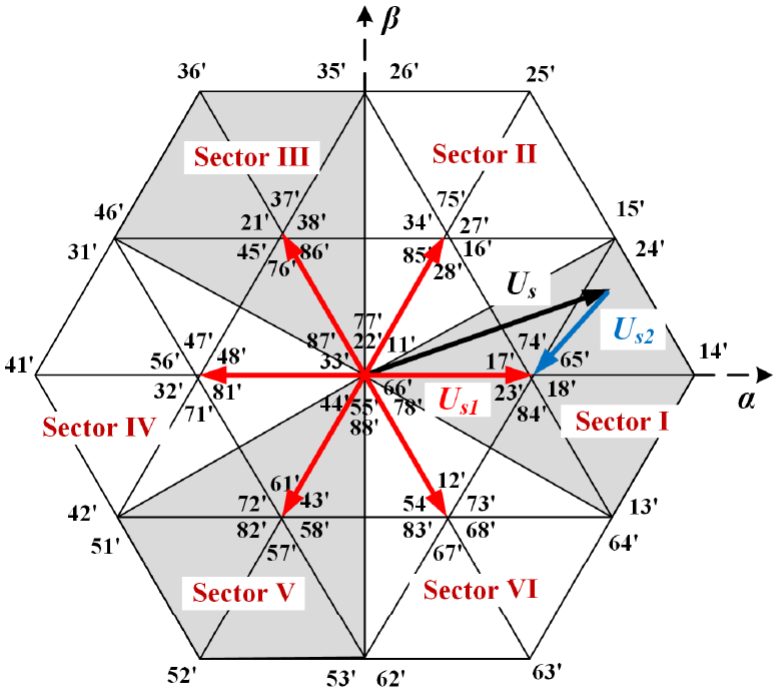

Figure 4.4: Space vector modulation diagram of the lookup based method [21].

As mentioned above, this method will be the main solution for open-end winding motor control. Furthermore, it will be compared with the conventional 180° decoupled Space Vector PWM scheme.
The operating principle of this modulation technique is to separate the voltage reference space vector into two equal and opposite vectors. Thus, from the vector $\bar{u}_{s\,ref}$, the two vectors are derived through equation (4.1), which are shown in Figure 4.5:

$$\begin{aligned} \bar{u}_{s1} &= \left|\frac{\bar{u}_{s\,ref}}{2}\right| \angle\alpha, \\ \bar{u}_{s2} &= \left|\frac{\bar{u}_{s\,ref}}{2}\right| \angle\alpha + 180. \end{aligned} \tag{4.1}$$

They will respectively represent the SVPWM inputs of the dual-inverters configuration, to obtain the switching states and times of the two independent inverters.

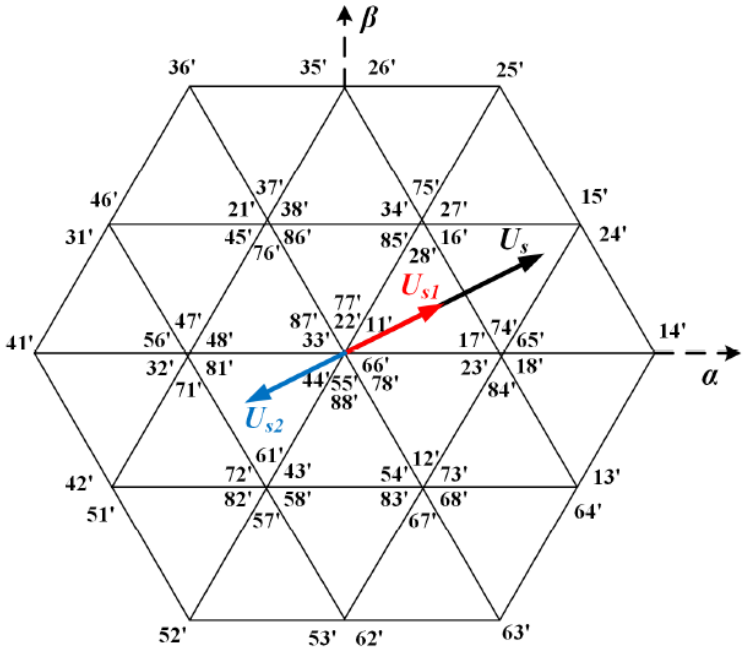

Figure 4.5: Space vector modulation diagram of the decoupled 180° method [21].

5 | System model implementation

To check the effectiveness of the analysed solutions for the open-end winding motor control, simulations were carried out through the implementation of the system on Simulink and MatLab, as shown in Figure 5.2. In contrast to the above, an MTPA technique was not used, but the control is carried out through the motor's operational regions.

As can be seen from the equation (3.11) of the electromagnetic torque, it is most dependent on the quadrature component of the stator current i_s. Furthermore, in the case examined, we have an isotropic synchronous machine, in which $L_d = L_q = L_s$ and thus the "reluctance torque" is zero. Therefore, in order to optimise the electromagnetic torque T_e, it is necessary to maximise the current i_{sq} and set i_{sd} equal to zero, minimising the amplitude of the stator current phasor as well as reducing losses.
This will result in a constant i_{sq} component equal to the maximum stator current, limited only by the thermal constraints of the machine. Then, the motor will be able to generate the maximum possible electromagnetic torque, which will also be constant.
This situation ($i_{sd} = 0, i_{sq} = i_{s\,max}$) can be maintained for all speed values below the base speed. When $\omega = \omega_b$, the stator voltage of the motor have reached the maximum value imposed by the voltage limit, that can be supplied by the power converter. In this situation, as represented by the vector diagram in Figure 5.1a, the synchronous machine will no longer be able to increase its speed.

In order to reach speeds higher than ω_b, it is necessary to introduce a negative current i_{sd} (no longer equal to zero), which will generate an inductive voltage drop that will partially counteract the emf E, which rises with the increasing of the mechanical speed ($E = \omega_m \psi_{pm}$). In this case, i_{sq} will no longer be equal to the maximum permissible stator current, but will respect the equation (5.1). Otherwise, the stator voltage will be greater than the maximum allowable value of the converter.

$$i_{sq} = \sqrt{i_{s\,max}^2 - i_{sd}^2} < i_{s\,max}. \tag{5.1}$$

In this zone, called flux-weakening region, the stator voltage is always equal to the max-

imum value, while the power output becomes constant. This situation is represented on the vector diagram in Figure 5.1b.The limiting case occurs when the conditions in (5.2) are achieved, the critical speed value ω^* being reached.

$$\begin{aligned} \delta &= \frac{\pi}{2}, \\ i_{sd} &= \frac{\psi_{pm}}{L_s}, \\ i_{sq} &= \frac{v_{max}}{\omega_m L_s}. \end{aligned} \tag{5.2}$$

When $\omega \geq \omega^*$, as in the vector diagram in Figure 5.1c, the electromagnetic torque starts to decrease as $\frac{1}{\Omega_m}$ and also the stator current will start to drop below its maximum level. Accordingly, this control will be integrated to manage the reference current i_{sdref} based on the speed values and therefore according to the operating region.

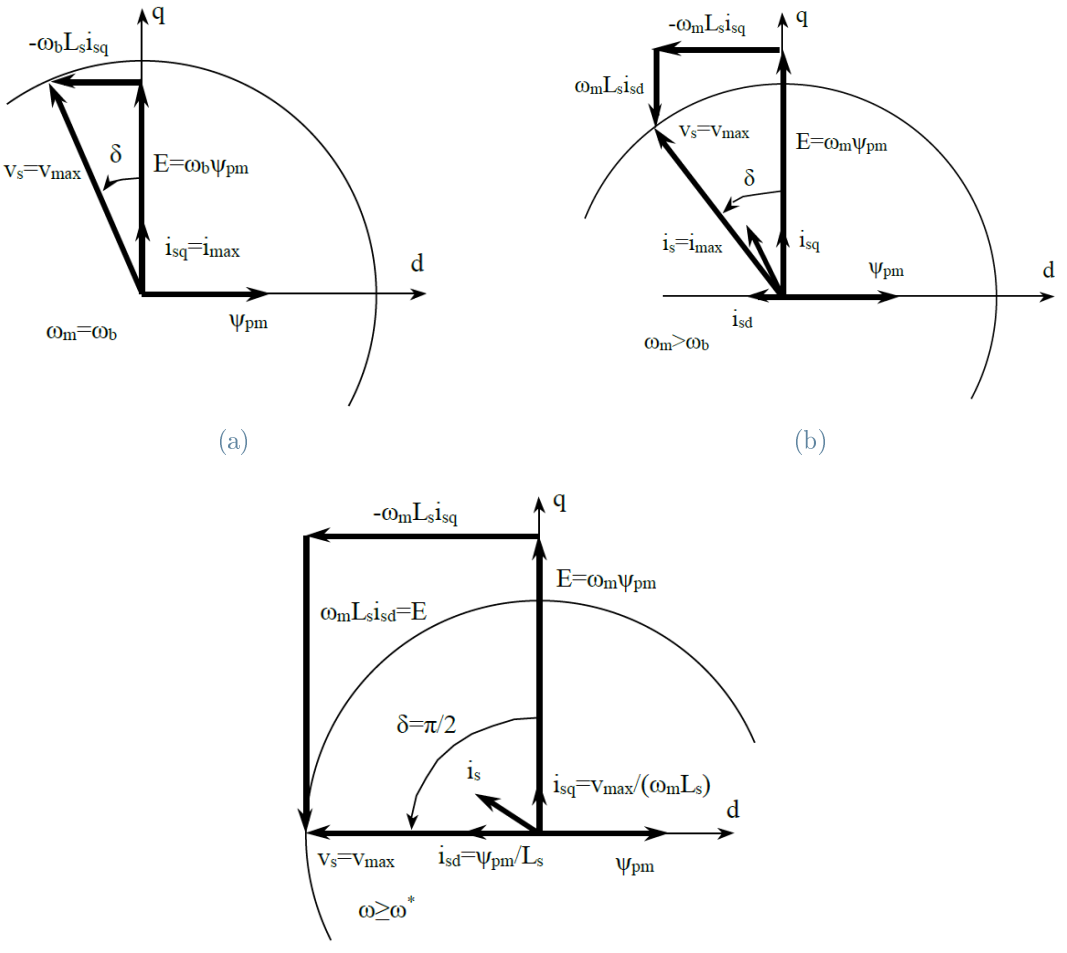

Figure 5.1: Vector diagrams according to speed values.

The two control solutions adopted for the open-end winding motor will be compared with a conventional three-phase permanent magnet synchronous machine. Telemetry data, recorded for an electric car on the Varano track, will be used as speed and electromagnetic torque references, to analyse the behaviour of the two different motor types under the same conditions.

5.1. Motor and system parameters

The main parameters of the open-end winding motor used in the simulations are those shown in Table 5.1. As mentioned above in this case, the d and q components of the stator inductance will have the same value, represented by the inductance L_s.

Parameter Name	Value
Stator resistance R_s	0.1 Ω
Stator inductance L_s	0.8 mH
Permanent magnet flux ψ_{pm}	0.5 Wb
Efficiency η	0.95
Power factor $\cos\phi$	1
Pole pairs n_p	2
Rated power P_m	180 kW
Rated speed ω_n	400 rad/s
Maximum speed v_{max}	240 km/h
Maximum acceleration a_{max}	4 m/s^2

Table 5.1: Motor parameters.

Whereas, the other system parameters, such as the voltages of both DC sources in the lookup table configuration and the one for classic PM AC motor, are listed in Table 5.2. A data on which the control of the open-end winding motor is based is the maximum value of the stator current i_s, as mentioned in the chapter 5. To do this, it is first necessary to calculate the equivalent inertia at the motor shaft using the formula expressed in the equation (5.3).

$$J_{eq} = m_{tot}\frac{G_r^* d_r^*}{4}. \tag{5.3}$$

Parameter Name	Value
DC-link voltages VSI1 $V_{dc\,1}$	200 V
DC-link voltages VSI2 $V_{dc\,2}$	200 V
DC-link voltage conventional system	400 V
Switching frequency f_{sw}	5 kHz
Sample time T_s	5 μs
Friction coefficient β	0.065 Nm
Load (resistant) torque T_r	$T_r = 4\beta\Omega$
Gear ratio G_r	1/3
Total weight m_{tot}	1580 kg
Tyre radius d_r	30 cm

Table 5.2: System parameters.

While in the equation (5.4), the maximum electromagnetic torque that can be delivered by the motor can be obtained.

$$T_{e\,max} = \frac{a_{max}}{G_r^* \frac{d_r^*}{2}}. \tag{5.4}$$

In this way, it is possible to derive the maximum value of the stator current in (5.5). It will also correspond to that of the current $i_{sq\,max}$.

$$i_{s\,max} = \frac{T_{e\,max}}{n_p \psi_{pm}}. \tag{5.5}$$

Regarding the maximum allowable voltage, it is obtained from the inverter's DC bus voltage in the equation (5.6), with the assumption of using a sinusoidal sub-oscillation control with third harmonic, where the maximum value of m_a is equal to $\frac{2}{\sqrt{3}}$.

$$v_{s\,max} = \sqrt{\frac{3}{2}} m_a \frac{V_{dc}}{\sqrt{2}} = \frac{400}{\sqrt{2}} V. \tag{5.6}$$

To define the machines' operating ranges, it is necessary to calculate the value of the base speed. This is obtained by solving the system of equations (5.7), which are based on the vector diagrams in Fig. 5.1a.

$$\begin{cases} v_{s\,max} = \sqrt{v_{sd}^2 + v_{sq}^2}, & \text{(5.7a)} \\ v_{sd} = -\omega_m L_s i_{sq}, & \text{(5.7b)} \\ v_{sq} = R_s i_{sq} + \omega_m \psi_{pm}. & \text{(5.7c)} \end{cases}$$

Adding the components of the stator voltage of (5.7c) and (5.7b) into (5.7a), the second-degree equation can be solved, from which the value of ω_b=330.2 rad/s (3153.41 rpm) is obtained.
The maximum speed, on the other hand, is calculated in the equation (5.8):

$$\Omega_{m\,max} = \frac{v_{max}}{3.6 d_r G_r} = 666.7 \frac{rad}{s}. \tag{5.8}$$

Then, in order to properly control the machine in all operating regions, the current amplitude i_{sd} must be regulated in such a way as to comply with the previous chapter (5). In order to do this, a script has been implemented on MatLab that will set $i_{sd} = 0$, if the speed is less than the base one, or otherwise, with $\omega > \omega_b$, it will define the value of i_{sd} to ensure a correct motor de-fluxing and to guarantee a stator voltage equal to $v_{s\,max}$.

The work area is also taken into account when i_{sq}. Here, the value for i_{sd} is setted and the control imposes an i_{sq} inversely proportional to the speed. Also a control must be added that does not allow the voltage v_{sq} to reach negative values.
In this way, the operating regions of the synchronous permanent-magnet machine can be accurately reproduced and, by means of the non-linear system of equations (5.9), derived from the Figure 5.1b, the value to be taken by the current i_{sd} is computed.

$$\begin{cases} i_{s\,max} = \sqrt{i_{sd}^2 + i_{sq}^2}, \\ v_{s\,max} = \sqrt{v_{sd}^2 + v_{sq}^2}, \\ v_{sd} = R_s i_{sd} - \omega_m L_s i_{sq}, \\ v_{sq} = R_s i_{sq} + \omega_m L_s i_{sd} \omega_m \psi_{pm}. \end{cases} \tag{5.9}$$

5.2. Simulink control model

The lookup table based control system proposed to perform the simulations and to verify the validity of the analysed solutions is the one represented in Figure 5.2. It is based on the control of the two components of the stator current, in order to obtain a voltage regulation of the open-end winding motor.

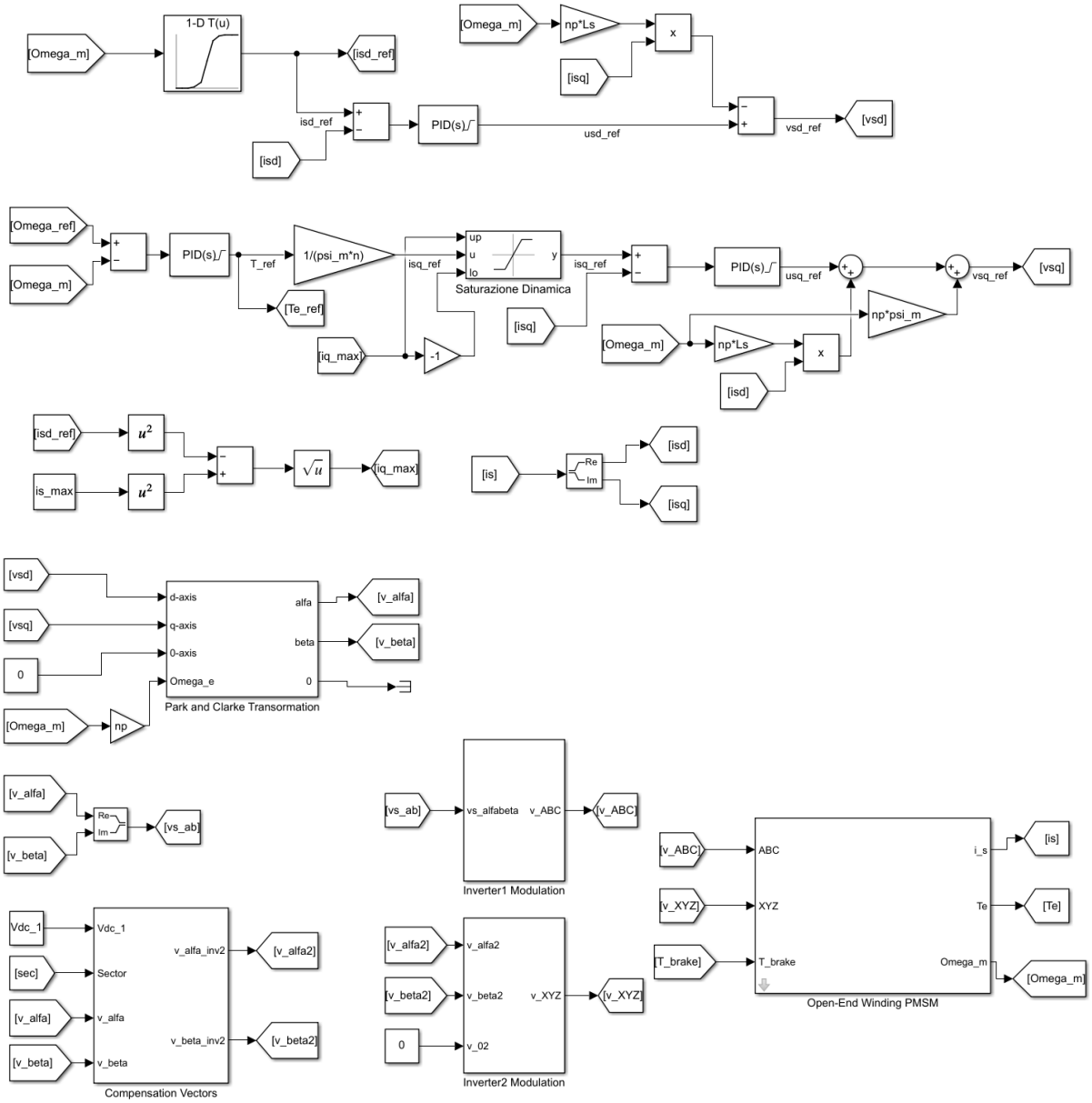

Figure 5.2: Overall control system for the lookup table based modulation.

The main structure of the control system is based on the differential equations of the motor (5.10), (5.11). These are represented in Figures 5.3a and Figure 5.3b, in which the two components of the stator voltage are obtained.

$$v_{sd} = R_s i_{sd} + L_s p i_{sd} - \omega_m L_s i_{sq}, \tag{5.10}$$

$$v_{sq} = R_s i_{sq} + L_s p i_{sq} + \omega_m L_s i_{sd} + \omega_m \psi_{pm}. \tag{5.11}$$

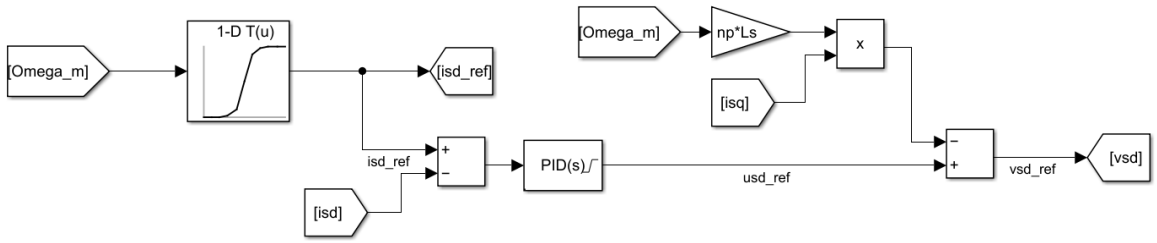

(a) d-axis reference stator voltage.

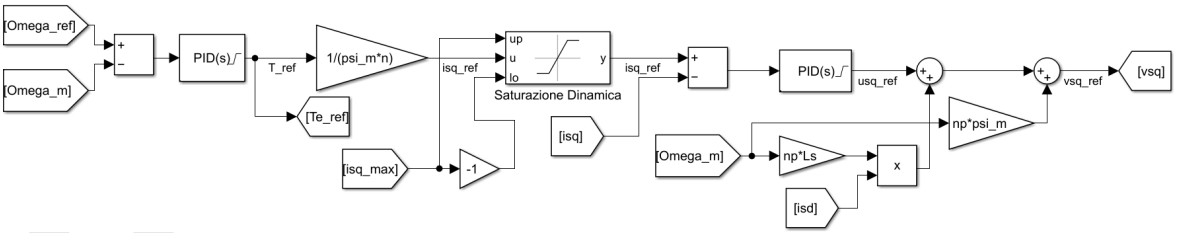

(b) q-axis reference stator voltage .

Figure 5.3: Control diagram for reference stator voltages dq-axis.

The reference stator current $i_{sd\,ref}$ is directly derived from the lookup table visible in Figure 5.3a. The latter implements the MatLab script described above, to obtain the operating regions of the machine. It has also as input the mechanical speed Ω_m exiting from the open-end motor winding model in Figure 5.12.

Instead, a speed controller is used to determine the reference current $i_{sq\,ref}$, which has the function of calculating the electromagnetic torque required to eliminate the difference between the mechanical speed Ω_m and the Ω_{ref}, obtained from the performance telemetry data of the electrical vehicle under test, shown in Figure 5.4.

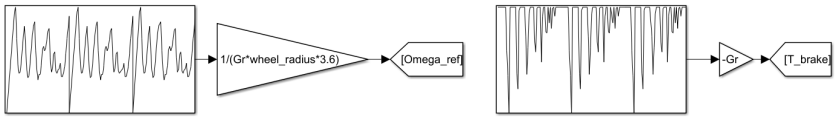

Figure 5.4: Telemetry of speed and braking torque during a hot lap at the Varano circuit.

At the output of the PI controller, the reference trend of the electromagnetic torque $T_{e\,ref}$ is obtained. Then, by means of the inverse formula of the equation (3.11), the current $i_{sq\,ref}$ is computed. With the equation (5.1), implemented on Simulink as represented in Figure 5.5, the current $i_{sq;max}$ is calculated, which will be reduced as the current $i_{sd\,ref}$ increases. Dynamic saturation is used to limit the value of $i_{sq\,ref}$ when the maximum value just obtained varies.

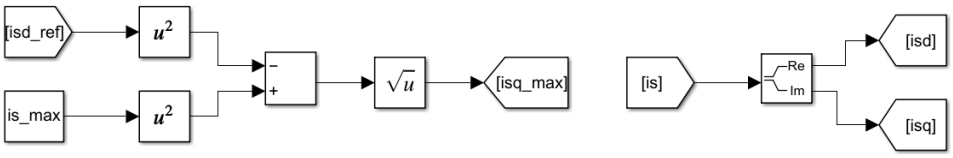

Figure 5.5: Computation of the stator currents i_{sd}, i_{sq}, and the value of $i_{sq\,max}$.

The vector of the stator current i_s output from the motor also appears in Figure 5.5. From this, the two components i_{sd} and i_{sq} are taken, which are used in the respective controllers to calculate the error with respect to the reference that will be injected into the PI controllers.
The parameters K_p, K_i and the coefficients of the anti-windup have been computed using the MatLab function *pidtune*. In order to do this, it is necessary to define the transfer functions of the mechanical load and of the two current controllers, described by the equations (5.12), (5.13) respectively.

$$G_{mec}(s) = \frac{1}{4\beta + sJ}. \tag{5.12}$$

$$G_{el}(s) = \frac{1}{R_s + sL_s}. \tag{5.13}$$

While, the phase margin was set at 88° to avoid overshoot, as much as possible, and to improve system stability. Finally, the two natural time constants of the system were also calculated, which are given in the equations (5.14), (5.15). Through these, the frequencies used in PI controllers to speed up the system's response (5.16), (5.17) are obtained:

$$\tau_{n\,mec} = \frac{J}{4\beta}. \tag{5.14}$$

$$\tau_{n\,el} = \frac{L_s}{R_s}. \tag{5.15}$$

$$\omega_{mec} = \frac{1}{k_m \tau_{n\,mec}}. \tag{5.16}$$

$$\omega_{el} = \frac{1}{k_e \tau_{n\,el}}. \tag{5.17}$$

The two coefficients k were obtained experimentally, with the constraint that it must be ensured that the inner loop is at least 10 times faster than the outer loop. This guarantees that the PI regulators can be individually designed.

In the speed controller, a saturation at $\pm T_{max}$ was also used as the lower and upper limit. At the output of the two current PIs, the voltages $u_{sd\,ref}$ and $u_{sq\,ref}$ are obtained, which are shown in Figures 5.3a, 5.3b. In the last part of the control, both the coupling terms between the two loops, $-\omega_m L_s i_{sq}$ and $\omega_m L_s i_{sd}$, and the induced electromotive force $\omega_m \psi_{pm}$ are compensated. As a result, the stator reference voltages $v_{sd\,ref}$ and $v_{sq\,ref}$ are obtained. Figure 5.6 shows the subsystem used to obtain the stator voltage components v_α and v_β, on the fixed-axis reference frame, for the modulation of the two inverters.

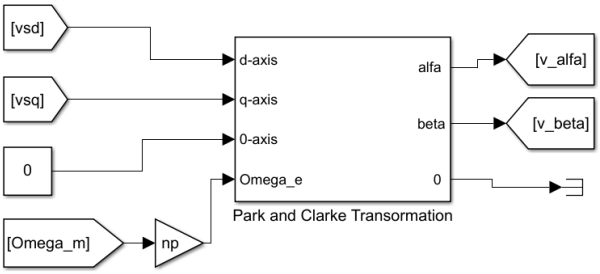

(a)

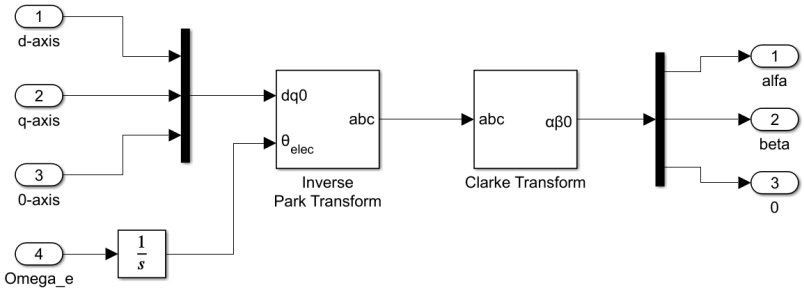

(b)

Figure 5.6: Subsystem for Park and Clarke transformations.

To do this, it is necessary to use Park's inverse transform and Clarke's transformation. The former derives the three phase voltage from the components on the *dq0* axes of the rotating reference frame. Instead, with Clarke's transform, the components on the $\alpha\beta$ axes are obtained from the phase voltages.
To perform these conversions, the blocks in the Simulink library are used directly. The one for the inverse transformation of Park requires the electric angle θ_e and the matrix formula described in the equation (5.18).

$$\begin{aligned} \begin{bmatrix} v_a \\ v_b \\ v_c \end{bmatrix} &= T(\theta)^t \begin{bmatrix} v_d \\ v_q \\ v_0 \end{bmatrix}, \\ \begin{bmatrix} v_a \\ v_b \\ v_c \end{bmatrix} &= \sqrt{\frac{2}{3}} \begin{bmatrix} \cos(\theta) & -\sin(\theta) & \frac{1}{\sqrt{2}} \\ \cos(\theta - \frac{2}{3}\pi) & -\sin(\theta - \frac{2}{3}\pi) & \frac{1}{\sqrt{2}} \\ \cos(\theta - \frac{4}{3}\pi) & -\sin(\theta - \frac{4}{3}\pi) & \frac{1}{\sqrt{2}} \end{bmatrix} \begin{bmatrix} v_d \\ v_q \\ v_0 \end{bmatrix}. \end{aligned} \tag{5.18}$$

The electrical angle is obtained by integrating the mechanical output speed of the motor, Ω_m, multiplied by the number of pole pairs. In addition, it is also necessary to impose that the d-axis is initially aligned with the a-phase of the motor, to comply the convention shown in Figure 3.2 (with $s1 = a$).

In the Clarke transform, on the other hand, the angle is set equal to zero as it uses a fixed-axis reference frame, whose matrix is represented in the equation (5.19):

$$\begin{aligned} \begin{bmatrix} v_\alpha \\ v_\beta \\ v_0 \end{bmatrix} &= T_0 \begin{bmatrix} v_a \\ v_b \\ v_c \end{bmatrix}, \\ \begin{bmatrix} v_\alpha \\ v_\beta \\ v_0 \end{bmatrix} &= \sqrt{\frac{2}{3}} \begin{bmatrix} 1 & -\frac{1}{2} & -\frac{1}{2} \\ 0 & \frac{\sqrt{3}}{2} & -\frac{\sqrt{3}}{2} \\ \frac{1}{\sqrt{2}} & \frac{1}{\sqrt{2}} & \frac{1}{\sqrt{2}} \end{bmatrix} \begin{bmatrix} v_a \\ v_b \\ v_c \end{bmatrix}. \end{aligned} \tag{5.19}$$

As mentioned above, the stator reference voltage $v_{\alpha\beta}$ is used to realise the modulations of the two inverters, which were analysed in chapter 4, depicted in Figure 5.7.

For the first inverter (Figure 5.7a), a lookup table is used to determine, in which of the six sectors of the reference frame, the voltage vector $v_{\alpha\beta}$ is located, and it must have a positive angle. According to the sector obtained from the lookup table, the *multiport switch* sends the respective switching states to Inverter1. These values were set in such a way as to comply with the cases analysed in the table 4.1.

Instead, inverter2 (Figure 5.7b) employs a space vector modulation based on the value of the compensation vector, which uses the switching frequency and sampling time given in the Table 5.2. Instead, the compensation vector is derived using the Table 4.2, implemented on Simulink as shown in Figure 5.8. Therefore, depending on the sector in which the vector $\bar{v}_{\alpha\beta}$ is located, the components on the $\alpha\beta$ axes of the reference voltage vector for the second inverter are generated by means of two lookup tables, which realise the equations of the Table 4.2.

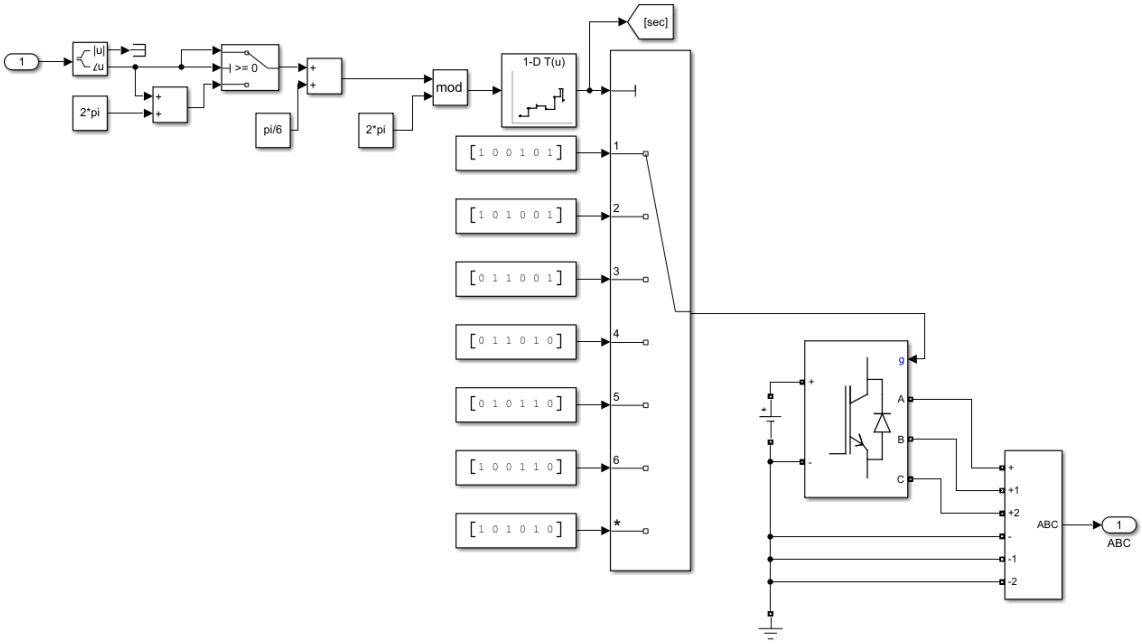

(a) Control system used for Inverter1.

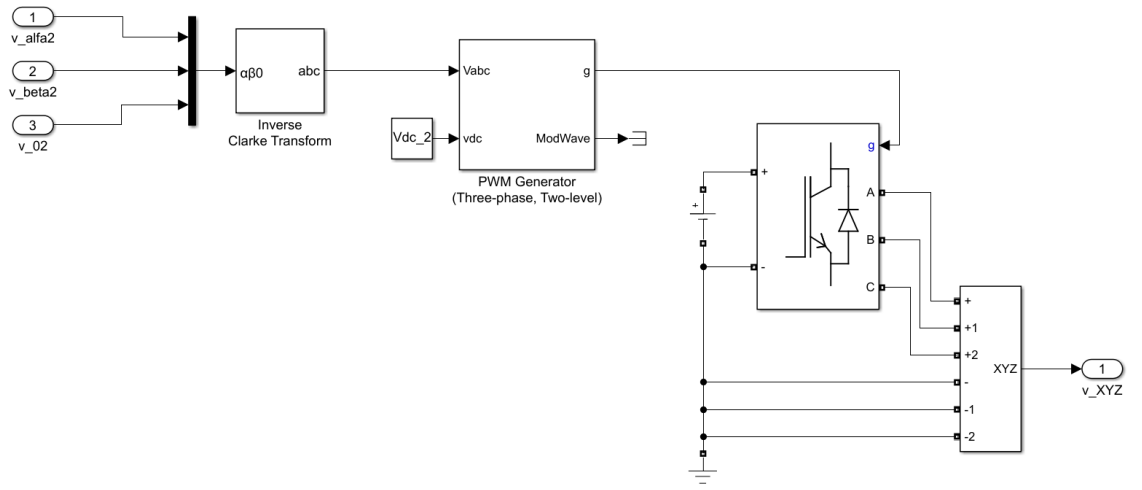

(b) Control diagram applied to Inverter2.

Figure 5.7: Modulation techniques employed for the two inverters in the lookup table based control.

In these two block diagrams, the voltages at the inverter ends are computed using the Simulink blocks *voltage measurement*, in order to obtain the two three-phase voltages that will be fed into the OW motor model.
$v_{\alpha 2}$ and $v_{\beta 2}$ are converted to the three-phase voltage triplet through the inverse Clarke transform, obtained from the transposed matrix of that shown in equation (5.20).

$$\begin{bmatrix} v_a \\ v_b \\ v_c \end{bmatrix} = T_0^t \begin{bmatrix} v_\alpha \\ v_\beta \\ v_0 \end{bmatrix}, \qquad \begin{bmatrix} v_a \\ v_b \\ v_c \end{bmatrix} = \sqrt{\frac{2}{3}} \begin{bmatrix} 1 & -\frac{1}{2} & -\frac{1}{2} \\ 0 & \frac{\sqrt{3}}{2} & -\frac{\sqrt{3}}{2} \\ \frac{1}{\sqrt{2}} & \frac{1}{\sqrt{2}} & \frac{1}{\sqrt{2}} \end{bmatrix} \begin{bmatrix} v_\alpha \\ v_\beta \\ v_0 \end{bmatrix}. \tag{5.20}$$

The SVPWM modulation is applied using the *PWM Generator* block, represented in Figure 5.8, to handle the switching states of the second inverter.
Both inverters are IGBTs, and the DC-link voltage applied to their leads is set to the values given above in Table 5.2.

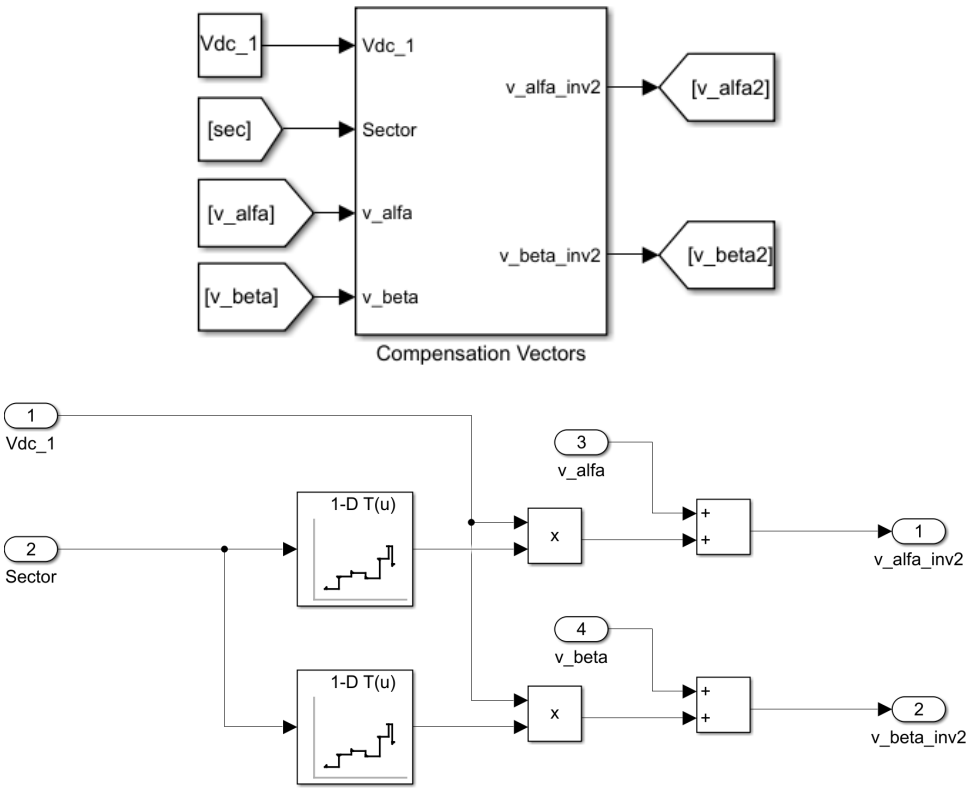

Figure 5.8: Inverter2 compensation vector generation.

Instead, as regards the control scheme with the 180° decoupled SVPWM method, the system employed is the same as the one just analysed, but, of course, the blocks that handle the modulation of the dual-inverter must be changed.
More precisely, after having derived the two reference voltages v_{sd} and v_{sq}, from the diagram in Figure 5.3, these are converted into the corresponding three-phase *abc* components of the stator voltage vector by means of the Park anti-transformation in the equation (5.18).

Furthermore, the magnitude of the voltage vector has to be halved by means of the *gain* blocks, as shown in Figure 5.9, with which the 180° phase shift between the two vectors can also be obtained.

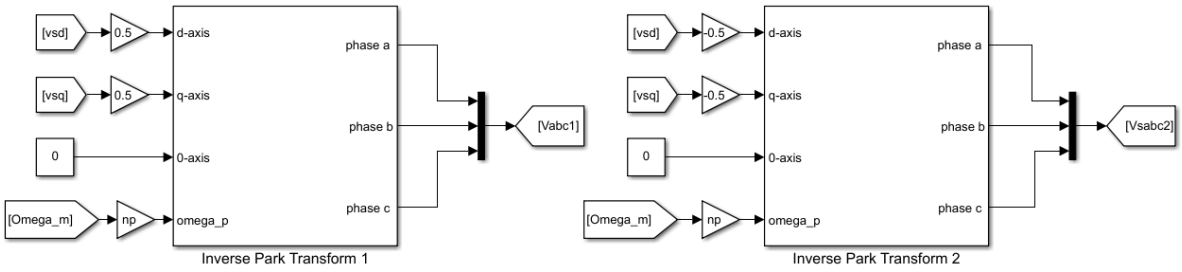

Figure 5.9: Generation of reference voltage vectors for the 180° decoupled scheme.

These two voltage vectors are then fed into the modulation of the corresponding inverters, which is performed in the same way, as shown in Figure 5.10a and 5.10b. Indeed, the Simulink *PWM Generator* block is used to generate the switching states of the two IGBTs, as in the case analysed above, by setting a space vector modulation.
The two DC-links were setted at 200 V, to obtain a total value equal to that of the DC source that will be used in the model of the conventional PM synchronous motor.

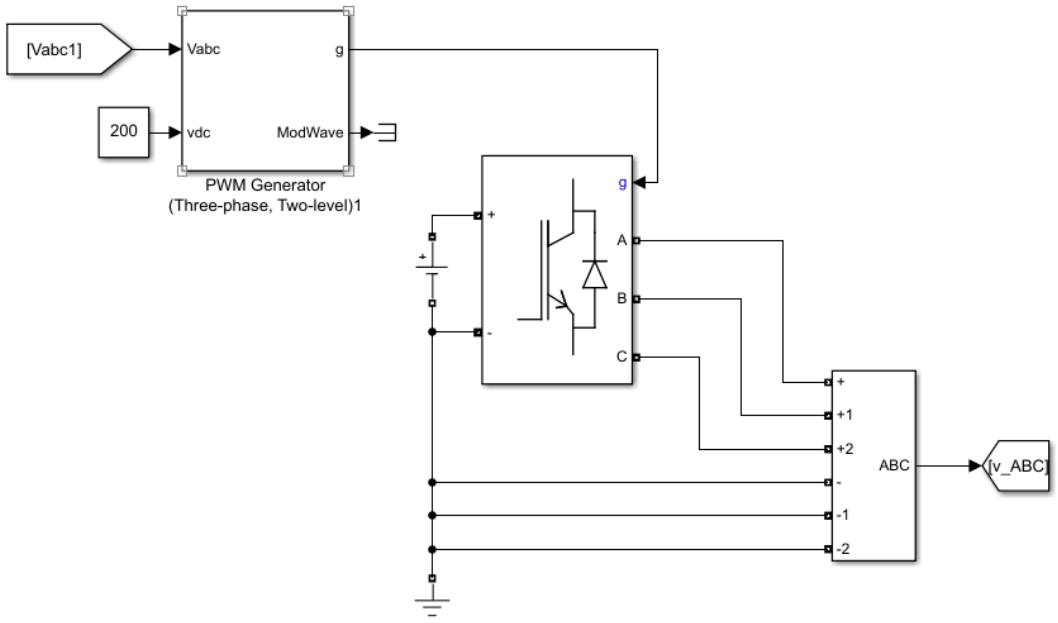

(a) Control system used for Inverter1.

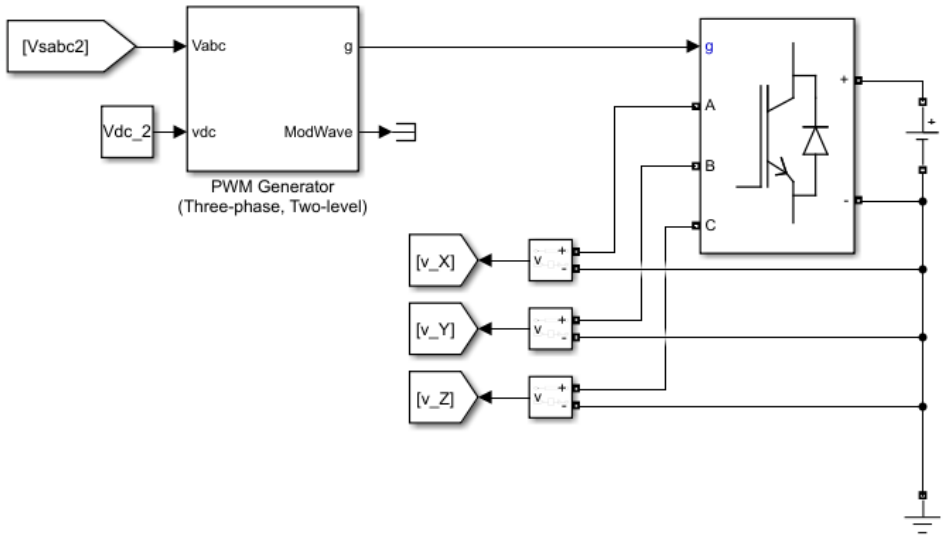

(b) Control diagram applied to Inverter2.

Figure 5.10: Modulation techniques employed for the dual-inverter in the 180° decoupled SVPWM.

Finally, the open-end winding motor model, shown in Figure 5.12, was implemented, in which the dynamic equations (5.21) of the machine were recreated on Simulink.

$$\begin{cases} \bar{v}_s = R_s \bar{i}_s + p\bar{\psi}_s + j\omega_m \bar{\psi}_s, \\ \psi_{sd} = L_s i_{sd} + \psi_{pm}, \\ \psi_{sq} = L_s i_{sq}, \\ p\omega_m = \dfrac{n_p}{J_{eq}}(T_e - T_r), \\ T_e = n_p \psi_{pm} i_{sq}. \end{cases} \tag{5.21}$$

Figure 5.11 illustrates the inputs of the OW motor model, i.e. the two three-phase voltages generated by the two inverters, and the braking torque T_{brake}, obtained from the initial telemetry data. The equations (3.1), (3.2) were implemented to generate the space vector of the stator voltage.

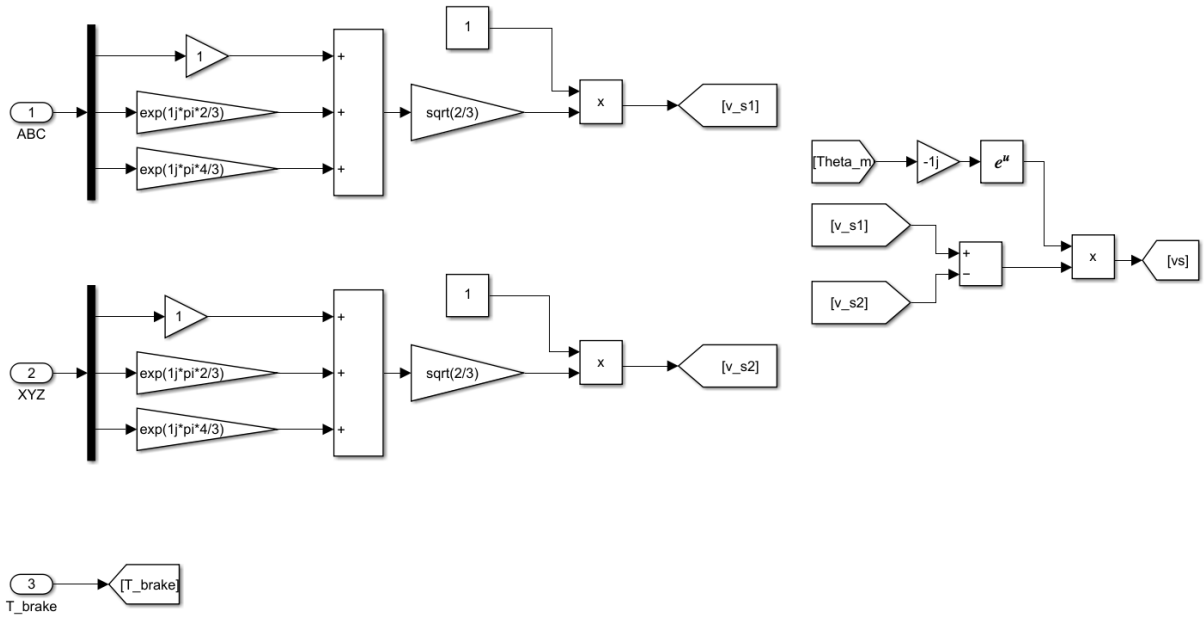

Figure 5.11: Computation of the space vector for the OW motor stator voltage.

The model's output quantities are the stator current i_s, the electromagnetic torque T_e, and the mechanical speed of the motor Ω_m.

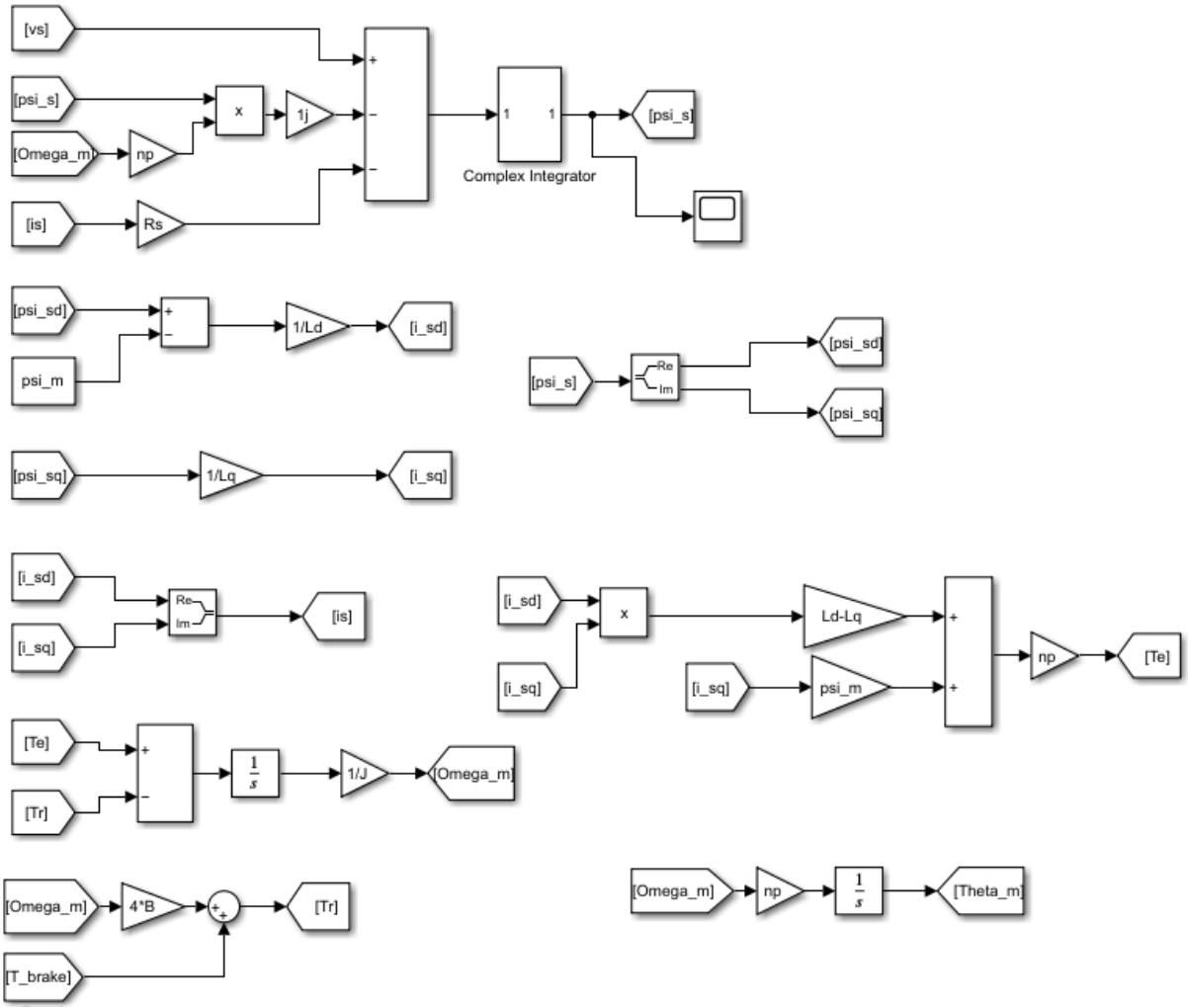

Figure 5.12: Open-end winding motor model.

6 | Simulation and experimental results

To verify the proper operation of the control and modulation strategies of the open-end winding motor, simulations were carried out on Simulink.
The performance of a permanent magnet synchronous motor, with star-connected stator winding neutral point, will be also compared with the same parameters as the OW motor in Tables 5.1, 5.2.
Finally, for both engine types, simulations will be carried out with telemetry data obtained from an electric vehicle hot lap on the Varano circuit, in order to obtain a comparison of the main electrical and mechanical quantities of the two different systems analysed.

6.1. Checks of motor model and control system operation

Before analysing the results obtained from the operation of the overall system, shown in Figure 5.2, simulations were performed to verify the Simulink model.
This was done mainly to verify the behaviour of the motor model and the correct functioning of the operating regions script.
To do this, a ramp velocity reference was applied, with the combination of *ramp* and *saturation* blocks, in Figure 6.1, to set the maximum value less than that of the base velocity ω_b equal to $330.2 rad_{el}/s$ (or in terms of mechanical speed $\Omega_b = \omega_b/n_p = 165.11 rad/s = 1576.79 rpm$).
In all simulations performed, reference speed values are set in mechanical and not electrical radians, as is the case for the output speed of the motor model.

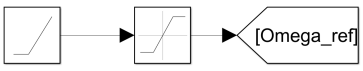

Figure 6.1: Simulink block to realize the reference speed.

In this case, the model of the open-end winding motor receives as input directly the stator voltage components v_{sd} and v_{sq} by means of the control system in Figure 5.3.
Obviously, before entering into the electric motor, they are converted into the respective set of three-phase voltage v_a, v_b and v_c via the Park transform in equation (5.6).
Furthermore, in order to verify the duality of the open-end winding motor, the three remaining voltages, in this case v_x, v_y and v_z are short-circuited as shown in Figure 6.2, resulting in a classical brushless AC motor.
The same trends must, of course, be obtained for the mechanical and electrical quantities if the reverse operation is performed, i.e. if the input v_{xyz} is powered and a null constant is set on that v_{abc}.

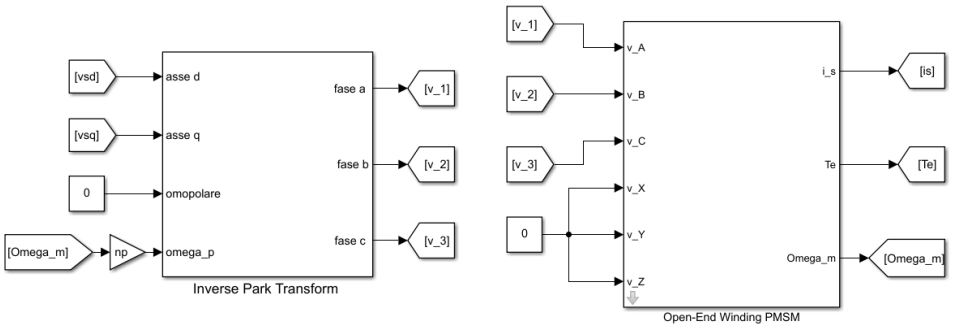

Figure 6.2: Motor configuration to test operation and to verify the internal model.

By setting a maximum reference speed of $150 rad/s$, therefore lower than ω_b, the trends in Figure 6.3 are obtained. It can be seen that the control allows the motor to correctly follow the reference speed. Furthermore, by observing what was said in the chapter 5, current i_{sd} is kept at a zero value, allowing maximum torque to be obtained from the motor. Thus, the value of current i_{sq} can assume the maximum value of the stator current.

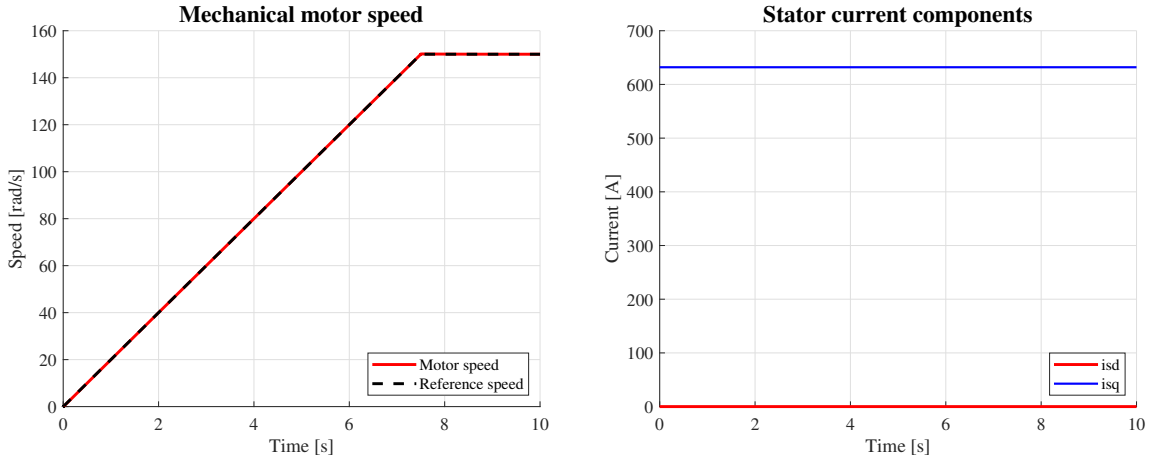

Figure 6.3: Stator current components trends for speeds below the base speed.

On the other hand, setting a speed of $300 rad/s$, it can be seen from the Figure 6.4 how the current i_{sd} starts to become negative, in order to counteract the emf E, when the speed becomes greater than the value of ω_b. At the same time, i_{sq} begins to decrease as it can no longer be equal to the maximum value of the stator current.

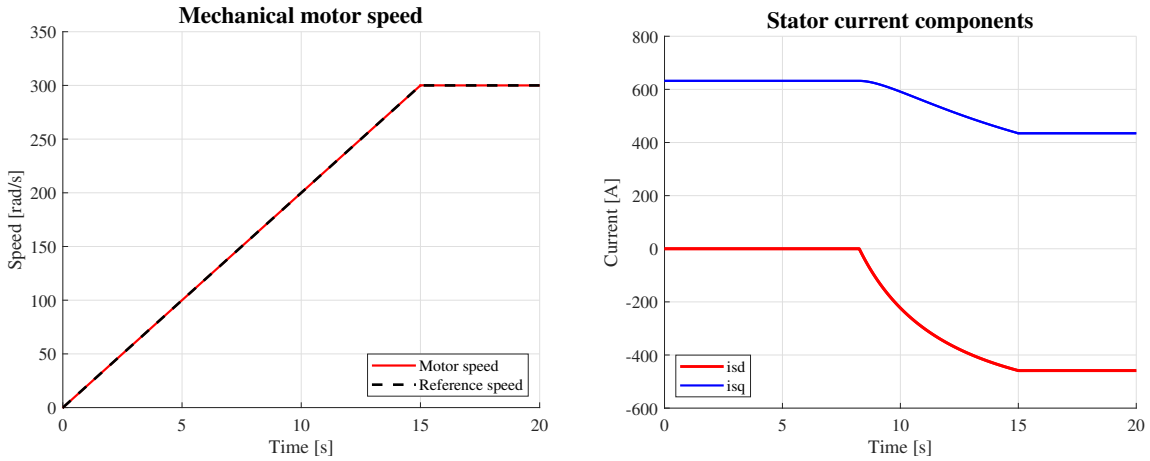

Figure 6.4: Stator current components trends for speeds above the base speed.

To finally verify the correct implementation of the operating regions, the mechanical and electrical quantities of the motor were plotted, as shown in Figure 6.5 and in Figure 6.6.

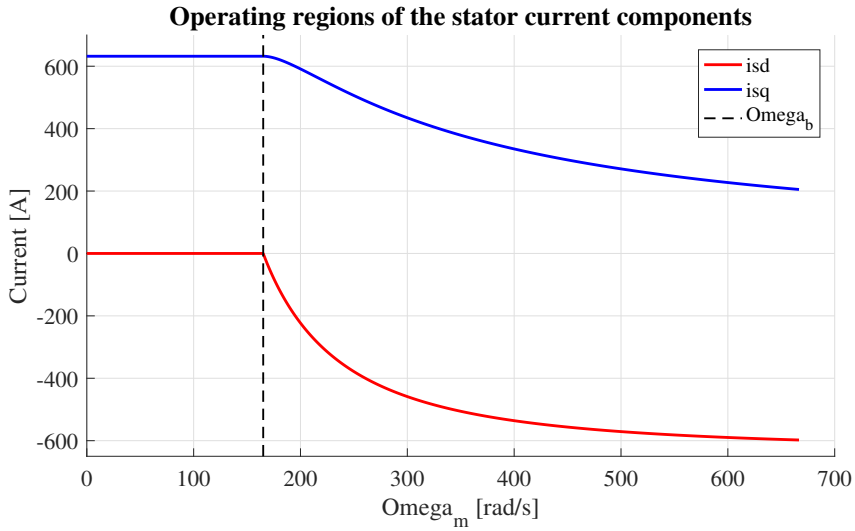

Figure 6.5: Operating region for the dq-axis components of the stator current.

More precisely, in Figure 6.6, it can be seen the difference between the two operating zones in which the motor works. In the first, with $\omega < \omega_b$, the zone of constant electromagnetic torque is observed, while in the second, with values of $\omega > \omega_b$, the trends of stator voltage and current, as well as the motor's power, are correctly seen to become constant.

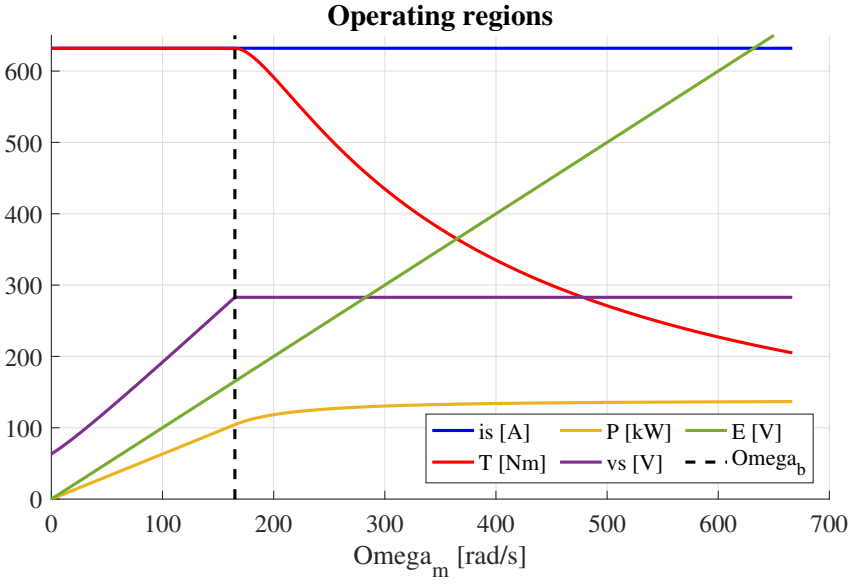

Figure 6.6: Open-end winding motor operating regions.

6.2. Comparison of the two different drive strategies

In this last part, a final comparison of the two control strategies analysed, the decoupled 180° SVPWM and the lookup table six-step modulation, will be performed. As in the previous case, the trends obtained from the application of the two control strategies are examined, for both lower and higher speeds than ω_b, or Ω_b if mechanical radians are used.

6.2.1. Below the base speed

By setting 150 rad/s as the maximum value of the mechanical reference speed, which is less than the 165 rad/s of Ω_b, the trends shown in Figure 6.7 are obtained.

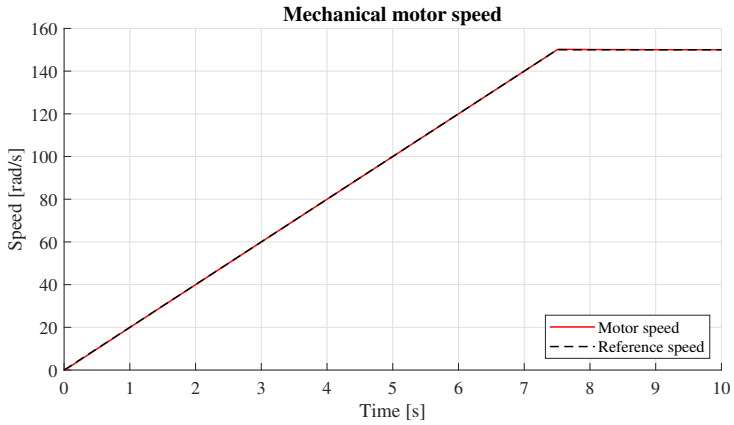

(a) Lookup table based method.

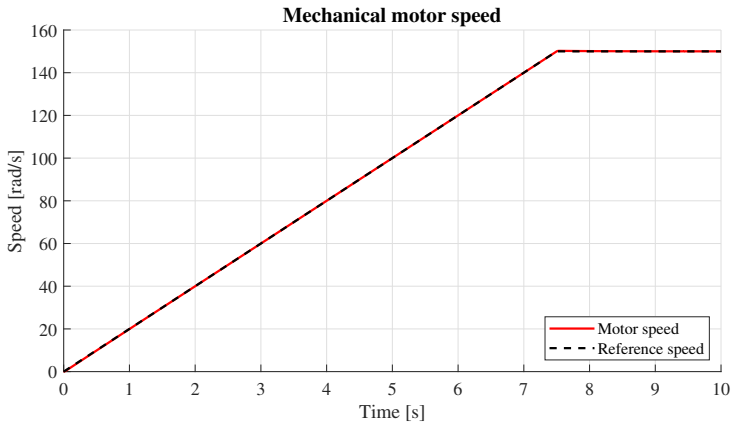

(b) 180° decoupled scheme

Figure 6.7: Mechanical motor speed.

It can be noted that in both control systems, the motor speed follows the reference correctly, with the exactly same trend. This means that the PI current and speed controllers have been set correctly.

Furthermore, as can be seen in Figure 6.8, since the motor is below the base speed, the d-axis component of the stator current is fixed to zero. Whereas, the q-axis component has an initial step increase and keeps increasing slightly until about 8 seconds, to provide the electromagnetic torque required for the motor to reach the reference speed. Once the open.end winding motor has reached a speed of 150 rad/s, i_{sq} is stabilised to 50 A, keeping the speed and torque constant.

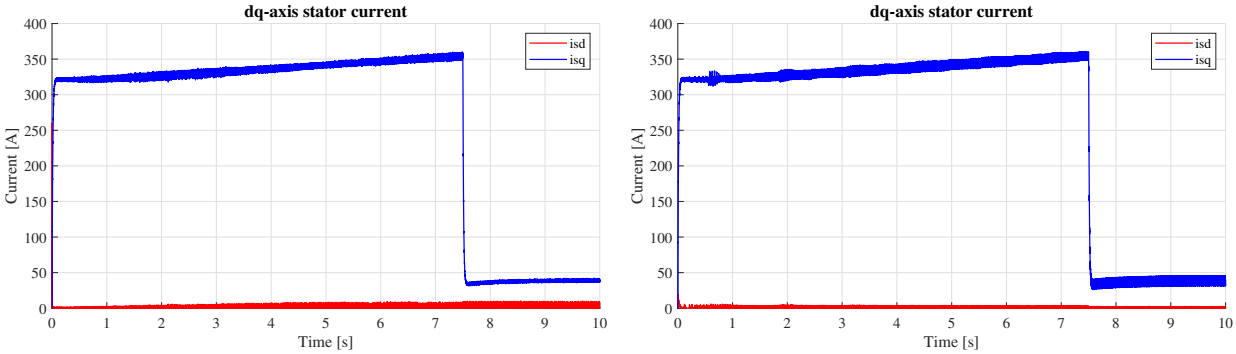

(a) Lookup table based method.

(b) 180° decoupled scheme

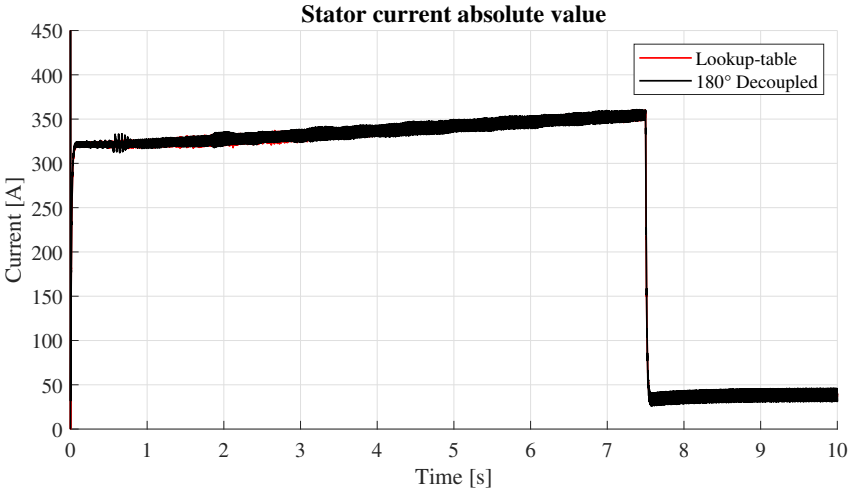

(c) Stator current modulus comparison

Figure 6.8: Stator current trends.

As regards the stator current, the same trend is achieved in the two modulation techniques, except for particular oscillations, as for that of the current magnitude i_s. All the three currents remain below the calculated values in the operating regions, as depicted above in Figure 6.8.

Moreover, the electromagnetic torque and the electric power generated by the motor also have overlapping trends between those obtained in the two systems. The T_e shown in Figure 6.9 is properly proportional to the stator current i_{sq}.

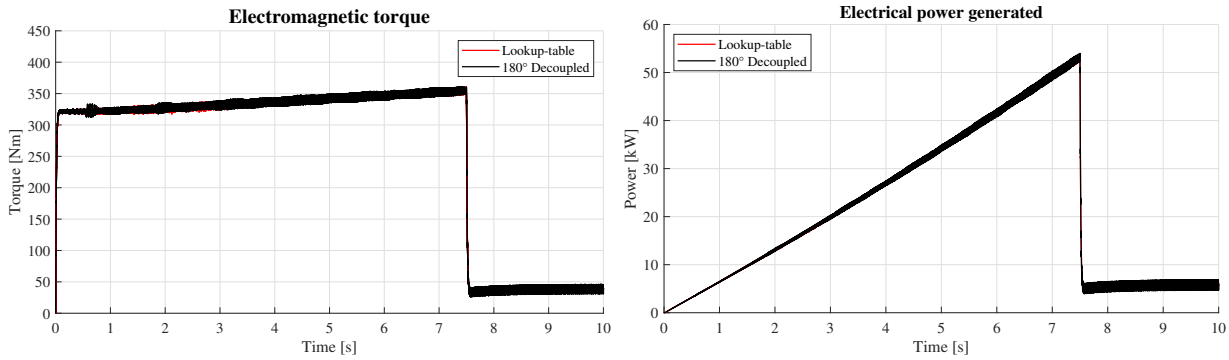

Figure 6.9: Electromagnetic torque and electric power trends.

6.2.2. Above the base speed

In order to exceed the base speed Ω_b, as in the case of the operating regions analysis, a speed of 300 rad/s was set.

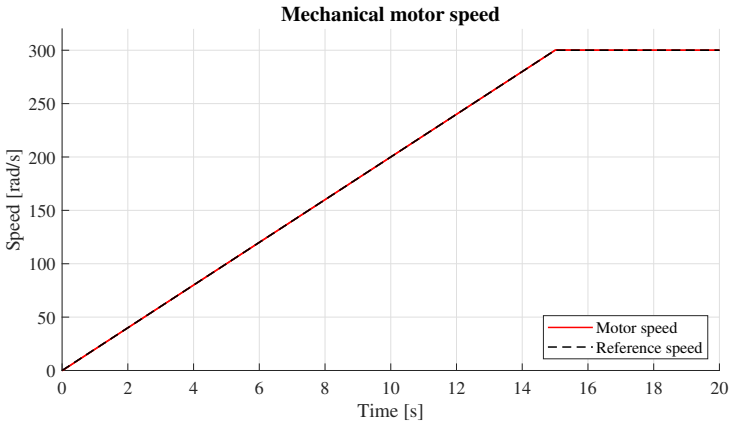

(a) Lookup table based method.

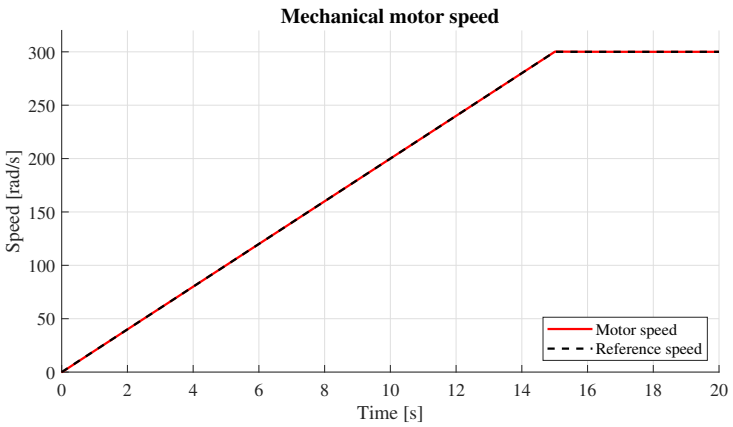

(b) 180° decoupled scheme

Figure 6.10: Mechanical motor speed.

From the simulations performed, the mechanical speeds for the two modulation techniques were derived, which are shown in Figure 6.10. Again, the motor speed accurately tracks the reference for the control startegies.Therefore, the implemented controllers also operate correctly in this motor operation zone.
Unlike the previous case, after about 8 seconds, Ω_b is exceeded, thereby the OW motor enters in the flux-weakening region. In this moment, as illustrated in Figure 6.11, the current i_{sd} starts to decrease, taking on negative values to counteract the induced emf E, before stabilising once the set speed value is reached.

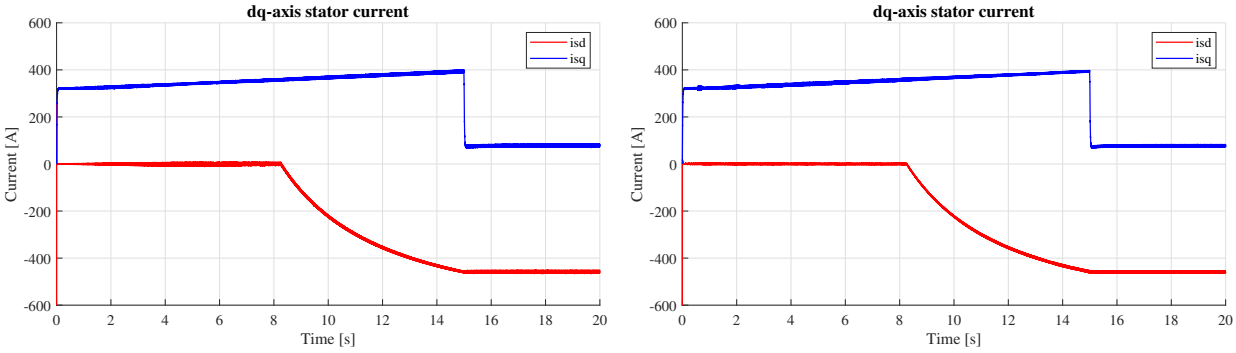

(a) Lookup table based method.

(b) 180° decoupled scheme

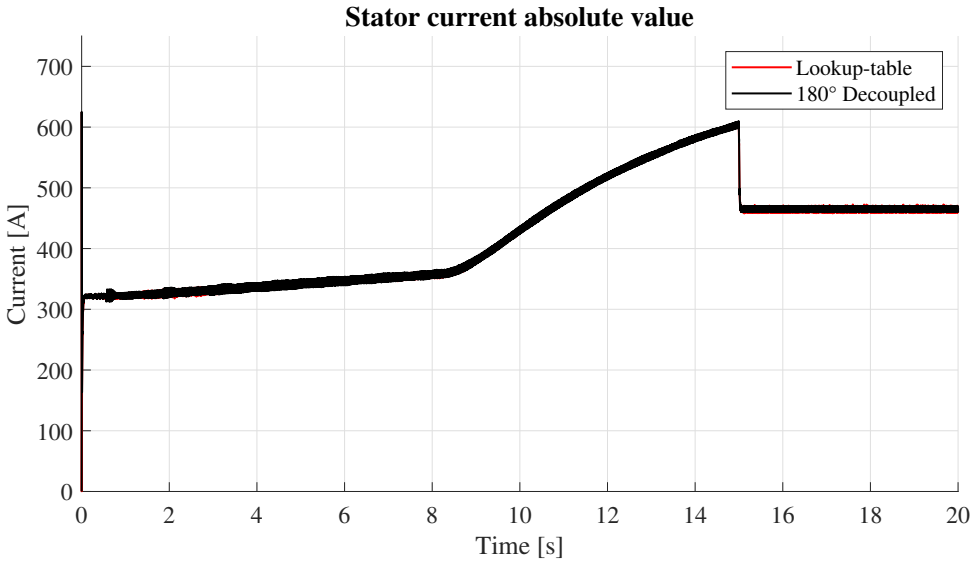

(c) Stator current modulus comparison

Figure 6.11: Stator current trends.

On the other hand, the q-axis current did not change from the trend in the previously analysed case (with $\Omega < \Omega_b$), since the maximum value of the stator current was never exceeded in either control system.

For this reason, the torque T_e and the power P_e will also remain unchanged as they are related to the current i_{sq} behaviour, as shown in Figure 6.12.

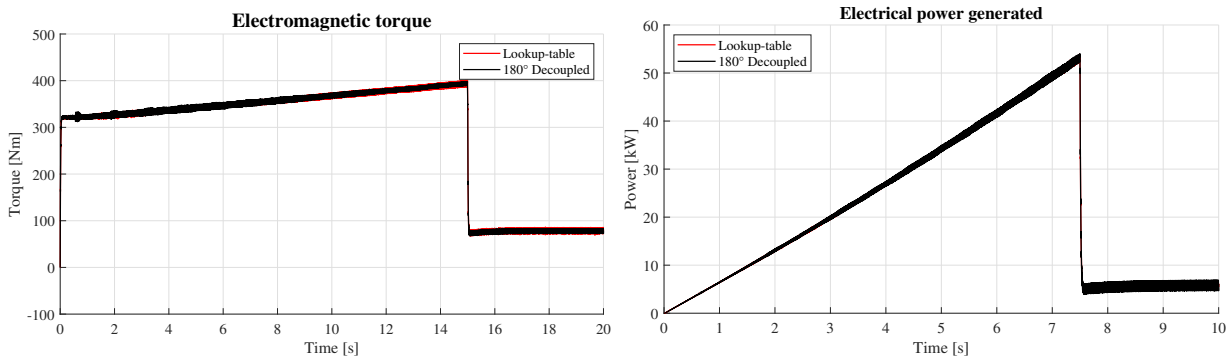

Figure 6.12: Electromagnetic torque and electric power trends.

6.2.3. Comparison in the EV traction application

Experimental simulations were also carried out, in which the the lookup table based method and the 180° decoupled SVPWM scheme were compared in an EV traction application.
This was done by means of telemetry data of speed and braking torque, which will be used as references. They were taken from a lap launched by an electric vehicle on the Varano circuit, which can be seen in Figure 6.13.

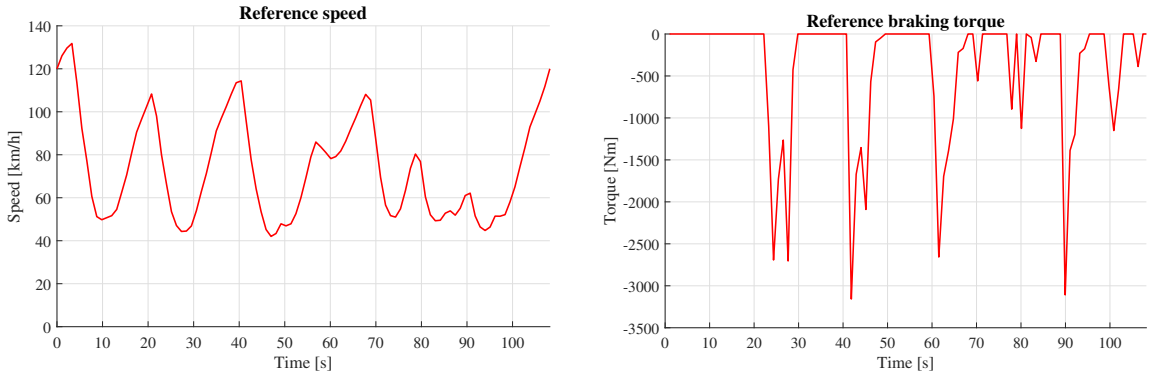

Figure 6.13: Reference speed and braking torque trends.

An initial 20 seconds with constant speed was added to allow time for the motor to reach this value, in order to simulate the pattern of a flying lap. Simulations showed that the mechanical speed trend of the open-end winding motor follows the reference speed correctly. This happens both when the system uses the drive method based on the six-

step generated by the look-up table and also with the 180° decoupled strategy, as shown in Figure 6.14a and Figure 6.14b.

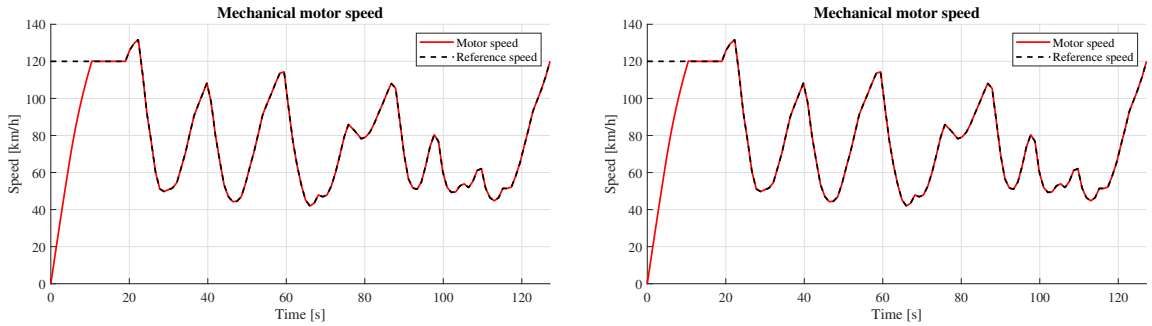

(a) Lookup table based method. (b) 180° Decoupled SVPWM.

Figure 6.14: Speed trends of the two modulation startegies analysed.

As can be seen from Figure 6.15, the speed trends obtained with the two implemented modulation types are perfectly overlapping.

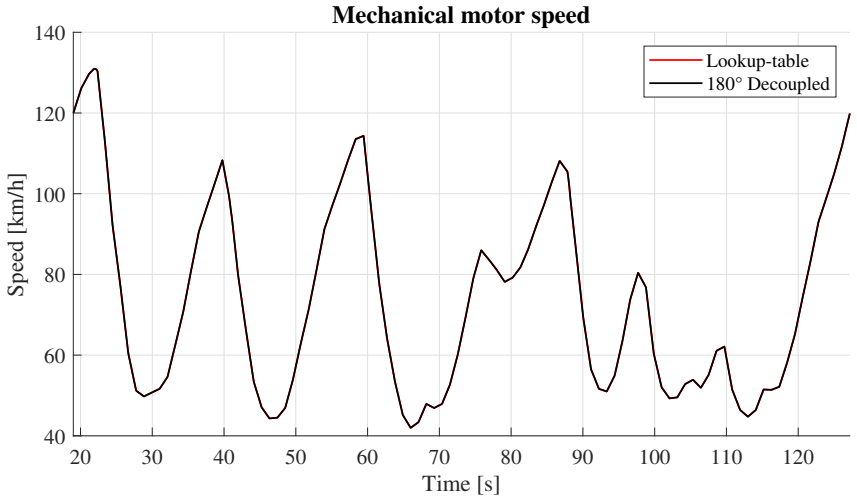

Figure 6.15: Open-end winding motor speed trends.

This means that both strategies work correctly, since the reference is followed optimally, and also that the implemented regulators in the control of the motor have been set appropriately. As regards the trend in mechanical quantities, the torque generated by the open-end winding motor is shown in Figure 6.16.

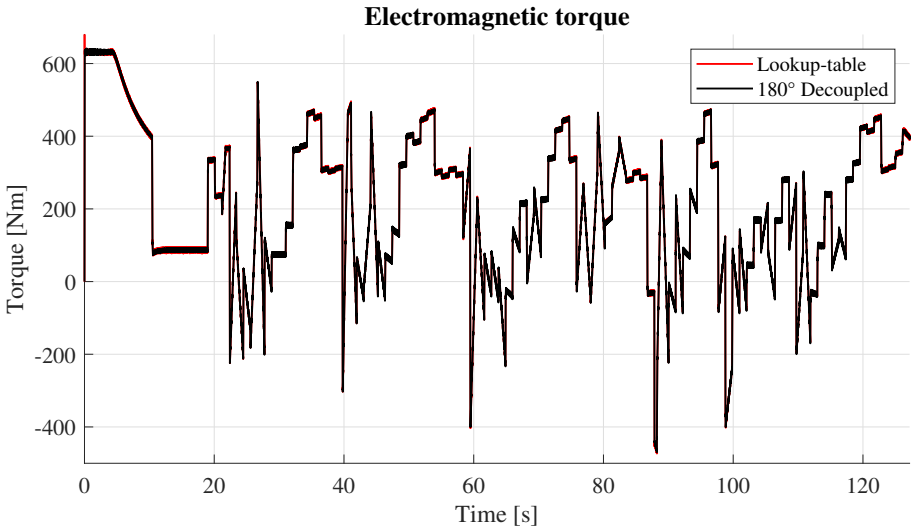

Figure 6.16: Open-end winding motor electromagnetic torque trends.

It can be seen that, as well as having a very similar trend for both analysed methods, the electromagnetic torque T_e complies with that observed in the motor's operating regions. Indeed, it reaches its maximum value of $632Nm$ until it reaches a speed of $120km/h$. In addition, when the base speed is exceeded, the motor torque enters in the flux-weakening region with a decrease proportional to $1/\Omega$, until it stabilises at around $100Nm$. For the remaining part of the simulation, even sudden increases in torque can be observed, but never exceeding the maximum value imposed for T_e in the system.

As in the cases analysed above, the q-axis component of the stator current is calculated in the control system via the value of the electromagnetic torque. Indeed, as shown in Figure 6.17, the current i_{sq} has the same trend of the torque T_e.

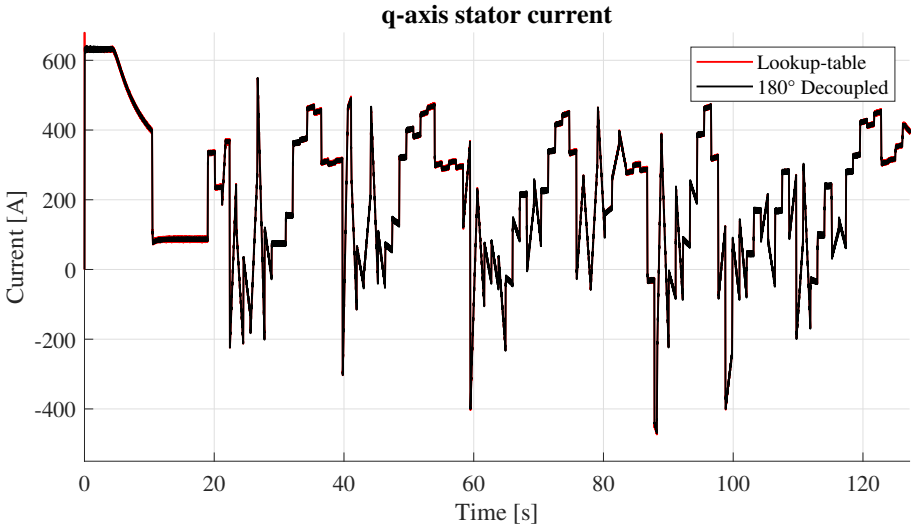

Figure 6.17: q-axis stator current trends.

For both modulation strategies examined, the same trends in the components of the stator current occur.

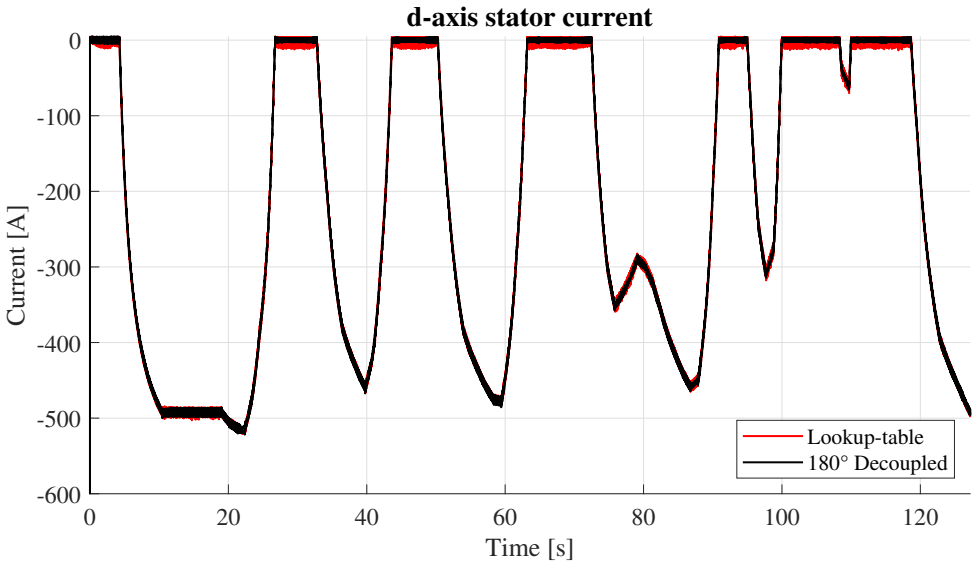

Figure 6.18: d-axis stator current trends.

It is useful to note that current i_{sd} only takes on non-zero values when the speed of the open-end winding motor exceeds the value of the base speed, i.e. in the flux-weakening region. Therefore, it acquires negative values that decrease the current i_{sq}, complying with both the thermal limits and the operating regions of the motor.
This can be seen in Figure 6.19, where the absolute value of the stator current i_s does not exceed its maximum value calculated above at any point.

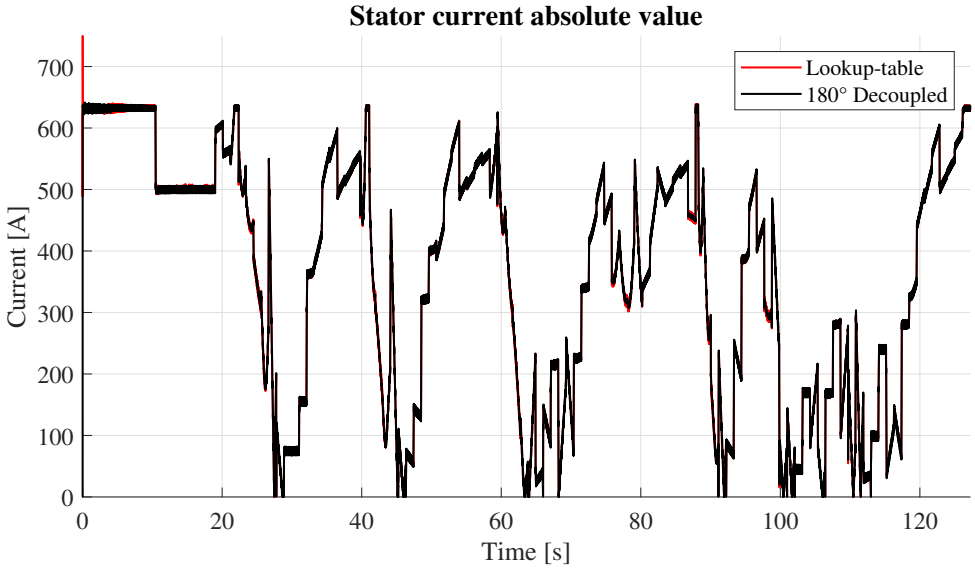

Figure 6.19: Motor stator current absolute value for the two analysed methods.

The electric power generated, by the open-end winding motor during the lap, also shows the same trend for both control strategies implemented, as can be seen in Figure 6.20.

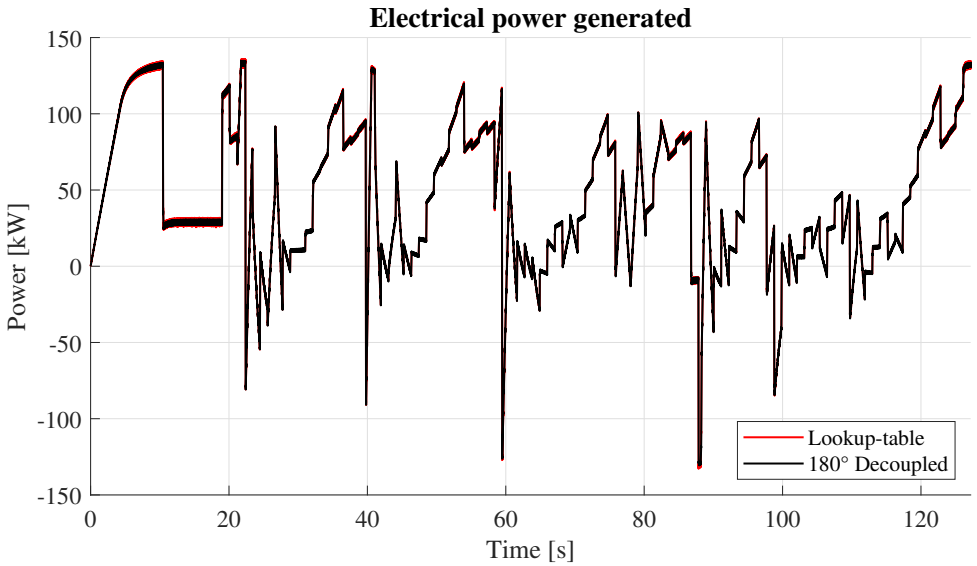

Figure 6.20: Electrical power generated by the OW motor with the two modulation schemes.

From the several comparisons made between the two modulation strategies implemented for the dual-inverter configuration, it can be deduced that both allow the open-end winding motor to work correctly at all points of the operating regions, and thus over a wide speed range.

Furthermore, for the same results obtained, lookup table-based modulation proves to be the best solution as it allows a lower switching frequency for the first invert than the conventional 180° decoupled SVPWM scheme, thus reducing the switching losses in the system.

6.3. Comparison between OW-PMSM and PMSM

The same simulations were also carried out in order to make a direct comparison between an open-end winding and a conventional synchronous motor, both equipped with permanent magnets. Besides the technology used to make these two electric machines, the different types of drive are also investigated.
Indeed, the real improvement that could be achieved by the use of a dual-inverter configuration is verified, through the lookup table-based modulation combining six-step and PWM.

The conventional synchronous motor, on the other hand, utilises the control system in Figure 5.3, from which the components of the reference stator vector $\bar{v}_{s\,ref}$ are derived, to be inserted directly into the motor model. This is implemented through the same electrical and mechanical relationships analysed in the system of equations 5.21 for the open-end winding motor, and using the same total DC-link voltage. Simulation results on traction applications show that, also in this case, the control system and the lookup table-based modulation allow the OW motor to have the same mechanical speed responses as the conventional AC motor, as can be seen in Figure 6.21.

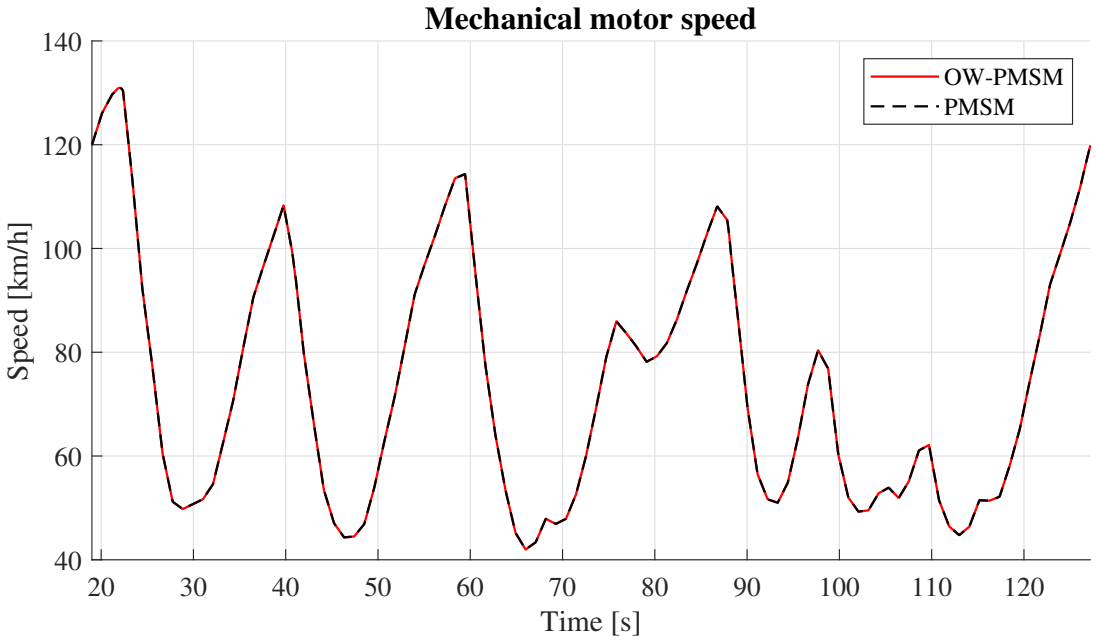

Figure 6.21: Comparison between mechanical speed trends in the two motor types.

Furthermore, as shown in Figure 6.22, the electromagnetic torque developed by the open-end winding motor also coincides with that generated by the permanent-magnet synchronous motor.

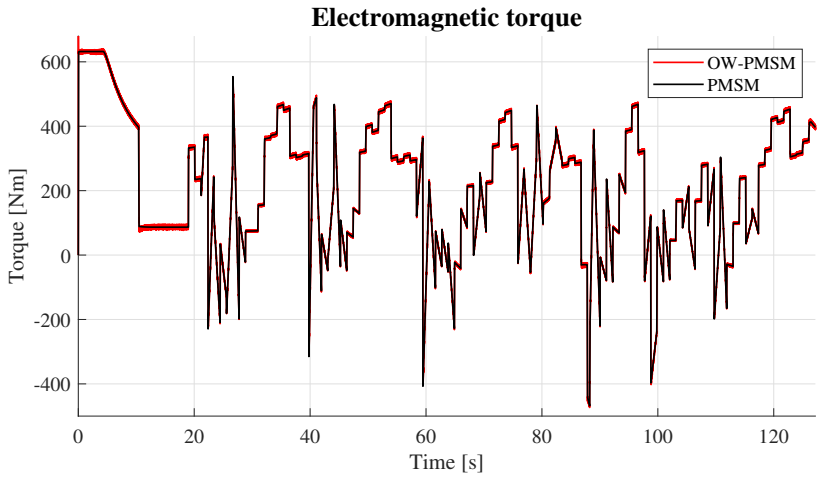

Figure 6.22: Electromagnetic torque trends.

Being directly related to the T_e, the currents i_{sq} of the two types of motor will also have an overlapped trend, as well as for the d-axis stator current component, and thus also for the modulus of i_s, as shown in Figure 6.23.

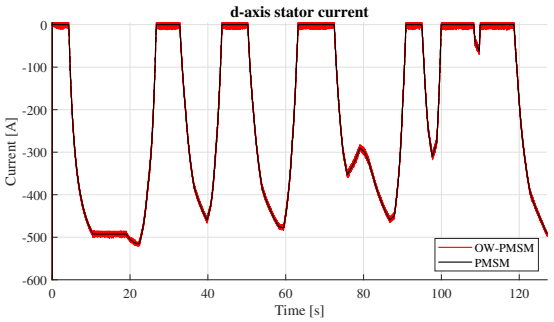

(a) q-axis stator current trends.

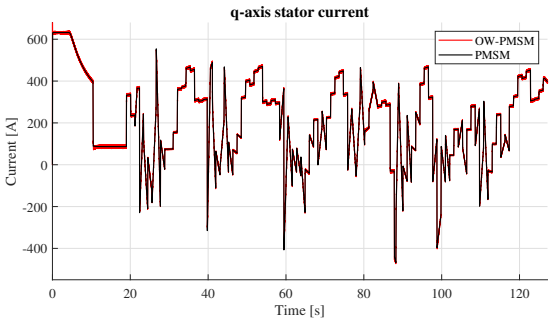

(b) d-axis stator current trends.

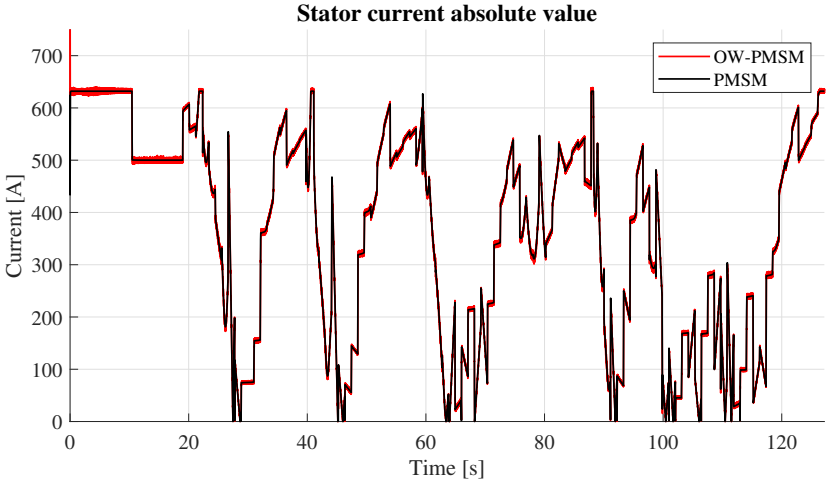

(c) Stator current modulus comparison

Figure 6.23: Stator current trends in the two analysed systems.

Thus, by examining the trends obtained for the two different types of electric motor, it can be stated that hybrid six-step and pulse width modulation strategy achieves the same performance as a conventional permanent magnet synchronous motor, even with the same DC-link voltage.

Therefore, the control scheme based on the look-up table is able to introduce into the system all the benefits of the dual-inverter configuration for an open-end winding motor which cannot be achieved by using a conventional system, such as the absence of the DC/DC converter, improved reliability in fault situations and greater control flexibility.

7 | Conclusions

In the conducted study, the different configurations and applications of an open-end winding motor were analysed, with a greater focus on the ones equipped with permanent magnets as, in recent years, this type of motor configuration has seen an increased application in electric vehicles compared to induction motors.

Among all those proposed in the various papers examined, a hybrid lookup table-based modulation, combining six-step and pulse width modulation, was implemented via a Simulink scheme to drive a dual-inverter system with two independent DC sources.
This strategy was compared both with a more conventional 180° decoupled SVPWM scheme, also used to handle OW motors, and with a control system of a classic permanent magnet synchronous motor.
From the simulations carried out, it could be seen that the two drive startegies allow the open-end winding motor to work in a very similar way over a wide speed range.

For the same operation, however, lookup table modulation allows the system's switching frequencies to be reduced compared to the 180° decoupled scheme. Indeed, the latter using two SVPWMs for both inverters will, in addition to increasing the computational complexity of the system, increase the switching losses in the system, thus reducing its efficiency.In contrast, the scheme based on the lookup table is able to make the first inverter operate at a lower switching frequency, since only one switching is required in a period.

Finally, also from the comparisons made in the traction application between the open-end winding motor and a synchronous machine, it was noted that the proposed modulation allows the same performance to be achieved as with a conventional control system.
This means that by implementing the analysed hybrid modulation scheme in electric vehicles, such as cars and trains, the benefits of the dual-inverter configuration can be achieved.
More precisely, the need to use a DC/DC converter would be avoided, since in EVs it is responsible for increased costs and reduced efficiency in power consumption. In addition, without the DC/DC converter, it is possible to also achieve a lower complexity in the

structure of the system. The open-end winding motor also allows for greater reliability in the event of failure and higher control flexibility.

However, there is an increase in the number of components used to form the system, and therefore also in the total costs, which are already high in traction applications due to the presence of the battery pack. The latter is one of the most difficult problems to solve and one that limits the realisation and use of EVs. Indeed, as analysed in the paper [12], a possible solution would be to use a floating capacitor as a second DC source, connected to the compensation inverter. It will not vary the behaviour of the lookup table-based modulation and, at the same time, make it possible to avoid the use of a second battery, reducing the overall costs.

Bibliography

[1] A Vagati, G Pellegrino, and P Guglielmi. Comparison between SPM and IPM motor drives for EV application. *XIX International Conference on Electrical Machines*, 2010.

[2] Electrical Technology, 2000. URL `https://www.electricaltechnology.org/2020/09/difference-synchronous-asynchronous-motor.html`.

[3] Lee Yongjae and Ha Jung-Ik. Power enhancement of dual inverter for open-end permanent magnet synchronous motor. *IEEE Applied Power Electronics*, 2013.

[4] Yi-Fan Jia, Nan Xu, Liang Chu, Yuanjian Zhang, Zhe Xu, Yu-Kuan Li, and Zhi-Hua Yang. Control strategy for an open-end winding induction motor drive system for dual-power electric vehicles. *IEEE Access*, 2020.

[5] Lakshmi Mohan, Kaninika Pant, and P P Rjeevan. A speed range extension scheme for scalar-controlled open-end winding induction motor drives. *IEEE Trans. Industry Applications*, 2022.

[6] Akihito Mizukoshi and Hitoshi Haga. Improvement of output voltage waveform in dual inverter fed open-end winding im at low-speed area. *2018 IEEE Energy Conversion Congress and Exposition*, pages 5422–5427, 2018.

[7] Di Wu, JiFeng Chen, Rui Zhu, and Guowu Hua. Simplified model predictive flux control for dual inverter fed open end winding induction motor. *2019 IEEE International Symposium on PEDG*, pages 1050–1054, 2019.

[8] Xiaogang Lin, Wenxin Huang, and Wen Jiang. Dtc for 3-phase open-end winding pmsm based on zero-sequence current suppression. *22nd International Conference on Electrical MAchines and Systems*, 2019.

[9] Paul Sandulescu, Fabien Meinguet, Xavier Kestelyn, Eric Semail, and Antoine Bruyère. Control strategies for open-end winding drives operating in the flux-weakening region. *IEEE Transactions on Power Electronics*, 29:4829–4842, 2014.

[10] Quntao An, Jin Liu, Zhuang Peng, Li Sun, and Lizhi Sun. Dual-space vector control

of open-end winding permanent magnet synchronous motor drive fed by dual inverter. *IEEE Transactions on Power Electronics*, 31:8329–8342, 2016.

[11] Mu-Shin Kwak and Seung-Ki Sul. Flux weakening control of an open-end winding machine with isolated dual inverters. *IEEE Industry Apllications Conference*, pages 251–255, 2007.

[12] Dan Sun, Zhihao Xheng, Bin Lin, Wenzhi Zhou, and Min Chen. A hybrid pwm-based field weakening strategy for a hybrid-inverter-driven open-end winding pmsm system. *IEEE Transactions on Power Electronics*, pages 857–865, 2017.

[13] Albino Amerise, Luca Rovere, Andrea Formentini, Michele Mengoni, Luca Zarri, and Preicle Zanchetta. Control system for open-end winding surface pm synchronous machines with a floating capacitor bridge. *IEEE Energy Conversion Congress and Exposition*, pages 6585–6591, 2020.

[14] Hyung-Woo Lee, Sung-Jin Jang, and Kyo-Beum Lee. Advanced dpwm method for switching loss reduction in isolated dc type dual inverter with open-end winding ipmsm. *IEEE Access*, 11:2700–2710, 2023.

[15] Yi-Fan Jia, Liang Chu, NaN Xu, Yu-Kuan Li, Di Zhao, and Xin Tang. Power sharing and voltage vector distribution model of a dual inverter open-end winding motor drive system for electric vehicles. *Applied Sciences*, 2018.

[16] Ryan Brody and Brandon M Grainger. Control of boost converter module for open-end winding pm motor based, dual inverter drive. *2020 IEEE Energy Conversion Congress and EXposition*, pages 6345–6352, 2020.

[17] Brian A Welchko. A double-ended inverter system for the combined propulsion and energy management functions in hybrid vehicles with energy storage. *31st Annual Conference of IEEE industrial Electronics Society*, pages 1401–1406, 2005.

[18] Caludio Rossi, Gabriele Grandi, Piero Corbelli, and Domenico Casadei. Generation system for series hybrid powertrain based on the dual two-level inverter. *13th European Conference on Poer Electronics and Applications*, 2009.

[19] Kasoju Bharath Kumar and Kunisetti V Praveen Kumar. An effective predictive torque control technique for open-end winding permanent magnet synchronous motor drives with reduced ripples for evs. *Second International Conference on Power, Control and Computing Technologies*, 2022.

[20] Yongjae Lee and Jung-Ik Ha. Hybrid modulation of dual inverter for open-end winding pmsm. *IEEE Transactions on Power Electronics*, 30:3286–3299, 2015.

[21] Jing Wang and Jianhua Wu. Space vector modulation based on lookup table for a dual-inverter-fed open-end winding pmsm drive. *IEEE Vehicle Power and Propulsion Conference*, 2016.

[22] Duc Tan Vu, Ngac Ky Nguyen, Eric Semail, and Walter Lhomme. Electric vehicles driven by 5-phase open-end winding machines fed by battery and supercapacitors. *IEEE Vehicle Power and Propulsion Conference*, 2019.

[23] Jinseok Hong, Heekwang Lee, and Kwanghee Nam. Charging method for the secondary battery in dual-inverter drive systems for electric vehicles. *IEEE Transactions on Power Electronics*, pages 909–920, 2014.

[24] Ning Xing, Shubo hu, Zhengyu Lin, Zheng Tan, Wenping Cao, and Sahdy Gadoue. New adaptive control strategies for open-end winding pmsg for wind power generator. *The 10th International Conference on Power Electronics, Machines and Drives*, 2021.

[25] Mu-Shin Kwak and Seung-Ki Sul. Control of an open-end winding machine in a grid-connected distributed generation system. *IEEE Industry Applications Conference Forty-First IAS Annual Meeting*, pages 2576–2580, 2006.

List of Figures

List of Tables

Acknowledgements

First of all, I wanted to thank Professor Maria Stefania Carmeli and Professor Marco Mauri for giving me the opportunity to do my graduation thesis on a subject that I have always been passionate about, i.e. electric motors in traction applications, thus linking my study to my passions. I would also like to thank them for having given me a hand during the most difficult moments in the realisation of this study, and for showing me which was the best way to follow to reach the conclusion of my work.
I would also like to thank all the professors who have contributed to improving my knowledge during these five years at the Politecnico. In particular Prof. Castelli Dezza, Prof. Nicola Toscani, Prof. Giovanni Maria Foglia and Prof. Antonino Di Gerlando for making me passionate about all subjects related to electrical machines and their application.
My biggest thanks go to my parents who, through the sacrifices they have made over the years, have given me the opportunity to study at the Politecnico di Milano. I also thank them for having always supported me, together with my brother, during these five years of study and above all, when I found myself in the most difficult times, they were always there to hearten me. I hope that I have at least partially paid you back with the achievement of this milestone.
In addition to them, I can only thank my grandparents, my relatives and all my friends who have always been by my side at all times.